Light Scattering from Ultracold Atomic Gases

James Stewart Douglas

A thesis submitted in partial fulfilment of
the requirements for the degree of
Doctor of Philosophy at the University of Oxford

Balliol College
University of Oxford
Michaelmas Term 2010

Light Scattering from Ultracold Atomic Gases

James Stewart Douglas, Balliol College, University of Oxford

A thesis submitted in partial fulfilment of the requirements for the degree of Doctor of Philosophy at the University of Oxford. Michaelmas Term, 2010

Abstract

Systems of ultracold atoms in optical potentials have taken a place at the forefront of research into many-body atomic systems because of the clean experimental environment they exist in and the tunability of the system parameters. In this thesis we study how light scattered from these ultracold atomic gases reveals information about the state of the atomic gas and also leads to changes in that state.

We begin by investigating the angular dependence of light scattered from atoms in optical lattices at finite temperature. We demonstrate how correlations in the superfluid and Mott insulator states affect the scattering pattern, and we show that temperature affects the number of photons scattered. This effect could be used to measure the temperature of the gas, however, we show that when the lattice band structure is taken into account the efficiency of this temperature measurement is reduced.

We then investigate light scattering from small optical lattices where the Bose-Hubbard Hamiltonian can be solved exactly. For small lattices, scattering a photon from the atomic system significantly perturbs the atomic system. We develop a model of the evolution of the many-body state that results from the consecutive scattering and detection of photons. This model shows that light scattering pushes the system towards eigenstates of the light scattering measurement process, in some cases leading to a superposition of atomic states.

In the second half of this thesis we study light scattering that depends on the internal hyperfine spin state of the atoms, in which case the scattered light can form images of the spatial atomic spin distribution. We demonstrate how scattering spatially correlated light from the atoms can result in spin state images with enhanced spatial resolution. We also show how using spatially correlated light can lead to direct measurement of the spatial correlations of the atomic spin distribution.

We then apply this theory of spin-dependent light scattering to the detection of different spin states of ultracold gases in synthetic magnetic fields. We show that it is possible to distinguish between ground states in the quantum Hall regime using light scattering. Moreover, we show how noise correlation analysis of the spin state images can be used to identify the correlations between atoms and how a variant on phase-contrast imaging can reveal the relationship between the atomic spins.

Acknowledgements

This thesis would not have been possible without the supervision of Keith Burnett. Keith is a true inspiration, and I am yet to leave one of our discussions without a renewed sense of excitement and optimism about my studies. His passion and enthusiasm for physics, and life in general, have been a great motivation and I am thankful for all the advice and wisdom he has given me. I also thank Ian Walmsley for stepping in to be my supervisor when Keith left the university, and for providing many useful insights and being there to help over the years.

When I arrived in Oxford I was welcomed into the Keith Burnett group and I thank Thorsten Köhler, Marzena Szymańska, Mark Lee, Ho Tsang Ng, Tom Hanna, David Hallwood, Andreas Nunnenkamp and Hugo Martay for making that a happy introduction and for making my first few years at Oxford enjoyable ones. My time at the Clarendon Laboratory has benefited from many fruitful discussions and I would like to thank Uwe Dorner, Dieter Jaksch, Lijian Zhang, Amita Deb, Christopher Foot and Simon Thwaite for sharing their ideas and perspectives.

I was very fortunate to be part of Balliol College's graduate community over my time at Oxford. I could not have hoped for a better social environment during my studies than the one provided at Holywell Manor, and I thank all my friends for making the last few years so much fun. Thank you also to all my fellow athletes at the athletics club for providing welcome physical respite from my daily mental grind.

I gratefully acknowledge the financial support provided by the Clarendon Fund for my doctoral studies, without which I would not have been able to come to Oxford, and I also thank Balliol College for assistance.

Thank you to my wonderful family for supporting me over the years, even from the four corners of the earth, and for taking part in the painful proofreading of this thesis. And Erin, for everything, thank you.

Contents

Chapter 1

Introduction

One of the fundamental ways we humans garner information about the world around us is by examining the light that scatters from our surroundings. Needless to say this is also an important way that physicists gain information about the laws of nature, where the light scattered from an object potentially contains information about its large structure, right down to the behaviour of its constituent atoms. In this thesis we investigate how light scattering might be used to examine the properties of new states of matter produced in experiments with ultracold atoms, and also how light scattering might change the properties of the matter in a useful way. In this introduction we discuss our motivation for taking this path and what this has lead us to study in this thesis.

Research involving ultracold atoms has flourished since laser cooling of dilute gases of neutral atoms [1], combined with evaporative cooling, allowed temperatures in the sub micro-Kelvin range to be reached in experiments for the first time, leading to the phenomena of Bose-Einstein condensation [2, 3, 4]. Advances in optical and magnetic cooling have allowed the routine production of Bose-Einstein condensates in laboratories around the world, giving physicists the opportunity to

explore a macroscopic quantum object in a very clean experimental environment [5, 6]. Furthermore, sympathetic cooling of fermions with Bose-Einstein condensates has been used to achieve quantum degeneracy in Fermi gases [7, 8].

The main focus of initial experiments involving ultracold Bose gases was their behaviour in the weakly interacting superfluid regime, where the atoms exhibit long range phase coherence. In this regime the behaviour is well described by the Gross-Pitaevskii equation and Bogoliubov mean-field theory [9]. As ever, the interaction with light played a crucial role in revealing the state of the many-body system. The most prominent method of probing the atomic system has been time of flight absorption imaging, where the atoms are released from their trapping potential, allowed to expand and then hit with resonant light. The amount of light absorbed by the atoms then reveals their density [2]. To create excitations in the system Bragg scattering of photons from one laser beam to another was used, allowing for an excellent test of the Bogoliubov theory [10]. Light scattering was also used to determine the relative phase between two spatially separated Bose-Einstein condensates in an almost non-destructive manner [11]. The coherence properties of a Bose-Einstein condensate were also apparent in an experiment showing directional light scattering as a result of the build up of a matter wave interference pattern [12].

In more recent experiments an emphasis has been placed on increasing interactions betweens atoms allowing for the production of strongly correlated states, which can no longer be described by the mean field theories mentioned above. One way of achieving this is through Feshbach resonance [13], which allows the interaction strength to be altered by applying optical or magnetic fields. One demonstration of the usefulness of this technique has been in mapping for Fermi gases the cross-over from Bardeen-Cooper-Schrieffer superfluidity of atoms paired in momentum space into a Bose-Einstein condensate of molecules [14, 15, 16].

Another method of attaining higher interaction strengths is by loading ultracold atoms into optical potentials formed by standing wave laser fields. For neutral atoms the optical dipole force then creates a sinusoidal potential called an optical lattice that has periodicity of order the wavelength of the laser light [17]. Atoms are then more likely to exist at the periodic potential minima, or lattice sites, increasing the density and hence the effective interaction at these points. Theoretical work has shown that by altering the lattice strength a phase transition between the weakly interacting Bose gas and a Mott insulating state characterised by strong interactions is possible, where the system very closely represents the Bose-Hubbard model used in condensed matter physics [18]. The experimental realisation of this transition [19] confirmed that ultracold gases in optical lattices provide an excellent test bed for condensed matter theory because of the isolation of the atoms from the environment and the ability to adjust parameters such as the interaction strength in experiments [20].

Efforts to demonstrate novel states of matter in ultracold gases have been accompanied by efforts to improve on methods of probing the gas. Bragg scattering was again used, this time as a method to probe the Mott transition [21, 22], while a proposal to apply noise correlation imaging to ultracold gases [23] was successfully used to measure correlations in Bose and Fermi gases [24, 25]. The recent achievement of strong coupling between ultracold gases and optical cavities [26, 27, 28] has led to further interesting regimes of behaviour where the optical lattice and atoms are coupled to one another, and has also allowed for the read-out of atomic properties through cavity emission spectra, which a number of theoretical proposals examine [29, 30, 31, 32, 33]. Schemes have also been proposed to measure the spin state of ultracold atoms in a non-destructive manner by analysing the polarisation of light after it has passed through the atomic gas [34, 35, 36].

The field of ultracold atoms is now taking further steps in simulating condensed

matter physics. By using optical fields synthetic magnetic fields can be induced for neutral atoms [37], opening the field to a potential realisation of the quantum Hall regime. There is a current experimental drive toward the achievement of topological insulators in ultracold gases, a development that would advance efforts toward topological quantum computing [38, 39].

1.1 Thesis overview

In this thesis we study the interaction of light with atoms in optical lattices and also in synthetic magnetic fields. The overriding motivation behind our work has been attempts to couple correlations in ultracold gases with correlations in the light field, with the hope of revealing more information about the atomic state and also with the aim of generating entanglement in the atoms and light.

To begin with, in Chapter 2, we introduce the description of the light-matter interaction that is the central theme of this thesis. This leads naturally to a description of the behaviour of neutral atoms in optical potentials, including a brief review of the Bose-Hubbard model. We also describe developments in the field of quantum imaging that tie into our imaging schemes.

Following this background theory, we present in Chapter 3 a treatment of light scattering from atoms in the superfluid and Mott insulating phases of the Bose-Hubbard model, where we extend recent models of light scattering from finite temperature samples [40, 41] to include the full band structure of the lattice. The simple scheme involved, shining a laser on the sample, demonstrates what can be learnt about the atomic sample by first order light scattering where the input light is uncorrelated and does not significantly perturb the atoms.

In Chapter 4 we solve the Bose-Hubbard model exactly for small lattices sizes, allowing us in the first place to test the validity of the mean-field and perturbative

methods used in Chapter 3. We then proceed to examine how the light scattering affects the atoms in the lattice, moving away from the approximations of the previous chapter, and allowing us to investigate how each scattering event is conditioned on the previous events. We produce a picture of dynamic light scattering from optical lattices, where in some cases the consecutive scattering of light from the lattice leads to the creation of superposition states.

The next step in our investigation, detailed in Chapter 5, examines possible improvements in probing the atomic sample by scattering light that is correlated to begin with, building on results from the field of quantum imaging. For systems of atoms with internal spin degrees of freedom, we show that using correlated input light can lead to resolution enhancements when imaging the spatial spin distribution. Moreover, we develop a method using correlated light to directly reveal information about spatial spin correlations.

Our treatment of spin systems then leads us to consider the quantum spin Hall regime in Chapter 6. We demonstrate the potential to distinguish ground states of the quantum spin Hall model for neutral atoms by using light scattering. We also look at possible applications of noise correlation imaging and a variant of phase contrast imaging to reveal the spin relationship between the atoms in these ground states.

The thesis is then concluded in Chapter 7, followed by an outline of future research possibilities.

Chapter 2

Background theory

In this chapter we will briefly cover some of the background theory required in this thesis. To begin with we will look at the interaction between light and matter that is the basis for all of our work. This naturally leads into a discussion on the creation of periodic optical potentials for neutral atoms or optical lattices as they are otherwise known. We then consider how these optical lattices are used to realise the Bose-Hubbard model. Following this we examine some key results in the field of quantum imaging that motivate our later work on imaging atoms in optical lattices. There are more comprehensive reviews of these subjects available, for example Hammerer *et al.* [42] review the light matter interaction, while Bloch *et al.* [43] review the subject of optical lattices and their use to investigate problems in many-body physics, and *Quantum Imaging* edited by Kolobov provides further details about this developing field [44].

2.1 Interactions between light and alkali atoms

In this section we derive the effective Hamiltonian describing the interaction between detuned light and ultracold atoms in the rotating wave and dipole approximations (see Lewenstein *et al.* for a careful treatment of the approximations involved [45]). This interaction is used to generate optical potentials for cold atoms, and also leads to scattering of light from the atoms, which we will use to probe the atomic state. In the following we assume the light is sufficiently detuned from the excited electronic states of the atomic Hamiltonian so that they can be adiabatically eliminated, and for alkali atoms we find interaction terms that depend only on the hyperfine ground state atomic field operators.

The Hamiltonian of the system can be divided up into two parts, $\hat{H} = \hat{H}_0 + \hat{H}_{af}$, where $\hat{H}_0 = \hat{H}_a + \hat{H}_f$ is the sum of the Hamiltonians describing the behaviour of the atomic system $\hat{H}_a$ and the electromagnetic field $\hat{H}_f$ in absence of one another, and $\hat{H}_{af}$ describes the interaction of the atoms with the field. The Hamiltonian of the atom system is

$$\hat{H}_a = \sum_\alpha \int d\mathbf{r} \hat{\Psi}^\dagger_\alpha(\mathbf{r}) \left[-\frac{\hbar^2 \nabla^2}{2m} + V_\alpha(\mathbf{r}) \right] \hat{\Psi}_\alpha(\mathbf{r}) + \hat{H}_{aa}, \tag{2.1}$$

where $\hat{H}_{aa}$ describes interactions between the atoms and $V_\alpha(\mathbf{r})$ describes external trapping of the atoms. The field operators $\hat{\Psi}_\alpha(\mathbf{r})$ and $\hat{\Psi}^\dagger_\alpha(\mathbf{r})$ destroy and create atoms at $\mathbf{r}$ with internal atomic state α [46]. For a boson field the operators obey the usual commutator relations $[\hat{\Psi}_\alpha(\mathbf{r}), \hat{\Psi}^\dagger_{\alpha'}(\mathbf{r}')] = \delta_{\alpha,\alpha'}\delta(\mathbf{r} - \mathbf{r}')$ and $[\hat{\Psi}_\alpha(\mathbf{r}), \hat{\Psi}_{\alpha'}(\mathbf{r}')] = [\hat{\Psi}^\dagger_\alpha(\mathbf{r}), \hat{\Psi}^\dagger_{\alpha'}(\mathbf{r}')] = 0$.

In the dipole approximation the interaction Hamiltonian between the light and matter fields is

$$\hat{H}_{af} = -\sum_{\alpha,\alpha'} \int d^3\mathbf{r} \hat{\Psi}^\dagger_\alpha(\mathbf{r}) \hat{\Psi}_{\alpha'}(\mathbf{r}) \mathbf{d}_{\alpha,\alpha'} \cdot \hat{\mathbf{E}}(\mathbf{r}), \tag{2.2}$$

where $\hat{\mathbf{E}}(\mathbf{r})$ is the electric field operator. In this approximation the strength of the coupling between the internal states of the atom depends only on $\mathbf{d}_{\alpha,\alpha'} = \langle\alpha|\mathbf{d}|\alpha'\rangle$, the matrix elements of the atom's electric dipole moment.

For the purpose of making the rotating wave approximation we can divide the electric field operator into two parts

$$\hat{\mathbf{E}}(\mathbf{r}) = \hat{\mathbf{E}}^{+}(\mathbf{r}) + \hat{\mathbf{E}}^{-}(\mathbf{r}), \tag{2.3}$$

where $\hat{\mathbf{E}}^{+}(\mathbf{r})$ is the positive frequency part of the field, which can in turn be expanded over plane wave modes with wave vector $\mathbf{k}$, polarisation vector $\boldsymbol{\epsilon}_{\mathbf{k},\nu}$ and annihilation operators $\hat{a}_{\mathbf{k},\nu}$, that is

$$\hat{\mathbf{E}}^{+}(\mathbf{r}) = i\sum_{\nu}\int d\mathbf{k}\sqrt{\frac{\hbar\omega_{\mathbf{k}}}{2\epsilon_0(2\pi)^3}}\hat{a}_{\mathbf{k},\nu}e^{i\mathbf{k}\cdot\mathbf{r}}\boldsymbol{\epsilon}_{\mathbf{k},\nu}. \tag{2.4}$$

The negative frequency part is then given by $\hat{\mathbf{E}}^{-}(\mathbf{r}) = [\hat{\mathbf{E}}^{+}(\mathbf{r})]^{\dagger}$. With this expansion, the Hamiltonian for the free electromagnetic field is $\hat{H}_f = \sum_{\nu}\int d\mathbf{k}\hbar\omega_{\mathbf{k}}\hat{a}^{\dagger}_{\mathbf{k},\nu}\hat{a}_{\mathbf{k},\nu}$.

We also divide the atomic internal states into a manifold of ground states, denoted by α's, and a manifold of excited states, denoted by β's, that will be coupled together by the interaction with light. We then make the rotating wave approximation by only retaining the terms in the Hamiltonian that conserve the number of excitations. These processes – the absorption of a photon by a ground state atom leading to an excited atom, and the emission of a photon by an excited state atom leading to a ground state atom – dominate processes such as photon emission by a ground state atom leading to an excited state atom, which do not conserve energy. The Hamiltonian then becomes

$$\hat{H}_{af} = -\sum_{\alpha,\beta}\int d^3\mathbf{r}\hat{\Psi}^{\dagger}_{\alpha}(\mathbf{r})\hat{\Psi}_{\beta}(\mathbf{r})\mathbf{d}_{\alpha,\beta}\cdot\hat{\mathbf{E}}^{-}(\mathbf{r}) - \sum_{\alpha,\beta}\int d^3\mathbf{r}\hat{\Psi}^{\dagger}_{\beta}(\mathbf{r})\hat{\Psi}_{\alpha}(\mathbf{r})\mathbf{d}^{*}_{\alpha,\beta}\cdot\hat{\mathbf{E}}^{+}(\mathbf{r}). \tag{2.5}$$

We assume that the frequency distribution of the electromagnetic field is centred around a dominant frequency ω_L. In the Heisenberg picture we can then identify the slowly varying operators $\hat{\Psi}'_\beta(\mathbf{r}) = \hat{\Psi}_\beta(\mathbf{r})e^{i\omega_L t}$, $\tilde{\mathbf{E}}^+(\mathbf{r}) = \hat{\mathbf{E}}^+(\mathbf{r})e^{i\omega_L t}$, $\tilde{\mathbf{E}}^-(\mathbf{r}) = \hat{\mathbf{E}}^-(\mathbf{r})e^{-i\omega_L t}$. The Heisenberg equations of motion for the slowly varying excited states then become

$$\frac{\partial \hat{\Psi}'_\beta(\mathbf{r})}{\partial t} = i\left(\frac{\hbar}{2m}\nabla^2 - \frac{V_\beta(\mathbf{r})}{\hbar} - \Delta_\beta\right)\hat{\Psi}'_\beta(\mathbf{r}) + \frac{i}{\hbar}\sum_\alpha \hat{\Psi}'_\alpha(\mathbf{r})\mathbf{d}^*_{\alpha,\beta}\cdot\tilde{\mathbf{E}}^+(\mathbf{r}). \qquad (2.6)$$

where $\Delta_\beta = \omega_\beta - \omega_L$ is the detuning of the light's dominant frequency from the excited state's frequency.

For detunings Δ_β that are large compared to the natural line widths of the transitions involved and the Rabi frequencies associated with the electric field, the contributions from the kinetic energy and trap terms in Equation 2.6 will become insignificant and we ignore them. Effectively the atoms do not then spend any time in the excited state and therefore the excited state kinetic energy and potential terms do not play a role. Within this approximation we can formally integrate Equation (2.6) giving

$$\hat{\Psi}'_\beta(\mathbf{r},t) = \frac{i}{\hbar}\sum_\alpha \int_0^t ds e^{-i\Delta_\beta(t-s)}\hat{\Psi}_\alpha(\mathbf{r},s)\mathbf{d}^*_{\alpha,\beta}\cdot\tilde{\mathbf{E}}^+(\mathbf{r},s) + \hat{\Psi}'_\beta(\mathbf{r},0)e^{-i\Delta_\beta t}. \qquad (2.7)$$

We now assume that the slowly varying operators vary on a time scale that is long compared with $2\pi/\Delta_\beta$. For this to be true, the detunings must be larger than the frequency width of the ground state manifold and the frequency width of the slowly varying electric field. Energy conservation dictates that non-resonant scattering of light by the atoms results in a frequency shift for the light of order of the sum of the recoil frequency and the frequency associated with any change of internal atomic state. For the transitions we consider in this thesis, the recoil frequency is typically at least an order of magnitude less than the natural line

widths. It is thus sufficient to assume that the detuning is greater than the natural line widths, as we already did above, and the width of the ground state manifold. In this case the slowly varying operators can be taken outside of the integral, and the fast rotating initial term will make a negligible contribution to the evolution. With this approximation we get the following solution for the excited state

$$\hat{\Psi}'_{\beta}(\mathbf{r},t) = \sum_{\alpha} \hat{\Psi}_{\alpha}(\mathbf{r},t)\frac{\mathbf{d}^{*}_{\alpha,\beta}\cdot\tilde{\mathbf{E}}^{+}(\mathbf{r},t)}{\hbar\Delta_{\beta}}. \tag{2.8}$$

Using this solution for the excited state is the same as adopting the effective interaction Hamiltonian

$$\hat{H}^{ef}_{af} = -\sum_{\alpha,\alpha',\beta}\int d\mathbf{r}\hat{\Psi}^{\dagger}_{\alpha}(\mathbf{r})\frac{(\tilde{\mathbf{E}}^{-}(\mathbf{r})\cdot\mathbf{d}_{\alpha,\beta})(\mathbf{d}^{*}_{\alpha',\beta}\cdot\tilde{\mathbf{E}}^{+}(\mathbf{r}))}{\hbar\Delta_{\beta}}\hat{\Psi}_{\alpha'}(\mathbf{r}), \tag{2.9}$$

removing any dependence on the excited state atomic field operators from the model.

2.1.1 Atomic polarisability

We now take a closer look at the electric dipole operator $\mathbf{d} = -e\sum_j(\mathbf{r}_j - \mathbf{r})$, which results from the positions $\mathbf{r}_j - \mathbf{r}$ of the electrons around the nucleus at $\mathbf{r}$. Taking the z-axis as the axis of quantisation for the internal atomic states, we can decompose the dipole operator into its spherical vector components

$$\mathbf{d} = \sum_{\sigma=-1}^{1} d_{\sigma}\boldsymbol{\epsilon}^{*}_{\sigma}, \tag{2.10}$$

where $\boldsymbol{\epsilon}_0 = \hat{\mathbf{z}}$ and $\boldsymbol{\epsilon}_{\pm1} = \mp(\hat{\mathbf{x}} \pm i\hat{\mathbf{y}})/\sqrt{2}$.

Here we are concerned with transitions between ground hyperfine states Fm and excited hyperfine states $F'm'$, where $\mathbf{F} = \mathbf{J} + \mathbf{I}$ is the total atomic angular momentum resulting from the addition of the total electronic angular momentum

J and nuclear spin **I**. The dipole matrix element between these states is denoted by

$$\mathbf{d}^{+}_{J'F'm',JFm} = \sum_{\sigma} \langle J'IF'm'|d_\sigma|JIFm\rangle \boldsymbol{\epsilon}^{*}_{\sigma} \tag{2.11}$$

These matrix elements can be calculated explicitly with the help of Clebsch-Gordan coefficients as detailed in Appendix 2.A. The effective interaction Hamiltonian can then be expressed as

$$\hat{H}^{ef}_{af} = -\int d\mathbf{r} \hat{\Psi}^{\dagger}_{J_2,F_2,m_2}(\mathbf{r})(\tilde{\mathbf{E}}^{-}(\mathbf{r})\vec{\alpha}_{J_1F_1m_1,J_2F_2m_2}\tilde{\mathbf{E}}^{+}(\mathbf{r}))\hat{\Psi}_{J_1,F_1,m_1}(\mathbf{r}), \tag{2.12}$$

in terms of the polarisability tensor [42]

$$\vec{\alpha}_{J_1F_1m_1,J_2F_2m_2} = \sum_{J',F',m'} \frac{\mathbf{d}^{-}_{J_2F_2m_2,J'F'm'} \otimes \mathbf{d}^{+}_{J'F'm',J_1F_1m_1}}{\hbar\Delta_{J',F'}}, \tag{2.13}$$

where we use the notation $\mathbf{a}(\mathbf{b}\otimes\mathbf{c})\mathbf{d} = (\mathbf{a}\cdot\mathbf{b})(\mathbf{c}\cdot\mathbf{d})$.

Many ultracold atom experiments are done with alkali atoms and we now restrict our attention to alkali atoms making transitions from the $J = 1/2$ ground state to the $J' = 1/2, 3/2$ excited states. If we are detuned enough from the excited state levels then we can approximate $\Delta_{J',F'} \approx \Delta_{J'}$ in Equation (2.13) and we can simplify the polarisability tensor as detailed in Appendix 2.B [47, 48, 42]. The effective interaction Hamiltonian then breaks into two parts. The first does not depend on the internal state of the atom and is given by

$$H^{(0)}_{af} = -a_0(\Delta_{3/2}) \sum_{m} \int d\mathbf{r} \hat{\Psi}^{\dagger}_{m}(\mathbf{r}) \tilde{\mathbf{E}}^{-}(\mathbf{r}) \cdot \tilde{\mathbf{E}}^{+}(\mathbf{r}) \hat{\Psi}_{m}(\mathbf{r}). \tag{2.14}$$

For incoming linearly polarised light, this interaction results in light scattering in a dipole pattern, where the strength of scattering depends on $\sin^2(\theta)$, θ being the angle between the direction of the scattered light and the input light's polarisation

vector [12]. The second part is a spin dependent interaction

$$H_{af}^{(1)} = -a_1(\Delta_{3/2}) \sum_{m_1,m_2} \int d\mathbf{r} \hat{\Psi}_{m_2}^{\dagger}(\mathbf{r}) \langle F m_2 | (\hat{\mathbf{F}}/\hbar) \cdot (\tilde{\mathbf{E}}^{-}(\mathbf{r}) \times \tilde{\mathbf{E}}^{+}(\mathbf{r})) | F m_1 \rangle \hat{\Psi}_{m_1}^{\dagger}(\mathbf{r}), \tag{2.15}$$

that is responsible for the Faraday effect. This interaction leads to scattering in directions prohibited in the dipole pattern and changes in polarisation of the scattered photons [49]. The atom-field coupling coefficients $a_0(\Delta_{3/2})$ and $a_1(\Delta_{3/2})$ are defined by Equations (2.41) and (2.44) in Appendix 2.B, see also Hammerer *et al.* for further details [42].

Both these interactions are used in creating optical lattices in experiments today. As discussed in the next section, the state independent interaction leads to a simple realisation of an optical lattice using reflected laser light. The spin-dependent interaction allows one to produce more complicated potentials that depend on the hyperfine state of the atoms and provide a rich testing ground for spin-dependent models [50, 51, 52, 53, 54]. Both terms will play a part in the light scattering interactions we discuss in this thesis.

2.2 Optical lattices

We will now demonstrate how the light matter interaction described above can be used to create an optical potential for the atoms. Suppose the electromagnetic field consists of a coherent state with mode function $u(\mathbf{r})$, with linear polarisation $\boldsymbol{\varepsilon}$ and frequency ω_L. We can then approximate the electric field operator as a classical state $\tilde{\mathbf{E}}^{+}(\mathbf{r}) = \mathcal{E}_L u(\mathbf{r}) \boldsymbol{\varepsilon}$ and the spin-dependent interaction plays no part. Equation

(2.14) then leads to the effective Hamiltonian for the atoms

$$\hat{H}^{ef} = \sum_{\alpha} \int d\mathbf{r} \hat{\Psi}^{\dagger}_{\alpha}(\mathbf{r}) \left[-\frac{\hbar^2 \nabla^2}{2m} + V_{\alpha}(\mathbf{r}) + V_L(\mathbf{r}) \right] \hat{\Psi}_{\alpha}(\mathbf{r}), \tag{2.16}$$

where we have for the moment neglected atom-atom interactions. In addition to the external potential $V_{\alpha}(\mathbf{r})$, the atoms now experience a potential $V_L(\mathbf{r}) = V_0|u(\mathbf{r})|^2$ resulting from the light matter interaction, where the magnitude of this potential is $V_0 = -a_0(\Delta_{3/2})|\mathcal{E}_L|^2$. The sign of the potential depends on the sign of $a_0(\Delta_{3/2})$, which in turn depends on the detuning. When one of the $S_{1/2} \rightarrow P_{1/2}, P_{3/2}$ transitions is dominant over the other, the sign of $a_0(\Delta_{3/2})$ is then just the sign of the detuning to the dominant level (see discussion at the end of Appendix 2.B). For red detuned light this sign is positive, leading to atoms having lower potential energy where the radiation field intensity is higher, and atoms may be trapped at the intensity maxima of the field, while the reverse is true for blue detuned light.

If the light field is in a standing wave mode $u(\mathbf{r}) = \sin(\mathbf{k}_L \cdot \mathbf{r})$, created for example by retroreflecting a laser beam, then the atoms will experience a sinusoidal potential $V_0 \sin^2(\mathbf{k}_L \cdot \mathbf{r})$, with spatial period half that of the laser wavelength. This is referred to as an optical lattice, in this case a one-dimensional lattice. The potential minima of the lattice are referred to as lattice sites and we denote the inter-site distance by a. Higher dimensional lattices can be created by adding standing waves in the other dimensions, where coupling between the different standing waves is avoided by detuning them from one another or by using orthogonal polarisations. Different laser orientations can result in more complicated lattice geometries [55]. In this thesis we restrict our attention to isotropic lattices with the same site spacing a in each dimension. We use the notation N to refer to the total number of atoms contained in the lattice, and M to refer to the number of lattice sites. The relevant energy scale of the optical potential is the recoil energy $E_R = \frac{\hbar^2 k_L^2}{2m}$, which is the

kinetic energy an atom at rest obtains as a result of absorbing a photon with wave vector k_L. With this in mind we use E_R as our natural unit of energy.

Above we have neglected the effect of spontaneous emission events where photons are scattered incoherently out of the lattice laser beams. The rate at which these events occur can be estimated by calculating an effective spontaneous emission rate for each excited state level, which is the product of the probability of being in the excited state multiplied by the decay rate of that level [56]. For red detuned lattices the atoms reside in the antinodes of the field and are therefore more likely to be excited by the field, leading to higher spontaneous emission rates than for blue detuned lattices. However, in either case it is usually possible to arrange experimental parameters so that spontaneous emission occurs on a time scale that is much greater than the typical experimental time scale and is therefore negligible [56]. In this way, we can regard the lattice potential as being conservative.

2.2.1 Band structure

We have seen that it is possible to create a sinusoidal potential for atoms using the interaction with detuned light, we now examine the behaviour of atoms in these optical lattices. To begin with we take the simple case of atoms that do not interact with one another and are not subject to an external potential, in which case we require the single particle eigenstates of the Hamiltonian $\hat{H} = \frac{p^2}{2m} + V_L(\mathbf{r})$. Bloch's theorem [57, 58] states that the single particle eigenstates for a periodic potential are of the form

$$\phi_{\mathbf{n},\mathbf{q}}(\mathbf{r}) = u_{\mathbf{n},\mathbf{q}}(\mathbf{r})e^{i\mathbf{q}\cdot\mathbf{r}} \tag{2.17}$$

where $u_{\mathbf{n},\mathbf{q}}(\mathbf{r})$ is a function with the same periodicity as the potential. These eigenstates are called Bloch functions and have two quantum numbers identifying them: the quasi-momentum or crystal momentum $\mathbf{q}$ and the band index $\mathbf{n}$.

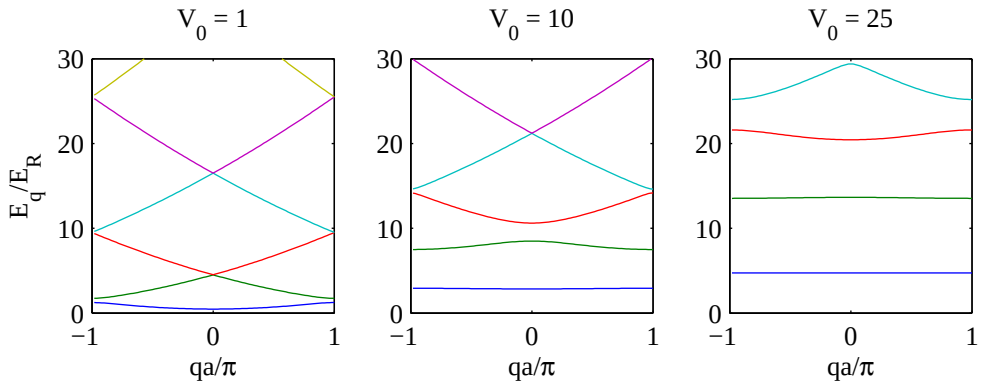

Figure 2.1: Band structure for 1d optical lattices of the form $V_0 \sin^2(k_L x)$ with $V_0 = E_R, 10E_R$ and $25E_R$ respectively.

The quasi-momentum is so named because it is the quantum number associated with the discrete translational symmetry of the lattice, in the same way that momentum is the quantum number associated with the translational symmetry of free space. Furthermore, the quasi-momentum plays a similar role to momentum in conservation laws governing momentum transfer in the lattice [57]. The quasi-momentum differs from momentum in that adding a reciprocal lattice vector $\mathbf{Q}$ results in an equivalent description $\mathbf{q} = \mathbf{q}' + \mathbf{Q}$ and the quasi-momentum can be confined to lie within the Brillouin zone (BZ) of the lattice, which in one dimension is given by $-\pi/a < q < \pi/a$. For each quasi-momentum there are an infinite number of possible eigenstates enumerated by the band index. Bloch functions with the same band index have energies that are a continuous function of quasi-momentum, forming bands of allowable energies called the band structure of the lattice.

The Bloch functions and their associated energies $E_{\mathbf{n},\mathbf{q}}$ can be found numerically [59, 60] and we show the band structure for some example one-dimensional lattices in Figure 2.1. In the figure we see that for low strength lattices, $V_0 = E_R$, the band structure closely resembles the dispersion relation of a free atom. As the lattice strength increases we see gaps forming between the energy bands, and the band width of the lower bands decreases. As V_0 gets larger the band structure approaches the energy levels of a harmonic potential.

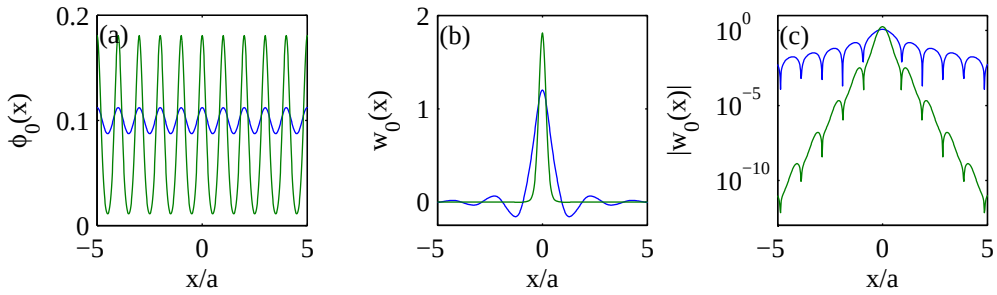

Figure 2.2: Bloch and Wannier functions for 1d optical lattices of the form $V_0 \sin^2(k_L x)$ with (blue) $V_0 = E_R$ and (green) $V_0 = 15E_R$. (a) Bloch functions $\phi_0(x)$, (b) lowest band Wannier functions $w_0(x)$ and (c) modulus of lowest band Wannier functions $|w_0(x)|$.

2.2.2 Wannier functions

The Bloch functions are a basis of states of the atomic system that are delocalised in the lattice, as shown in Figure 2.2(a). It is often desirable to have a basis of states that are localised at the individual lattice sites $\mathbf{r}_j$. Typically the Wannier states [57, 58] are adopted, which are given by the Fourier transform of the Bloch functions

$$w_{\mathbf{n}}(\mathbf{r} - \mathbf{r}_j) = \frac{1}{\sqrt{M}} \sum_{\mathbf{q} \in BZ} e^{-i\mathbf{q}\cdot\mathbf{r}_j} \phi_{\mathbf{n},\mathbf{q}}(\mathbf{r}). \tag{2.18}$$

Equation (2.18) does not uniquely identify the Wannier functions, as the arbitrary choice of phase of the Bloch functions can alter the spread of the Wannier function. However, Kohn [61] has shown that there exists a unique Wannier function that decays exponentially and is maximally localised. With the correct choice of Bloch function phase these maximally localised functions can be constructed using Equation (2.18) [59, 60]. Furthermore, the resulting functions are purely real. In Figure 2.2(b) we plot the lowest band Wannier functions for two different lattice strengths, while in Figure 2.2(c) we plot their modulus on a log scale to demonstrate their exponential localisation, which increases with lattice strength.

2.2.3 Bose-Hubbard Model

We now look at systems of interacting atoms in optical lattices. In doing so we only consider ultracold atoms where, to a good approximation, the atoms only interact with one another via two-body s-wave scattering, which is isotropic and fully determined by the s-wave scattering length a_s. In this case the actual atomic interaction potential can be replaced by a delta function pseudo-potential that gives the same asymptotic scattering [62]. The second quantised Hamiltonian for the atoms in the optical potential is then

$$\hat{H} = \sum_{\alpha} \int d^3\mathbf{r} \hat{\Psi}^{\dagger}_{\alpha}(\mathbf{r}) \left[-\frac{\hbar^2 \nabla^2}{2m} + V_L(\mathbf{r}) + \frac{2\pi\hbar^2 a_s}{2m} \hat{\Psi}^{\dagger}_{\alpha}(\mathbf{r}) \hat{\Psi}_{\alpha}(\mathbf{r}) \right] \hat{\Psi}_{\alpha}(\mathbf{r}). \tag{2.19}$$

The field operators can now either be expanded in terms of the Bloch basis or the Wannier basis. We examine the former expansion in Section 3.2 where we describe the Bogoliubov theory of the weakly interacting Bose gas in an optical lattice. Here we take the latter expansion $\hat{\Psi}_{\alpha}(\mathbf{r}) = \sum_{j,\mathbf{n}} \hat{b}_{j,\mathbf{n}} w_{\mathbf{n}}(\mathbf{r} - \mathbf{r}_j)$. We also assume that the temperature and density of the atoms in the lattice are low enough that the atoms only reside in the lowest band $\mathbf{n} = \mathbf{0}$ and drop the band index. This single-band approximation is good when both the thermal energy and the atomic interaction energy are much less than the energy gap between the two lowest bands and can be readily achieved by loading ultracold atoms into a lattice [18]. The Hamiltonian can then be expressed as

$$\hat{H} = \sum_{j,l} J_{j,l} \hat{b}^{\dagger}_j \hat{b}_l + \frac{1}{2} \sum_{j,l,r,s} U_{j,k,l,s} \hat{b}^{\dagger}_j \hat{b}^{\dagger}_k \hat{b}_l \hat{b}_s, \tag{2.20}$$

where

$$J_{j,l} = \int d^3\mathbf{r} w(\mathbf{r} - \mathbf{r}_j) \left[-\frac{\hbar^2 \nabla^2}{2m} + V_L(\mathbf{r}) \right] w(\mathbf{r} - \mathbf{r}_l) \tag{2.21}$$

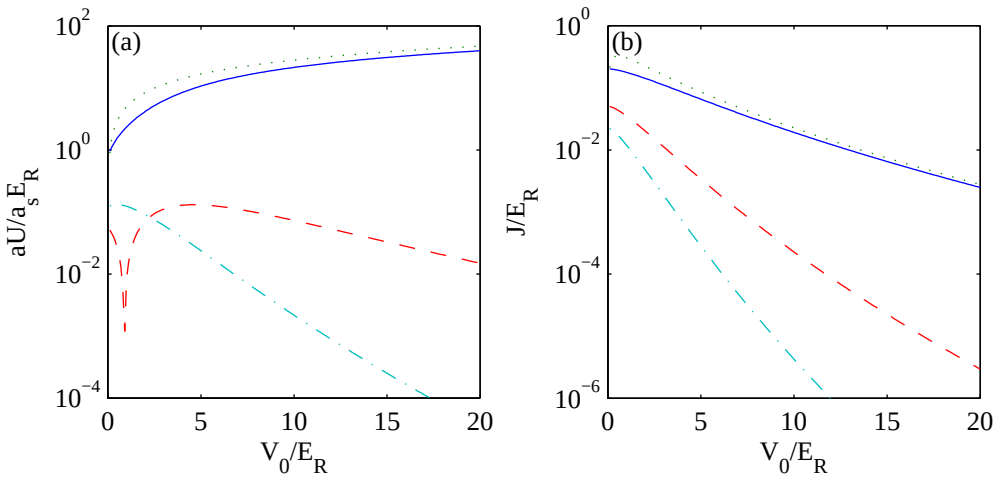

Figure 2.3: (a) Interaction matrix elements (solid) $U_{0,0,0,0}$, (dotted) harmonic approximation from Equation (2.24), (dashed) $|U_{0,0,0,1}|$ and (dot-dashed) $U_{0,0,1,1}$. (b) Tunnelling matrix elements (solid) $-J_{0,1}$, (dotted) harmonic approximation from Equation (2.25), (dashed) $J_{0,2}$ and (dot-dashed) $-J_{0,3}$. Calculations are all for an isotropic three dimensional lattice.

is the tunnelling matrix element and

$$U_{j,k,l,s} = \frac{4\pi\hbar^2 a_s}{2m} \int d^3\mathbf{r} w(\mathbf{r}-\mathbf{r}_j) w(\mathbf{r}-\mathbf{r}_k) w(\mathbf{r}-\mathbf{r}_l) w(\mathbf{r}-\mathbf{r}_s) \tag{2.22}$$

is the atomic interaction matrix element.

The description is further simplified in what is known as the tight-binding approximation, where only nearest neighbour tunnelling terms $J = -J_{j,l}$, l being a neighbouring site to j, are retained. In Figure 2.3(b) we compare the nearest neighbour tunnelling matrix element with the tunnelling elements for sites separated by $2a$ and $3a$. For lattice strengths $V_0 > 4E_R$, the nearest neighbour term is greater than all other tunnelling elements by at least an order of magnitude. Similarly, the interaction terms are dominated by the onsite interaction term $U = U_{j,j,j,j}$, which we plot in Figure 2.3(a) against the next largest interaction matrix elements. We see that the onsite interaction term is an order of magnitude larger than the others even for $V_0 = 1E_R$. Retaining only these dominant terms we have

the Bose-Hubbard Hamiltonian [18]

$$\hat{H} = -J \sum_{\langle j,l \rangle} \hat{b}_j^\dagger \hat{b}_l + \frac{1}{2} U \sum_j \hat{n}_j (\hat{n}_j - 1), \tag{2.23}$$

where $\langle j, l \rangle$ indicates a sum over nearest neighbours.

The Bose-Hubbard model was originally used as a crude model for condensed matter systems to describe the breakdown of superfluidity as interactions increased [63]. Here for optical lattices this model provides a very good description of the system, and experiments in this regime therefore provide an excellent testing ground for the properties of this model. What makes optical lattices even more successful in this regard is that they provide easily adjustable crystalline-like structures, indeed both U and J can be adjusted by altering the strength of the optical lattice. In the tight binding regime the ground band Wannier states are closely approximated by the ground state of a harmonic oscillator. In this approximation the interaction strength (for a three dimensional isotropic lattice) depends on the lattice strength V_0 as follows

$$U \approx \frac{\sqrt{8\pi} a_s}{a} \left(\frac{V_0}{E_R} \right)^{3/4} E_R. \tag{2.24}$$

Furthermore, the tunnelling matrix element can be estimated by calculating the width of the ground band [64], yielding

$$J \approx \frac{4}{\sqrt{\pi}} \left(\frac{V_0}{E_R} \right)^{3/4} \exp \left[-2 \left(\frac{V_0}{E_R} \right)^{1/2} \right] E_R. \tag{2.25}$$

The ratio of interaction to tunnelling then changes with V_0 according to

$$\frac{U}{J} \approx \frac{\pi a_s}{2a} \exp \left[2 \left(\frac{V_0}{E_R} \right)^{1/2} \right], \tag{2.26}$$

allowing the system to be tuned from a regime where tunnelling dominates to

a regime where atomic interactions dominate. The ratio U/J can also be altered without changing the optical lattice strength by using Feshbach resonance to change the interaction strength alone [13]. This flexibility enables experiments with optical lattices to probe the full range of behaviour predicted by the Bose-Hubbard model, as we discuss next.

2.2.4 Transition from superfluid to Mott insulator

As the ratio of U/J is changed in the Bose-Hubbard model, a transition between a superfluid phase and a phase known as the Mott insulator is expected [63]. To gain a little insight into the nature of these phases we examine the limit where $U = 0$ and then the limit where $J = 0$.

The superfluid regime occurs when $J \gg U$. In the limit $U = 0$ we can find the ground state of the Bose-Hubbard Hamiltonian exactly to be

$$|\Psi_{SF}\rangle = \frac{1}{\sqrt{N!}} \left(\hat{b}_{\mathbf{0}}^{\dagger}\right)^{N} |0\rangle, \tag{2.27}$$

where $\hat{b}_{\mathbf{0}}^{\dagger} = \sum_j b_j^{\dagger}$ is the creation operator of the lowest energy Bloch state with quasi-momentum $\mathbf{q} = \mathbf{0}$. This macroscopic occupation of the ground state is referred to as Bose-Einstein condensation. The Bloch state is completely delocalised across the lattice, and hence each atom is in a superposition across the lattice sites. By expanding the Bloch state creation operator in terms of the Wannier site operators we find the average number density per site is $\langle n \rangle = N/M$, and the expectation of the single-particle density matrix $\langle b_j^{\dagger} b_l \rangle = \langle n \rangle$, for any j and l, demonstrating the long range order expected of a Bose-Einstein condensate. The number fluctuations at each site are $\langle n^2 \rangle - \langle n \rangle^2 = \langle n \rangle (M-1)/M$.

For $U \gg J$ and for commensurate filling — N equal to an integer multiple of M — the lattice is in the Mott insulator regime. For $J = 0$ each lattice site has a

definite number of atoms residing there, and the ground state is given by

$$|\Psi_{MI}\rangle = \frac{1}{(N/M)!^{M/2}} \prod_j \left(\hat{b}_j^\dagger\right)^{(N/M)} |0\rangle. \tag{2.28}$$

In this state the number fluctuations per site are zero, and hence there can be no phase relation between the individual sites. Moreover, for $J = 0$ there is an excitation gap of U between the ground and first excited states, in contrast to the superfluid phase which is gapless in the thermodynamic limit, $N, M \to \infty$.

We will further examine the nature of the superfluid and the Mott insulator regimes by using mean-field and perturbation theory to describe what happens as we move away from the $U = 0$ or $J = 0$ limits in Chapter 3. Following this in Chapter 4 we will study the exact solution of the Bose-Hubbard model for small lattices across the transition from the superfluid to the Mott regime.

2.3 Quantum imaging

In Chapters 5 and 6 of this thesis we discuss using entangled light to improve measurements of the atomic state. This work is motivated by developments in the field of quantum imaging [44, 65]. Our particular interest is in the aim of quantum imaging to create images that have higher resolution than allowed by the Rayleigh diffraction limit. Atoms in optical lattices are separated by distances of order of the wavelength of light, meaning that any system for imaging the atoms *in situ* that is subject to the Rayleigh bound will have difficulty resolving the lattice sites. In the following we detail some key results that feed into our work.

We begin with the seminal proposal by Boto *et al.* to improve the resolution of lithography using entangled light [66]. The scheme that Boto *et al.* consider is the simple interferometer depicted in Figure 2.4. Light enters a beam splitter in input modes a and b, then the two resulting light modes c and d are made to

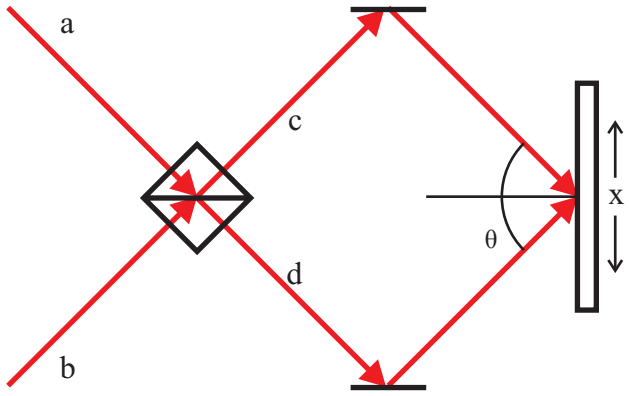

Figure 2.4: Interferometer used in Boto *et al.* Modes a and b are input into a beam-splitter leading to modes c and d which interfere at angle θ on a lithographic plate.

interfere on a lithographic plate. In the classical regime, input of a coherent beam with wavelength λ into mode a would result in an intensity pattern on the surface that varies as $1 + \cos(4\pi \sin(\theta)x/\lambda)$. This pattern has a peak to peak distance of $\lambda/(2\sin(\theta))$ which is minimised for grazing incidence $\theta \to \pi/2$.

Boto *et al.* proposed to improve on the resolution of this pattern using quantum states of light and lithographic media that respond to multiphoton absorption. For N photons, absorption then occurs in proportion to the N-photon correlation function $\langle E^-(x)^N E^+(x)^N \rangle$, where for the simple two mode case at grazing incidence we have $E^+(x) \propto \hat{c}e^{-i2\pi x/\lambda} + \hat{d}e^{i2\pi x/\lambda}$. Now in the two-photon case, an input of the number product state $|1\rangle_a|1\rangle_b$ into the beam splitter results in the path entangled state $(|2\rangle_c|0\rangle_d + |0\rangle_c|2\rangle_d)/\sqrt{2}$. The two-photon absorption then has a spatial dependence $1 + \cos(8\pi \sin(\theta)x/\lambda)$, with peak to peak distance half of what we had in the classical case. This can then be generalised to N photons using the state $(|N\rangle_c|0\rangle_d + |0\rangle_c|N\rangle_d)/\sqrt{2}$, referred to as a NOON state, although this state cannot be generated by simple input into the beam splitter as in the two photon case. In this case the spatial dependence is $1+\cos(4N\pi \sin(\theta)x/\lambda)$, giving a pattern with spatial frequency depending on $1/N$.

Following Boto *et al.*'s proposal it was noted that patterns with the same in-

crease in frequency could be generated using classical light and N-photon absorption but with limited visibility [67, 68, 69]. Later research has extended implementations using classical light further but rely on other specific properties of the absorbing media [70, 71, 72]. N-photon absorption was shown to be limited for the path entangled NOON states considered above [73], although in some cases this may be optimised [74]. A recent proposal by Tsang [75] avoids the problems associated with N-photon absorption, by instead using post-analysis of the intensity distribution. This scheme cannot be directly applied to lithography but will be useful in our case where we are simply interested in the image formed.

The root of Tsang's proposal is illustrated by the following example based on the setup considered by Boto *et al.* The only difference is that now we take spatial resolved intensity measurements at the image plane instead of using an N-photon absorbing material. A two photon state will then lead to a two photon intensity distribution $\langle E^-(x_1)E^-(x_2)E^+(x_2)E^+(x_1)\rangle$, where this distribution gives the probability of recording a photon at x_1 and another photon at x_2. For the two-photon NOON state this distribution varies in space as $1+\cos(4\pi\sin(\theta)(x_1+x_2)/\lambda)$. Tsang noticed that if we now measure the centroid of the photon positions $X = (x_1+x_2)/2$, then this has a probability distribution with peak to peak difference of half that of the classical case, just as in the Boto *et al.* proposal. This also can be generalised to N-photon states, and measuring the centroid $X = \sum_n x_n/N$ gives a probability distribution with peak to peak distance λ/N.

This technique requires only spatially resolved intensity measurements and post-processing of the data, a significant improvement over requiring N-photon absorbing materials. In Chapter 5 we apply this technique to *in situ* imaging of atoms in ultracold atoms.

Appendix 2.A Calculating dipole matrix elements

The dipole operator is an irreducible spherical tensor and we can therefore use the Wigner-Eckart theorem to re-express the matrix elements [76, 77]

$$\mathbf{d}^{+}_{F'm',Fm} = \langle J'IF'||\mathbf{d}||JIF\rangle \sum_{\sigma}\langle F1; m\sigma|F'm'\rangle \boldsymbol{\epsilon}^{*}_{\sigma}. \tag{2.29}$$

Here $\langle J'IF'||\mathbf{d}||JIF\rangle$ is the reduced matrix element for the transition between F and F' and $\langle F1; m\sigma|F'm'\rangle$ is a Clebsch-Gordan coefficient, which can itself be re-expressed in terms of the Wigner $3j$-symbol

$$\langle F1; m\sigma|F'm'\rangle = (-1)^{F-1+m'}\sqrt{2F'+1}\begin{pmatrix} F & 1 & F' \\ m & \sigma & -m' \end{pmatrix}. \tag{2.30}$$

The reduced matrix element can be reduced further using the relation [76]

$$\langle J'IF'||\mathbf{d}||JIF\rangle = (-1)^{J'+I+1+F}\sqrt{(2J'+1)(2F+1)}\langle J'||\mathbf{d}||J\rangle \begin{Bmatrix} J' & J & 1 \\ F & F' & I \end{Bmatrix}, \tag{2.31}$$

where $\langle J'||\mathbf{d}||J\rangle$ is a further reduced matrix element and the curly bracket is the Wigner $6j$-symbol. The reduced element can be related directly to the lifetime of the excited J' state

$$\frac{1}{\tau} = \frac{\omega^3}{3\pi\epsilon_0\hbar c^3}|\langle J'||\mathbf{d}||J\rangle|^2. \tag{2.32}$$

In total we have

$$\mathbf{d}^{+}_{F'm',Fm} = (-1)^{J'+I+1+F}\sqrt{(2J'+1)(2F+1)}\langle J'||\mathbf{d}||J\rangle \begin{Bmatrix} J' & J & 1 \\ F & F' & I \end{Bmatrix} \times \sum_{\sigma}\langle F1; m\sigma|F'm'\rangle \boldsymbol{\epsilon}^{*}_{\sigma}. \tag{2.33}$$

This new representation allows us to calculate relative transition rates between any of the sub levels of F and F' using only the Clebsch-Gordan coefficients and Wigner $6j$-symbols.

Appendix 2.B Polarisability tensor

In general the polarisability tensor is

$$\overleftrightarrow{\alpha}_{J_1F_1m_1,J_2F_2m_2} = \sum_{J',F',m'} \frac{\langle J_2IF_2m_2|\mathbf{d}|J'IF'm'\rangle \otimes \langle J'IF'm'|\mathbf{d}|J_1IF_1m_1\rangle}{\hbar\Delta_{J',F'}}. \quad (2.34)$$

We now consider this expression for the specific case of Alkali atoms and transitions from the $J = 1/2$ ground state to the excited $J' = 1/2, 3/2$ states. If we are far detuned from the the excited state levels we can simplify the polarisability tensor by approximating $\Delta_{J',F'} \approx \Delta_{J'}$ in Equation (2.34). We then have

$$\overleftrightarrow{\alpha}_{J,F_1,m_1,F_2,m_2} = \sum_{J'} \frac{1}{\hbar\Delta_{J'}} \langle F_2, m_2|\mathbf{D}^-_{J'} \otimes \mathbf{D}^+_{J'}|F_1, m_1\rangle, \quad (2.35)$$

where $\mathbf{D}^+_{J'} = \sum_{m_J,m_{J'}} |J'm_{J'}\rangle\langle J'm_{J'}|\mathbf{d}|Jm_J\rangle\langle Jm_J|$ and $\mathbf{D}^-_{J'} = (\mathbf{D}^+_{J'})^\dagger$.

Now $\tilde{\mathbf{E}}^-(\mathbf{r})(\mathbf{D}^- \otimes \mathbf{D}^+)\tilde{\mathbf{E}}^+(\mathbf{r}) = \sum_{i,j} \tilde{E}^-(\mathbf{r})_i \tilde{E}^+(\mathbf{r})_j D^-_i D^+_j$ (we have dropped the J' subscript temporarily for notational convenience) and $D^-_i D^+_j$ can be decomposed into irreducible tensors of rank 0,1 and 2 [76] as follows

$$D^-_i D^+_j = \frac{1}{3}(\mathbf{D}^- \cdot \mathbf{D}^+)\delta_{i,j} + \frac{1}{2}(D^-_i D^+_j - D^-_j D^+_i) + \left[\frac{1}{2}(D^-_i D^+_j + D^-_j D^+_i) - \frac{1}{3}(\mathbf{D}^- \cdot \mathbf{D}^+)\delta_{i,j}\right]. \quad (2.36)$$

Because $D^-_i D^+_j$ acts on the two-dimensional spin-1/2 Hilbert space where all operators are either scalar or vectors, the rank 2 part must be identically zero. We can then break the polarisability tensor into two parts $\overleftrightarrow{\alpha}_{F_1,m_1,F_2,m_2} = \overleftrightarrow{\alpha}^{(0)}_{F_1,m_1,F_2,m_2} +$

$\overleftrightarrow{\alpha}^{(1)}_{F_1,m_1,F_2,m_2}$, where

$$\tilde{\mathbf{E}}^-(\mathbf{r})\overleftrightarrow{\alpha}^{(0)}_{F_1,m_1,F_2,m_2}\tilde{\mathbf{E}}^+(\mathbf{r}) = \sum_{J'}\frac{1}{3\hbar\Delta_{J'}}\langle F_2,m_2|(\mathbf{D}^-_{J'}\cdot\mathbf{D}^+_{J'})|F_1,m_1\rangle(\tilde{\mathbf{E}}^-(\mathbf{r})\cdot\tilde{\mathbf{E}}^+(\mathbf{r})) \tag{2.37}$$

and

$$\tilde{\mathbf{E}}^-(\mathbf{r})\overleftrightarrow{\alpha}^{(1)}_{F_1,m_1,F_2,m_2}\tilde{\mathbf{E}}^+(\mathbf{r}) = \sum_{J'}\frac{1}{2\hbar\Delta_{J'}}\langle F_2,m_2|(\mathbf{D}^-_{J'}\times\mathbf{D}^+_{J'})\cdot(\tilde{\mathbf{E}}^-(\mathbf{r})\times\tilde{\mathbf{E}}^+(\mathbf{r}))|F_1,m_1\rangle \tag{2.38}$$

Using the results from Appendix 2.A we find that

$$\mathbf{D}^-_{J'}\cdot\mathbf{D}^+_{J'} = \frac{(2J'+1)|\langle J'||\mathbf{d}||J\rangle|^2}{2}\sum_{m_J}|Jm_J\rangle\langle Jm_J|, \tag{2.39}$$

and Equation (2.37) then gives the state independent light shift

$$\tilde{\mathbf{E}}^-(\mathbf{r})\overleftrightarrow{\alpha}^{(0)}_{J,F_1,m_1,F_2,m_2}\tilde{\mathbf{E}}^+(\mathbf{r}) = a_0(\Delta_{3/2})\tilde{\mathbf{E}}^-(\mathbf{r})\cdot\tilde{\mathbf{E}}^+(\mathbf{r})\delta_{F_1,F_2}\delta_{m_1,m_2}, \tag{2.40}$$

where

$$a_0(\Delta_{3/2}) = \sum_{J'}\frac{(2J'+1)|\langle J'||\mathbf{d}||J\rangle|^2}{6\hbar(\Delta_{3/2}-\Delta_{fs}\delta_{1/2,J'})}, \tag{2.41}$$

and $\Delta_{fs} = \omega_{J'=3/2} - \omega_{J'=1/2}$. Furthermore, the cross product term in Equation (2.38) is proportional to the angular momentum operator $\hat{\mathbf{J}}$, where

$$\mathbf{D}^-_{J'}\times\mathbf{D}^+_{J'} = \frac{4i(-1)^{J-J'}|\langle J'||\mathbf{d}||J\rangle|^2}{3\hbar}\hat{\mathbf{J}}. \tag{2.42}$$

For $F_1 = F_2$ we can then use the projection theorem to get

$$\tilde{\mathbf{E}}^-(\mathbf{r})\overleftrightarrow{\alpha}^{(1)}_{J,F_1,m_1,F_1,m_2}\tilde{\mathbf{E}}^+(\mathbf{r}) = a_1(\Delta_{3/2})\langle F_1m_2|(\hat{\mathbf{F}}/\hbar)\cdot(\tilde{\mathbf{E}}^-(\mathbf{r})\times\tilde{\mathbf{E}}^+(\mathbf{r}))|F_1m_1\rangle \tag{2.43}$$

where

$$a_1(\Delta_{3/2}) = \sum_{J'} \frac{i2(-1)^{F_1-I-J'}|\langle J'||\mathbf{d}||J\rangle|^2}{3(2I+1)\hbar(\Delta_{3/2} - \Delta_{fs}\delta_{1/2,J'})}. \tag{2.44}$$

In Equations (2.41) and (2.44), if one of the detunings for the $J = 1/2$ or $J = 3/2$ levels is much less than the other, then this level will make the dominant contribution to the light-matter interaction. In this case we can reduce the sum to include just that level, and the signs of the coupling coefficients $a_0(\Delta_{3/2})$ and $a_1(\Delta_{3/2})$ depend directly on the sign of the detuning from that level.

Chapter 3

Light scattering from superfluids and Mott insulators

As we described in Section 2.2.3, the Bose-Hubbard model predicts a phase transition between a superfluid and an insulating state that have significantly different properties. The characterisation of this transition has been a focal point of research, and a number of authors have considered what light scattered from the atomic gas might reveal about the many-body structure. In particular, the response of the atomic systems to Bragg scattering, where photons scatter via a stimulated process from one laser into another, was investigated theoretically [78, 79, 80, 81] and studied in an experiment [22], where signatures of the superfluid and Mott insulator states were detected. Schemes involving light scattering into a cavity, for which there is potentially strong light-matter coupling, have also been studied theoretically, where the photons transmitted from the cavity reveal information about the many-body state [30, 31, 82, 29, 83]. The majority of theoretical work done has made the zero temperature approximation for the gas, however, finite temperature effects have been investigated for the superfluid and Mott cases [41], and also for

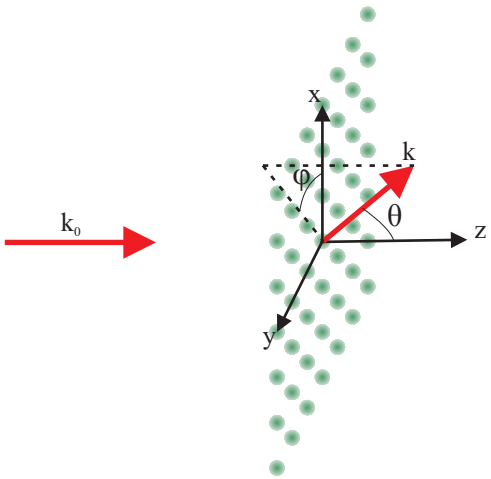

Figure 3.1: Light scattering scheme. The lattice is illuminated by a laser beam with wave vector $\mathbf{k}_0$. Light is then scattered to other modes $\mathbf{k}$ with polar coordinates θ and ϕ. In our examples of light scattering in this chapter the optical lattices are two dimensional square lattices with lattice translation vectors $a\hat{\mathbf{x}}$ and $a\hat{\mathbf{y}}$, and the input light has $\mathbf{k}_0 = \pi\hat{\mathbf{z}}/a$. In this coordinate system we then have $\Delta\mathbf{k} = \pi(\sin\theta\cos\phi, \sin\theta\sin\phi, 1-\cos\theta)/a$.

a closely related problem involving a Fermi gas [40].

Here we are interested in what light scattering that is not stimulated by another laser or by a cavity tells us about the many-body state. The aim being to reveal information about the atoms while they remain *in situ* with a relatively simple experimental implementation, only requiring a laser to be shone on the atoms, as depicted on Figure 3.1, followed by the detection of scattered photons, possible after collection by a lens. This would remove the need for a cavity or the need to destructively image the atomic sample as is the case for Bragg scattering. However, this complicates the theoretical treatment because in this case there is less restriction on the final energy state of the scattered photons and the full band structure of the optical lattice must be taken into account, something which has been neglected in previous works. We present here a treatment of light scattering from the superfluid and Mott insulating states that includes both the higher bands and the effects of non-zero temperature.

3.1 First order light scattering

Non-resonant light scattering from an ultracold gas can occur in two ways, the first involves the diffraction of light due to the non-uniform density of the gas which leaves the gas unchanged, while the second involves the creation of excitations in the gas where the light transfers momentum and/or energy to the gas. In the following we see how these processes occur when laser light is scattered from atoms in first order perturbation theory.

We consider light-matter interactions where the atom can be treated as a two-level system, as may be the case because of angular momentum considerations. For example in Rb^{87}, the transition $|5^2S_{1/2}, F = 2, m_F = 2\rangle \rightarrow |5^2P_{3/2}, F = 3, m_F = 3\rangle$ that is excited by σ^+-polarised light is a cycling transition, where because of the polarisation of the input light only one excited state can take part, which in turn can only decay to the initial ground state. In this case the contributions from the $5^2P_{1/2}$ level in the coupling coefficients in Equations (2.41) and (2.44) cancel exactly. For this type of cycling transition the interaction Hamiltonians from Equations (2.14) and (2.15) sum to give

$$H = -g \int d\mathbf{r} \hat{\Psi}^\dagger(\mathbf{r}) \tilde{\mathbf{E}}^-(\mathbf{r}) \cdot \tilde{\mathbf{E}}^+(\mathbf{r}) \hat{\Psi}(\mathbf{r}), \tag{3.1}$$

where $g = (a_0(\Delta_{3/2}) + i(I + 1/2)a_1(\Delta_{3/2})) = |\langle J' = 3/2||\mathbf{d}||J = 1/2\rangle|^2/(\hbar\Delta_{3/2})$.

In the interaction picture we have $\hat{H}_I(t) = e^{i\hat{H}_0 t/\hbar} \hat{H} e^{-i\hat{H}_0 t/\hbar}$ and the time evolution operator is given by the integral equation $U_I(t, 0) = 1 - \frac{i}{\hbar} \int_0^t dt' \hat{H}_I(t') U_I(t', 0)$ [46]. For a weak perturbation the evolution of the state is given approximately by expanding this integral equation to first order, giving

$$|\Psi(t)\rangle_I = \left(1 - \frac{i}{\hbar} \int_0^t dt' \hat{H}_I\right) |\Psi(0)\rangle_I. \tag{3.2}$$

We take the initial state of the system to be an atomic eigenstate $|\Psi_u\rangle$ and a laser represented by the classical field $\tilde{\mathbf{E}}^+(\mathbf{r}) = \frac{\mathcal{E}}{2} e^{i\mathbf{k}_0\cdot\mathbf{r}}\boldsymbol{\epsilon}_0$. The first order coupling then leads to photons being scattered from the laser into other modes $(\mathbf{k}, \lambda)$ with wave vector $\mathbf{k}$, frequency $\omega_\mathbf{k}$ and polarisation $\boldsymbol{\epsilon}_\lambda(\mathbf{k})$, resulting in a momentum change $\Delta\mathbf{k} = \mathbf{k}_0 - \mathbf{k}$ and energy change $\Delta\omega_\mathbf{k} = \omega_0 - \omega_\mathbf{k}$. The probability at time t of the system being in a new atomic eigenstate $|\Psi_v\rangle$ with an additional photon in the mode $(\mathbf{k}, \lambda)$ is then

$$\left|\left\langle \mathbf{k}\right|\otimes\left\langle \Psi_v\right|\frac{1}{\hbar}\int_0^t dt'\hat{H}_I\left|\Psi_u\right\rangle\otimes\left|0\right\rangle\right|^2 = tG_\lambda(\mathbf{k}) \times \delta_t((E_v - E_u)/\hbar - \Delta\omega_\mathbf{k})\left|\int d\mathbf{r} e^{i\Delta\mathbf{k}\cdot\mathbf{r}}\langle\Psi_v|\hat{\Psi}^\dagger(\mathbf{r})\hat{\Psi}(\mathbf{r})|\Psi_u\rangle\right|^2 \quad (3.3)$$

where $G_\lambda(\mathbf{k}) = |g\mathcal{E}\boldsymbol{\epsilon}^*_\lambda(\mathbf{k})\cdot\boldsymbol{\epsilon}_0|^2\omega_\mathbf{k}/(8\hbar\epsilon_0(2\pi)^2)$ is the coupling constant between the electromagnetic field modes and E_j is the unperturbed energy of the state $|\Psi_j\rangle$. The function $\delta_t(\omega) = 2\sin^2(\omega t/2)/(\pi t\omega^2)$ approaches the Dirac delta function $\delta(\omega)$ as the interaction time t approaches infinity, enforcing energy conservation.

For σ^+-polarised input laser light we can sum over polarisations in the coupling to get $G(\mathbf{k}) = \sum_\lambda G_\lambda(\mathbf{k}) = |g\mathcal{E}|^2(1+\cos(\theta)^2)\omega_\mathbf{k}/(16\hbar\epsilon_0(2\pi)^2)$. The total rate of scattering photons with wave vector $\mathbf{k}$ and frequency $\omega_\mathbf{k}$ of either polarisation is then

$$\Gamma(\mathbf{k}, \omega_\mathbf{k}) = G(\mathbf{k})S(\mathbf{k}_0 - \mathbf{k}, \omega_{\mathbf{k}_0} - \omega_\mathbf{k}), \quad (3.4)$$

where $S(\Delta\mathbf{k}, \Delta\omega_\mathbf{k})$ is the dynamic structure factor [84]. For a finite temperature system, in the canonical ensemble with partition function Z, the dynamic structure factor is [85, 86]

$$S(\Delta\mathbf{k}, \Delta\omega_\mathbf{k}) = \sum_{u,v}\delta((E_v - E_u)/\hbar - \Delta\omega_\mathbf{k})\left|\int d\mathbf{r} e^{i\Delta\mathbf{k}\cdot\mathbf{r}}\langle\Psi_v|\hat{\Psi}^\dagger(\mathbf{r})\hat{\Psi}(\mathbf{r})|\Psi_u\rangle\right|^2 \times e^{-E_u/(k_BT)}/Z. \quad (3.5)$$

The structure factor can be divided up into two parts, the first with $u = v$ describes classical diffraction, which results in no energy or momentum transfer to the gas, that is, the light scattering is *elastic*. The second part, where $u \neq v$, describes *inelastic* light scattering that results in excitations of the gas.

For non-resonant light scattering the frequency change $\Delta\omega_{\mathbf{k}}$ is determined by the difference in energies between the initial and final atom many-body states. For scattering from ultracold atoms these energy differences are all many orders of magnitude less than the frequency of the input light. To a very good approximation we then have $\mathbf{k} = k_0\hat{\mathbf{k}}$, where $\hat{\mathbf{k}}$ has associated angles θ and ϕ as shown in Figure 3.1. To get the total rate of photon scattering in direction $\hat{\mathbf{k}}$, we integrate over frequency, giving

$$I_{total}(\hat{\mathbf{k}}) = I_{atom}(\theta) \times S(\mathbf{k}_0 - k_0\hat{\mathbf{k}}), \tag{3.6}$$

where $I_{atom}(\theta) = 9I_{in}\Gamma^2(1+\cos(\theta)^2)/(32\hbar c k_0^3\Delta_{3/2}^2)$ is the scattering distribution resulting from the electronic structure of the atom and laser intensity $I_{in} = \epsilon_0 c|\mathcal{E}|^2/2$, and

$$S(\Delta\mathbf{k}) = \sum_u \int d\mathbf{r}d\mathbf{r}' e^{i\Delta\mathbf{k}\cdot(\mathbf{r}-\mathbf{r}')}\langle\Psi_u|\hat{\Psi}^\dagger(\mathbf{r}')\hat{\Psi}(\mathbf{r}')\hat{\Psi}^\dagger(\mathbf{r})\hat{\Psi}(\mathbf{r})|\Psi_u\rangle e^{-E_u/(k_BT)}/Z \tag{3.7}$$

is the scattering distribution due to the spatial structure of the atomic sample, known as the static structure factor [86]. In the expression above we have simplified the static structure factor using the closure relation for the atomic eigenstates.

The static structure factor applies in the perturbative regime, where it has been used successfully to describe neutron scattering from liquid helium [84] and to calculate the response of ultracold gases to Bragg excitation [10]. For our purposes it allows us to calculate how light scatters from atoms in optical lattice from the correlation function $\langle\Psi_u|\hat{\Psi}^\dagger(\mathbf{r}')\hat{\Psi}(\mathbf{r}')\hat{\Psi}^\dagger(\mathbf{r})\hat{\Psi}(\mathbf{r})|\Psi_u\rangle$. To find this correlation function we need to follow different approaches for the superfluid and Mott insulator

cases. We begin in the next section by describing the Bogoliubov method for the superfluid case.

3.2 Bogoliubov theory of weakly interacting Bose gases in optical lattices

In Section 2.2.3 we described the Bose-Hubbard model that resulted from expanding the many-body Hamiltonian in terms of the Wannier functions. In the superfluid case the atoms are not localised and, particularly for light scattering, it is more intuitive to expand in the Bloch basis. The expanded atomic field operator is then $\hat{\Psi}(\mathbf{r}) = \sum_{\mathbf{q}} \hat{b}_{\mathbf{q}} \phi_{\mathbf{q}}(\mathbf{r})$ and we get from Equation (2.19) the following atomic Hamiltonian,

$$H = \sum_{\mathbf{q}} E_{\mathbf{q}} \hat{b}^{\dagger}_{\mathbf{q}} \hat{b}_{\mathbf{q}} + \frac{1}{2} \sum_{\mathbf{q_1},\mathbf{q_2},\mathbf{q_3},\mathbf{q_4}} U_{\mathbf{q_1},\mathbf{q_2},\mathbf{q_3},\mathbf{q_4}} \hat{b}^{\dagger}_{\mathbf{q_1}} \hat{b}^{\dagger}_{\mathbf{q_2}} \hat{b}_{\mathbf{q_3}} \hat{b}_{\mathbf{q_4}} - \mu \hat{N}, \tag{3.8}$$

where

$$U_{\mathbf{q_1},\mathbf{q_2},\mathbf{q_3},\mathbf{q_4}} = \frac{4\pi\hbar^2 a_s M}{m_a} \int d\mathbf{r} \phi^*_{\mathbf{q_1}}(\mathbf{r}) \phi^*_{\mathbf{q_2}}(\mathbf{r}) \phi_{\mathbf{q_3}}(\mathbf{r}) \phi_{\mathbf{q_4}}(\mathbf{r}). \tag{3.9}$$

Here for notational convenience we have assumed the band index of the Bloch states is contained in the generalised quasi-momentum $\mathbf{q}$, and the theory below includes all bands. We use the grand canonical form of the Hamiltonian here to simplify the derivation below, number conserving methods are described elsewhere [87, 88, 89, 90, 9].

At zero temperature, atoms in a non-interacting Bose gas condense into the zero momentum Bloch state $\phi_{\mathbf{0}}(\mathbf{r})$. For weak interactions this ground state is perturbed, and the new ground state and elementary excitations of the gas are found using Bogoliubov theory [91]. Extensions of Bogoliubov's theory to Bose gases in optical lattices have been made [92, 93], but work in the tight binding approximation.

Here, by working in the Bloch basis we do not need to make this approximation.

Bogoliubov theory progresses by replacing the operators $\hat{b}_{\mathbf{0}}$ and $\hat{b}_{\mathbf{0}}^{\dagger}$ of the highly populated zero momentum Bloch state by the c-number $\sqrt{N_0} = \sqrt{\langle \hat{b}_{\mathbf{0}}^{\dagger} \hat{b}_{\mathbf{0}} \rangle}$. Minimising the energy to zeroth order with respect to N_0 then gives the chemical potential $\mu = E_{\mathbf{0}} + N_0 U_{\mathbf{0},\mathbf{0},\mathbf{0},\mathbf{0}}$. Assuming the non-zero momentum Bloch states have population much smaller than N_0, we can neglect terms above quadratic order in these modes and reduce the atomic Hamiltonian to

$$H = -\frac{1}{2} N_0^2 U_{\mathbf{0}} + \sum_{\mathbf{q} \neq \mathbf{0}} \left(\hat{b}_{\mathbf{q}}^{\dagger} \hat{b}_{\mathbf{q}} \tilde{E}_{\mathbf{q}} + \frac{1}{2} N_0 U_{\mathbf{q}} (\hat{b}_{\mathbf{q}}^{\dagger} \hat{b}_{-\mathbf{q}}^{\dagger} + \hat{b}_{\mathbf{q}}^{\dagger} \hat{b}_{-\mathbf{q}}^{\dagger}) \right), \tag{3.10}$$

where $U_{\mathbf{0}} = U_{\mathbf{0},\mathbf{0},\mathbf{0},\mathbf{0}}$, $U_{\mathbf{q}} = U_{\mathbf{q},\mathbf{0},\mathbf{0},\mathbf{q}}$ and $\tilde{E}_{\mathbf{q}} = E_{\mathbf{q}} - E_{\mathbf{0}} - N_0 U_{\mathbf{0}} + 2 N_0 U_{\mathbf{q}}$.

This quadratic Hamiltonian is then diagonalised via the Bogoliubov transformation [91]

$$\hat{b}_{\mathbf{q}}^{\dagger} = u_{\mathbf{q}} \hat{\beta}_{\mathbf{q}}^{\dagger} - v_{\mathbf{q}} \hat{\beta}_{-\mathbf{q}}, \qquad \hat{b}_{\mathbf{q}} = u_{\mathbf{q}} \hat{\beta}_{\mathbf{q}} - v_{\mathbf{q}} \hat{\beta}_{-\mathbf{q}}^{\dagger}, \tag{3.11}$$

where the Bogoliubov transformation coefficients are given by

$$u_{\mathbf{q}} = \sqrt{\frac{1}{2} \left(\frac{\tilde{E}_{\mathbf{q}}}{\hbar \omega_{\mathbf{q}}} + 1 \right)} \qquad \text{and} \qquad v_{\mathbf{q}} = \sqrt{\frac{1}{2} \left(\frac{\tilde{E}_{\mathbf{q}}}{\hbar \omega_{\mathbf{q}}} - 1 \right)}. \tag{3.12}$$

The resulting Hamiltonian is then

$$H = -\frac{1}{2} N_0^2 U_{\mathbf{0}} + \frac{1}{2} \sum_{\mathbf{q} \neq \mathbf{0}} (\hbar \omega_{\mathbf{q}} - \tilde{E}_{\mathbf{q}}) + \sum_{\mathbf{q} \neq \mathbf{0}} \hbar \omega_{\mathbf{q}} \hat{\beta}_{\mathbf{q}}^{\dagger} \hat{\beta}_{\mathbf{q}}, \tag{3.13}$$

where

$$\hbar \omega_{\mathbf{q}} = \sqrt{\tilde{E}_{\mathbf{q}}^2 - N_0^2 U_{\mathbf{q}}^2}. \tag{3.14}$$

The operators $\hat{\beta}_{\mathbf{q}}^{\dagger}$ and $\hat{\beta}_{\mathbf{q}}$ are interpreted as the creation and annihilation operators

of non-interacting bosonic quasi-particles with energy $\hbar\omega_{\mathbf{q}}$. At zero temperature the ground state of the system is the quasi-particle vacuum, while for finite temperature T the population of the quasi-particle modes is given by the Bose-Einstein distribution [6, 94]

$$\langle \hat{\beta}^\dagger_{\mathbf{q}'} \hat{\beta}_{\mathbf{q}'} \rangle = \frac{\delta_{\mathbf{q},\mathbf{q}'}}{e^{\hbar\omega_{\mathbf{q}}/k_b T} - 1} = \delta_{\mathbf{q},\mathbf{q}'} n_{\mathbf{q}}. \tag{3.15}$$

Furthermore, we have $\langle \hat{\beta}_{\mathbf{q}} \rangle = \langle \hat{\beta}^\dagger_{\mathbf{q}} \rangle = 0$ and $\langle \hat{\beta}^\dagger_{\mathbf{q}} \hat{\beta}_{\mathbf{q}} \hat{\beta}^\dagger_{\mathbf{q}'} \hat{\beta}_{\mathbf{q}'} \rangle = n_{\mathbf{q}} n_{\mathbf{q}'} + \delta_{\mathbf{q},\mathbf{q}'}(n_{\mathbf{q}}+1) n_{\mathbf{q}'}$, which we will need to calculate the correlation function in the structure factor.

The above quantities depend implicitly on the condensate number N_0, which is in turn restricted by the following relation for the number operator $\hat{N} = \sum_{\mathbf{q}} \hat{b}^\dagger_{\mathbf{q}} \hat{b}_{\mathbf{q}}$,

$$\langle \hat{N} \rangle = \sum_{\mathbf{q}} N_{\mathbf{q}} = N_0 + \sum_{\mathbf{q}\neq 0} \left(u^2_{\mathbf{q}} n_{\mathbf{q}} + v^2_{\mathbf{q}} (n_{\mathbf{q}} + 1) \right). \tag{3.16}$$

For a fixed $\langle \hat{N} \rangle = N$, Equations (3.12), (3.14) and (3.16) must be solved self-consistently.

As noted above, the Bogoliubov approximation only includes the contributions to the interaction energy proportional to N_0, and its validity is therefore limited to the regime where the number of quasi-particles is a small fraction of N_0. In this thesis we limit our calculations so that this fraction is less than one tenth.

3.3 Dynamic structure factor in the Bogoliubov regime

We may now proceed to calculate the dynamic structure factor using the Bogoliubov theory. Expanding the atomic field operators in the Bloch basis gives

$$S(\Delta\mathbf{k},\Delta\omega_{\mathbf{k}}) = \sum_{u,v}\delta((E_v-E_u)/\hbar-\Delta\omega_{\mathbf{k}}) \times\left|\sum_{\mathbf{q_1},\mathbf{q_2}}\langle\Psi_v|\hat{b}^{\dagger}_{\mathbf{q}_2}\hat{b}_{\mathbf{q}_1}|\Psi_u\rangle f_{\mathbf{q}_1,\mathbf{q}_2}(\Delta\mathbf{k})\right|^2 e^{-E_u/(k_BT)}/Z, \quad (3.17)$$

where

$$f_{\mathbf{q}_1,\mathbf{q}_2}(\Delta\mathbf{k}) = M\int d\mathbf{r}\phi^*_{\mathbf{q_2}}(\mathbf{r})\phi_{\mathbf{q_1}}(\mathbf{r})e^{i\Delta\mathbf{k}\cdot(\mathbf{r})}. \quad (3.18)$$

Again for notational convenience we have assumed the band index is contained in the generalised vector $\mathbf{q}$. We can now calculate the structure factor in the Bogoliubov regime by replacing $\hat{b}_{\mathbf{0}}$ and $\hat{b}^{\dagger}_{\mathbf{0}}$ by $\sqrt{N_0}$ and using the Bogoliubov transformation given by Equation (3.11). As a result we get three components.

The zeroth order component,

$$S_0(\Delta\mathbf{k},\Delta\omega_{\mathbf{k}}) = \delta(\Delta\omega_{\mathbf{k}})\left[\left|\sum_{\mathbf{q}}N_{\mathbf{q}}f_{\mathbf{q},\mathbf{q}}(\Delta\mathbf{k})\right|^2 + \sum_{\mathbf{q}\neq\mathbf{0}}|f_{\mathbf{q},\mathbf{q}}(\Delta\mathbf{k})|^2(n_{\mathbf{q}}+1)n_{\mathbf{q}}(u^2_{\mathbf{q}}+v^2_{\mathbf{q}})^2\right], \quad (3.19)$$

describes elastic light scattering that does not cause excitations in the lattice. In this expression the first term in the square brackets is the classical diffraction pattern due to the density distribution, while the second term results from the number fluctuations in the Bogoliubov modes at finite temperature. If we expand out the first term using Wannier functions, and keep at most nearest neighbour

terms, we find Equation (53) of Rist *et al.* [81]. In that paper the authors described part of this term as resulting from 'light-assisted tunnelling', here, working in the Bloch basis, this term arises purely from diffraction from the density.

The first order component is

$$S_1(\Delta\mathbf{k},\Delta\omega_\mathbf{k}) = N_0\sum_{\mathbf{q}\neq\mathbf{0}}|f_{\mathbf{q},\mathbf{0}}(\Delta\mathbf{k})|^2\delta(\omega_\mathbf{q}-\Delta\omega_\mathbf{k})(u_\mathbf{q}-v_\mathbf{q})^2(n_q+1) + N_0\sum_{\mathbf{q}\neq\mathbf{0}}|f_{\mathbf{0},\mathbf{q}}(\Delta\mathbf{k})|^2\delta(\omega_\mathbf{q}+\Delta\omega_\mathbf{k})(u_\mathbf{q}-v_\mathbf{q})^2 n_q, \quad (3.20)$$

and describes inelastic light scattering that excites atoms out of, or back into, the condensate mode. This involves the creation or destruction of quasi-particles with quasi-momentum $\mathbf{q}$, where the light is frequency shifted by $\omega_\mathbf{q}$.

The second order component involves excitations in two quasi-particle modes and is

$$S_2(\Delta\mathbf{k},\Delta\omega_\mathbf{k}) = \sum_{\mathbf{q}\neq\mathbf{p},\mathbf{q}\neq\mathbf{0},\mathbf{p}\neq\mathbf{0}}(u_\mathbf{q}u_\mathbf{p}+v_\mathbf{p}v_\mathbf{q})^2|f_{\mathbf{q},\mathbf{p}}(\Delta\mathbf{k})|^2(n_\mathbf{q}+1)n_\mathbf{p}\delta(\omega_\mathbf{q}-\omega_\mathbf{p}-\Delta\omega_\mathbf{k}) + \frac{1}{2}\sum_{\mathbf{q}\neq\mathbf{0},\mathbf{p}\neq\mathbf{0}}(u_\mathbf{q}v_\mathbf{p}+u_\mathbf{p}v_\mathbf{q})^2|f_{\mathbf{q},\mathbf{p}}(\Delta\mathbf{k})|^2\left[(n_\mathbf{q}+1)(n_\mathbf{p}+1)\delta(\omega_\mathbf{q}+\omega_\mathbf{p}-\Delta\omega_\mathbf{k}) + n_\mathbf{q}n_\mathbf{p}\delta(\omega_\mathbf{q}+\omega_\mathbf{p}+\Delta\omega_\mathbf{k})\right]. \quad (3.21)$$

Three processes contribute to this component: the destruction of a quasi-particle along with the creation of a quasi-particle, the creation of two quasi-particles, and the destruction of two quasi-particles.

In the above description, by working in the Bloch basis and making use of the Bogoliubov theory in the Bloch basis derived earlier, we have extended other works on the subject [80, 41, 81] by not making the tight binding approximation at any point or needing to neglect any terms in the dynamic structure factor. We have also not restricted ourselves to scattering events within the lowest band, however to

calculate the contributions from the higher bands we need to calculate the higher band Bloch functions. We will see in the next section, where we are only concerned with the angular dependence of the light scattering, that these contributions can be calculated in a more straightforward manner.

3.4 Angular dependence of light scattering in the Bogoliubov regime

In the previous section we studied the dynamic structure factor in the Bogoliubov regime, giving us a description of the amount of photons scattered at a particular angle at each frequency. In this section we are purely concerned with the angular distribution of the scattered photons. We have in mind an experiment where laser light is scattered from the atoms in the lattice and the intensity is examined at various angles to reveal information about the atoms. In this situation the frequency information is not measured and instead we measure the static structure factor. This allows for simplification of the multiple band problem and we will show that the contribution from the upper bands can be calculated using only information about the lowest band.

The full expression for the static structure factor, with the band index now written explicitly, is

$$S(\Delta\mathbf{k}) = \sum_{\substack{\mathbf{q_1},\mathbf{q_2},\mathbf{q_3},\mathbf{q_4} \\ \mathbf{m_1},\mathbf{m_2},\mathbf{m_3},\mathbf{m_4}}} \langle \hat{b}^\dagger_{\mathbf{q_1},\mathbf{m_1}} \hat{b}_{\mathbf{q_2},\mathbf{m_2}} \hat{b}^\dagger_{\mathbf{q_3},\mathbf{m_3}} \hat{b}_{\mathbf{q_4},\mathbf{m_4}} \rangle f^*_{\mathbf{q_1},\mathbf{m_1},\mathbf{q_2},\mathbf{m_2}}(\Delta\mathbf{k}) f_{\mathbf{q_4},\mathbf{m_4},\mathbf{q_3},\mathbf{m_3}}(\Delta\mathbf{k}). \tag{3.22}$$

For sufficiently low temperatures all the atoms reside initially in the lowest band of the optical lattice, however atoms may be excited to higher bands by scattering a photon. Examining Equations (3.12) and (3.14) we see that if, for the higher bands, $\tilde{E}_\mathbf{q} \gg N_0 U_\mathbf{q}$, then $u_\mathbf{q} \sim 1$ and the quasi-particle excitations are essen-

tially particle-like. This criterion is easily satisfied in the cases we investigate, in which case the only non-zero averages in the static structure factor sum above are $\langle \hat{b}^\dagger_{\mathbf{q_1},\mathbf{0}} \hat{b}_{\mathbf{q_2},\mathbf{0}} \hat{b}^\dagger_{\mathbf{q_3},\mathbf{0}} \hat{b}_{\mathbf{q_4},\mathbf{0}} \rangle$ and $\langle \hat{b}^\dagger_{\mathbf{q_1},\mathbf{0}} \hat{b}_{\mathbf{q_2},\mathbf{m}} \hat{b}^\dagger_{\mathbf{q_2},\mathbf{m}} \hat{b}_{\mathbf{q_3},\mathbf{0}} \rangle = \langle \hat{b}^\dagger_{\mathbf{q_1},\mathbf{0}} \hat{b}_{\mathbf{q_3},\mathbf{0}} \rangle$ for $\mathbf{m} \neq \mathbf{0}$. We then have two terms, the first due to light scattering within the lowest band of the optical lattice, that is

$$S_g(\Delta\mathbf{k}) = \sum_{\mathbf{q_1},\mathbf{q_2},\mathbf{q_3},\mathbf{q_4}} \langle \hat{b}^\dagger_{\mathbf{q_1},\mathbf{0}} \hat{b}_{\mathbf{q_2},\mathbf{0}} \hat{b}^\dagger_{\mathbf{q_3},\mathbf{0}} \hat{b}_{\mathbf{q_4},\mathbf{0}} \rangle f^*_{\mathbf{q_1},\mathbf{0},\mathbf{q_2},\mathbf{0}}(\Delta\mathbf{k}) f_{\mathbf{q_4},\mathbf{0},\mathbf{q_3},\mathbf{0}}(\Delta\mathbf{k}), \tag{3.23}$$

and the second due to scattering into the upper bands of the lattice, that is

$$S_b(\Delta\mathbf{k}) = \sum_{\mathbf{q_1},\mathbf{q_2},\mathbf{q_3},\mathbf{m}\neq\mathbf{0}} \langle \hat{b}^\dagger_{\mathbf{q_1},\mathbf{0}} \hat{b}_{\mathbf{q_3},\mathbf{0}} \rangle f^*_{\mathbf{q_1},\mathbf{0},\mathbf{q_2},\mathbf{m}}(\Delta\mathbf{k}) f_{\mathbf{q_3},\mathbf{0},\mathbf{q_2},\mathbf{m}}(\Delta\mathbf{k}). \tag{3.24}$$

This term was neglected in another treatment of finite temperature light scattering [41], and we will see that this can make a considerable difference to predictions about the light scattering.

We can calculate the upper band term with the help of the sum rule

$$\sum_{\mathbf{q},\mathbf{m}} f^*_{\mathbf{q_1},\mathbf{0},\mathbf{q},\mathbf{m}}(\Delta\mathbf{k}) f_{\mathbf{q_2},\mathbf{0},\mathbf{q},\mathbf{m}}(\Delta\mathbf{k}) = \delta_{\mathbf{q_1},\mathbf{q_2}}, \tag{3.25}$$

which is implied by the completeness of the Bloch functions. Using this relation we find

$$S_b(\Delta\mathbf{k}) = N - \sum_{\mathbf{q_1},\mathbf{q_2},\mathbf{q_3}} \langle \hat{b}^\dagger_{\mathbf{q_1},\mathbf{0}} \hat{b}_{\mathbf{q_3},\mathbf{0}} \rangle f^*_{\mathbf{q_1},\mathbf{0},\mathbf{q_2},\mathbf{0}}(\Delta\mathbf{k}) f_{\mathbf{q_3},\mathbf{0},\mathbf{q_2},\mathbf{0}}(\Delta\mathbf{k}). \tag{3.26}$$

All operators are now in the lowest band and we drop the $\mathbf{0}$ band index from our notation.

We can now evaluate all the expectation values using the Bogoliubov theory. We find that light scattering within the first band is the sum of three components

$S_g(\Delta\mathbf{k}) = S_{g0}(\Delta\mathbf{k}) + S_{g1}(\Delta\mathbf{k}) + S_{g2}(\Delta\mathbf{k})$. These components result from integrating over frequency the lowest band parts of the dynamic structure factor components in Equations (3.19–3.21), and describe the same processes as their respective dynamic components. The zeroth order component, which does not result in excitations in the lattice, is

$$S_{g0}(\Delta\mathbf{k}) = \left| \sum_{\mathbf{q}} f_{\mathbf{q},\mathbf{q}}(\Delta\mathbf{k}) N_{\mathbf{q}} \right|^2 + \sum_{\mathbf{q}} |f_{\mathbf{q},\mathbf{q}}(\Delta\mathbf{k})|^2 (u_{\mathbf{q}}^2 + v_{\mathbf{q}}^2)^2 n_{\mathbf{q}}(n_{\mathbf{q}} + 1). \tag{3.27}$$

The first order component, resulting from atoms being excited out of or into the condensate mode, is

$$S_{g1}(\Delta\mathbf{k}) = N_0 \sum_{\mathbf{q}\neq\mathbf{0}} |f_{\mathbf{0},\mathbf{q}}(\Delta\mathbf{k})|^2 \left(u_{\mathbf{q}} - v_{\mathbf{q}}\right)^2 (2n_{\mathbf{q}} + 1), \tag{3.28}$$

and the second order component is

$$\begin{aligned} S_{g2}(\Delta\mathbf{k}) = & \sum_{\mathbf{q}\neq\mathbf{0},\mathbf{p}\neq\mathbf{0},\mathbf{q}\neq\mathbf{p}} |f_{\mathbf{q},\mathbf{p}}(\Delta\mathbf{k})|^2 (u_{\mathbf{q}} u_{\mathbf{p}} + v_{\mathbf{q}} v_{\mathbf{p}})^2 n_{\mathbf{q}}(n_{\mathbf{p}} + 1) \\ & + \frac{1}{2} \sum_{\mathbf{q}\neq\mathbf{0},\mathbf{p}\neq\mathbf{0}} |f_{\mathbf{q},\mathbf{p}}(\Delta\mathbf{k})|^2 (u_{\mathbf{q}} v_{\mathbf{p}} + v_{\mathbf{q}} u_{\mathbf{p}})^2 \left(n_{\mathbf{q}} n_{\mathbf{p}} + (n_{\mathbf{q}} + 1)(n_{\mathbf{p}} + 1)\right), \end{aligned} \tag{3.29}$$

which results from creation and/or destruction involving two quasi-particle modes. The intensity due to the interband scattering is given by

$$S_b(\Delta\mathbf{k}) = N - \sum_{\mathbf{p},\mathbf{q}} |f_{\mathbf{q},\mathbf{p}}(\Delta\mathbf{k})|^2 N_{\mathbf{q}}. \tag{3.30}$$

In Figure 3.2 we compare how the four components of the static structure factor vary as a function of scattering angle θ for $\phi = 0$. The static structure factor is calculated for a two dimensional lattice in the xy-plane illuminated by laser light propagating in the z-direction, with wave vector $\mathbf{k}_0 = \pi\hat{\mathbf{z}}/a$. We see that the

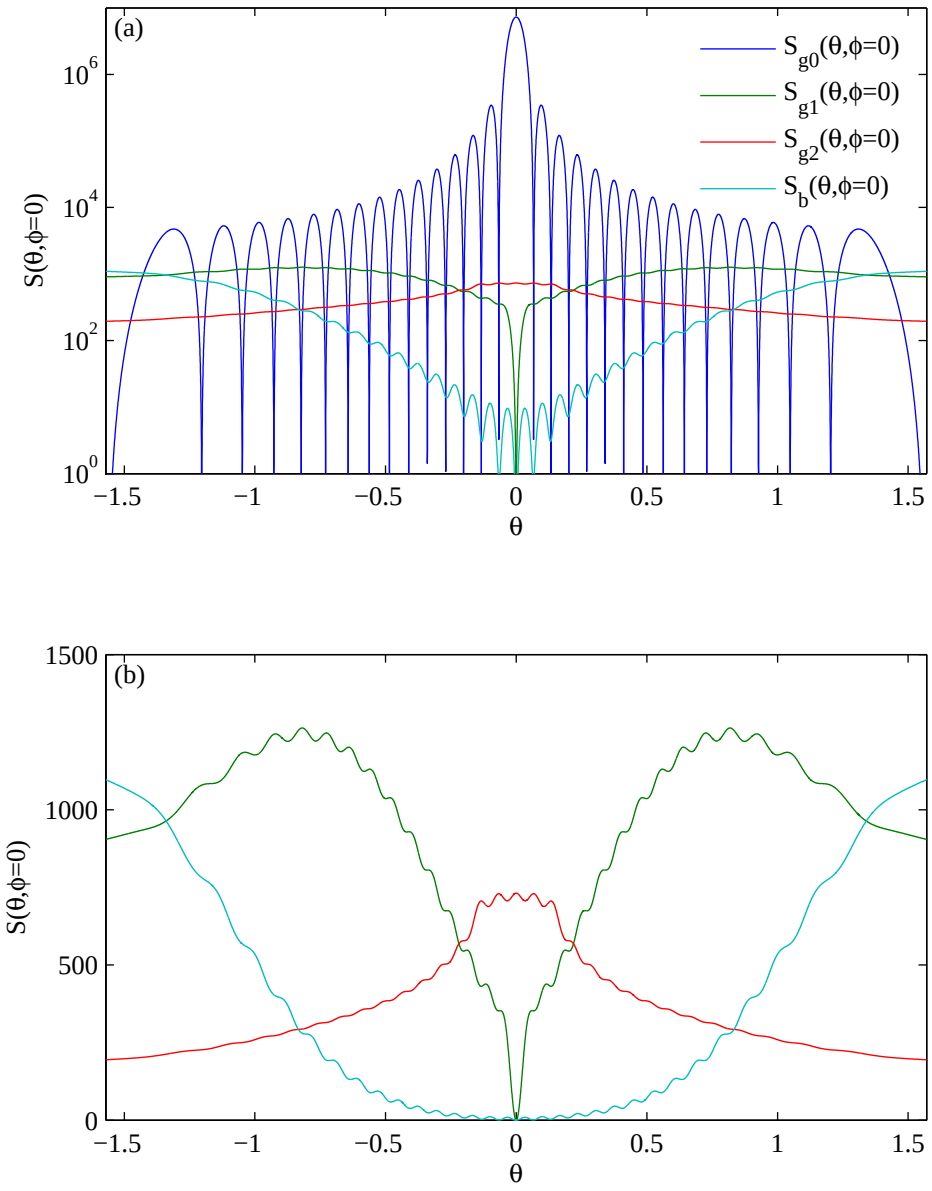

Figure 3.2: Comparison of the angular dependence of the components of the static structure factor in the superfluid regime for a 30×30 lattice with 2700 atoms. The lattice strength is $3E_R$ in the x and y directions and $20E_R$ in the z direction, leading to parameters $J = 0.11E_R$ and $U = 0.17E_R$, the temperature is $0.05E_R/k_B$ and the condensate population is $N_0 = 2526$. (a) Components of the structure factor on a log scale for $\phi = 0$. (b) Inelastic components only.

classical diffraction pattern is the dominant feature with peaks of order N^2, while the first order and band components are of order N. The second order component is significantly larger than the first order and band components near $\Delta\mathbf{k} = \mathbf{0}$, a behaviour that persists even at $T = 0$.

The behaviour of the first and second order components reflects the correlations between atoms in the lattice and quantum interference and enhancement play a role in determining their structure. We see in Figure 3.2 that the first order component vanishes as $\Delta\mathbf{k} \to 0$. This phenomenon has been recorded in Bose-liquids [95, 86] and in an experiment with a Bose condensed dilute gas, where Bragg spectroscopy was used to probe the structure factor [96]. Here the same processes are at work and we can understand the vanishing of the first order component as interference between two scattering channels resulting from the quantum depletion present in the condensate.

As we have seen in the Bogoliubov description, the s-wave scattering interaction causes perturbations to the ground state $|g\rangle$ of the non-interacting Bose gas. These perturbations are of the form $\frac{v_\mathbf{q}}{u_\mathbf{q}}\hat{b}^\dagger_\mathbf{q}\hat{b}^\dagger_{-\mathbf{q}}|g\rangle$, containing pairs of perfectly correlated atoms with equal and opposite momentum [62]. Light scattering involving a momentum change $\Delta\mathbf{k} = \mathbf{q}$ is then dominated by two channels. The first, a zero momentum atom scattering a photon and receiving a $\mathbf{q}$ momentum kick, and the second, an atom with momentum $-\mathbf{q}$ from the perturbed state scattering a photon and ending up in the ground state. These processes result in the same final state and the amplitudes interfere destructively. As q goes to zero the interference increases, approaching completely destructive interference at $q = 0$. An interesting feature of the optical lattice case, as opposed to the uniform Bose gas, is that the rate at which the first order structure factor goes to zero depends on the ratio of J to U, which can be tuned by adjusting the height of the lattice or by Feshbach resonance. By adjusting the lattice parameters and examining the light scatter-

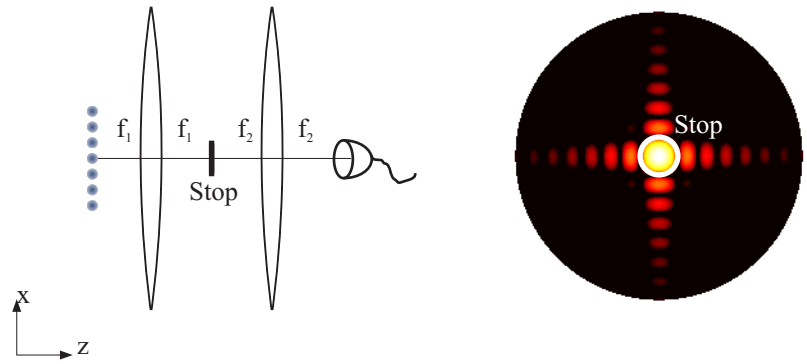

Figure 3.3: (Left) Scheme for collecting photons scattered from atoms in an optical lattice to measure the temperature of the gas. A stop placed in the centre of the Fourier plane of the first lens blocks the central diffraction peak. A second lens collects the unblocked photons which are then detected. (Right) Outline of the stop on diffraction pattern.

ing at various angles we can see how the depletion, or alternatively how number squeezing [93], in the lattice changes.

Despite involving two quasi-particle modes, the second order component can still make a significant contribution to the light scattering. This is due to quantum enhancement in the higher order scattering [97]. This component relies on the population of non-condensate modes either through depletion caused by interparticle interactions or finite temperature.

3.5 Temperature dependence of light scattering in superfluid regime

Both the first and second order components of the static structure factor depend on temperature and we can use this dependence to observe changes in temperature [41, 40]. In their recent paper, Ruostekoski *et al.* [40] proposed using non-resonant light scattered from fermions in optical lattices to determine the temperature of the Fermi gas. It is important to test whether their method could also be applied

to bosons in optical lattices, as an accurate *in situ* thermometer would be a useful experimental tool [98]. As in the scheme of Ruostekoski *et al.*, scattered photons can be collected using a system of two lenses as shown in Figure 3.3, where the number of photons detected gives a signal dependent on temperature. As noted by Ruostekoski *et al.*, the elastically scattered photons have no temperature dependence and placing a stop at the centre of the Fourier plane of the first lens will improve the signal to noise ratio, by blocking the central diffraction peak.

In Figure 3.4 we plot the temperature dependence of light scattering for a 30×30 two-dimensional lattice containing 2700 atoms. Figure 3.4(a) shows the total number of photons scattered per second over all angles, as well as the total number scattered inelastically and the number scattered by processes involving higher bands. The higher band scattering makes up about a third of the total inelastic scattering and has very small temperature dependence, changing by less than 0.1% for the temperature range plotted. In Figure 3.4(b) we plot the number of photons collected $N_c(T)$ per second by the lens system as a function of temperature T. We have assumed that the lens system has a numerical aperture of $\sin\theta = 0.5$ and the stop blocks light scattered with $\theta < 0.06$.

As discussed by Ruostekoski *et al.*, the inelastic scattering processes that are responsible for the temperature dependence of the scattering rate also heat the sample, and to measure the temperature without perturbing the system significantly we must limit the number of inelastic events W. Following Ruostekoski *et al.* we take $W = 0.1N$. To measure the temperature to a useful accuracy it is then necessary to do multiple repetitions τ of the experiment. The accuracy of the measurement then depends on the Poissonian fluctuations $\sqrt{\tau N_c(T)}$ of the number of photons collected in the τ repetitions. To achieve an uncertainty ΔT in the temperature measurement at temperature T we then require $\tau(N_c(T+\Delta T)-N_c(T)) \sim \sqrt{\tau N_c(T)}$ [40]. For the experimental parameters discussed above, determining the tempera-

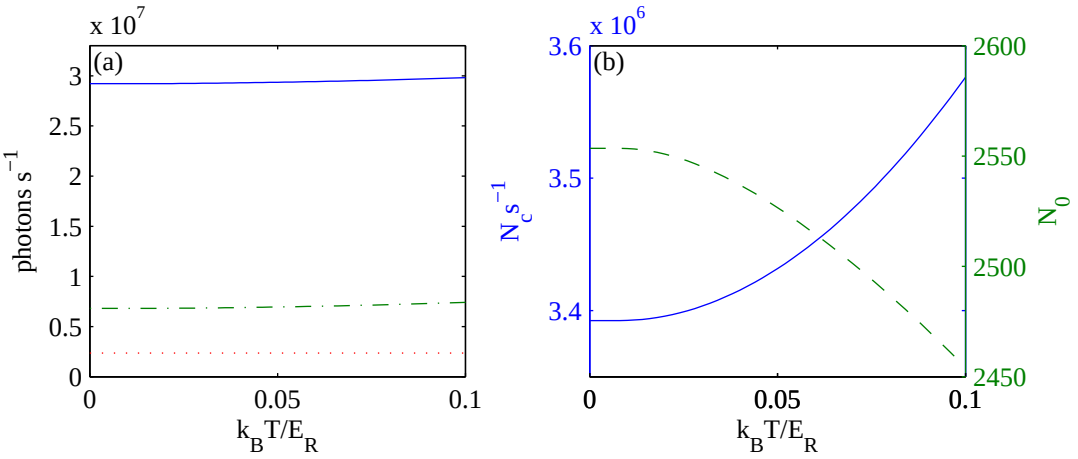

Figure 3.4: Temperature dependence of scattering from a superfluid state for a 30×30 lattices with $N = 2700$, The lattice has $V_0 = 3E_R$ in the x and y directions and $V_0 = 20E_R$ in the z direction, leading to parameters $J = 0.11E_R$ and $U = 0.17E_R$. The scattering rates are determined for the D_2-line of Rb^{87}, with a detuning from resonance of 20γ and laser intensity of $I_{in} = 5Wm^{-2}$. (a) Number of photons scattered per second over all angles for (solid) all photons, (dot-dashed) all inelastic photons and (dotted) photons scattered involving higher bands. (b)(left axis – solid) The number of photons per second collected by a lens with numerical aperture 0.5 and a 0.06 radians circular stop. (b)(right axis – dashed) Number of atoms in the zero momentum Bloch state.

ture to accuracy $0.005E_R/k_B$ would require 258 repetitions at $k_BT = 0.1E_R$ and 1005 repetitions at $k_BT = 0.05E_R$. The presence of the inelastic higher band scattering which is temperature independent reduces the efficiency of the measurement, where for comparison if these effects were excluded the number of repetitions required would be 175 and 661 respectively.

3.6 Perturbation of the Mott phase at zero temperature

We have seen that light scattering from an optical lattice in the superfluid regime is influenced by the correlations between atoms in the ground state and changes with temperature. We now examine light scattering from the Mott insulator. This state is characterised by strong interactions between atoms leading to particle localisation and one may expect that the characteristics of light scattered from this state will be significantly different. To examine this situation we apply perturbation theory in the Mott regime [99], an approach that has been applied to light scattering in a theoretical work investigating Bragg scattering by Rey *et al.* [80] and extended in Rist *et al.* [81]. In this section we will work at zero temperature and not consider the contribution from the upper bands, while we consider the effect of finite tunnelling on the Mott state. We will return to the effects of finite temperature and the full band structure in the next section.

In the absence of tunnelling ($J = 0$) for commensurate filling of the lattice, $N/M = n_0$ with n_0 an integer, the ground state is

$$|\Psi_0^{(0)}\rangle = \prod_j \frac{(\hat{b}_j^\dagger)^{n_0}}{\sqrt{n_0!}}|0\rangle, \tag{3.31}$$

a number state with exactly n_0 atoms at each lattice site. We can then use pertur-

bation theory to examine what happens to the ground state when a small amount of tunnelling is introduced. To first order in J/U the ground state is then

$$|\Psi_0\rangle = \left(1 - \frac{J^2}{2U^2} n_0(n_0+1)MZ\right)|\Psi_0^{(0)}\rangle + \frac{J}{U}\sum_{\langle j,l\rangle} \hat{b}_j^\dagger \hat{b}_l |\Psi_0^{(0)}\rangle, \tag{3.32}$$

where the prefactor of $|\Psi_0\rangle$ ensures normalisation to order $(J/U)^2$. The ground state is now the superposition of the uniformly filled unperturbed ground state and all states where an atom has tunnelled into a nearest neighbour site.

Expanding the atomic field operator in terms of the Wannier site basis gives the following expression for the dynamic structure factor

$$S(\Delta\mathbf{k}, \Delta\omega_\mathbf{k}) = \sum_{v,j_1,j_2,j_3,j_4} \langle\Psi_0|\hat{b}_{j_1}^\dagger \hat{b}_{j_2}|\Psi_v\rangle\langle\Psi_v|\hat{b}_{j_3}^\dagger \hat{b}_{j_4}|\Psi_0\rangle f^*_{j_2,\mathbf{0},j_1,\mathbf{0}}(\Delta\mathbf{k}) f_{j_4,\mathbf{0},j_3,\mathbf{0}}(\Delta\mathbf{k}) \times \delta((E_v - E_0)/\hbar - \Delta\omega_\mathbf{k}) \tag{3.33}$$

where $|\Psi_v\rangle$ are the eigenstates of the Bose-Hubbard Hamiltonian to first order in J/U with energy E_v and

$$f_{j_1,\mathbf{m},j_2,\mathbf{n}}(\Delta\mathbf{k}) = \int d\mathbf{r} w_\mathbf{m}(\mathbf{r} - \mathbf{r}_{j_1}) w_\mathbf{n}(\mathbf{r} - \mathbf{r}_{j_2}) e^{i\Delta\mathbf{k}\cdot(\mathbf{r})}. \tag{3.34}$$

The overlap between Wannier functions at different sites is very small in the Mott regime and $f_{j_1,\mathbf{0},j_2,\mathbf{0}}(\Delta\mathbf{k})$ can be neglected for $j_1 \neq j_2$. We then have

$$S(\Delta\mathbf{k}, \Delta\omega_\mathbf{k}) = |f_{0,\mathbf{0},0,\mathbf{0}}(\Delta\mathbf{k})|^2 \sum_{t,j,l} \langle\Psi_0|\hat{n}_l|\Psi_v\rangle\langle\Psi_v|\hat{n}_j|\Psi_0\rangle e^{i\mathbf{\Delta k}\cdot(\mathbf{r}_j - \mathbf{r}_l)} \times \delta((E_v - E_0)/\hbar - \Delta\omega_\mathbf{k}). \tag{3.35}$$

The matrix elements $\langle\Psi_v|\hat{n}_j|\Psi_0\rangle$ in the dynamic structure factor will only be non-zero when $|\Psi_v\rangle$ is the ground state or a particle-hole state, which have unper-

turbed form $|\Psi^{(0)}_{j,l}\rangle = \frac{1}{\sqrt{n_0(n_0+1)}}\hat{b}^\dagger_j\hat{b}_l|\Psi^{(0)}_0\rangle$ for $j \neq l$. These particle-hole states are degenerate in the unperturbed Hamiltonian, all having $E^{(0)}_{j,l} - E^{(0)}_0 = U$. To do first order perturbation theory we must first find a basis of states, $|\Phi^{(0)}_v\rangle = \sum_{j,l} C^v_{j,l}|\Psi_{j,l}\rangle$, for the particle-hole subspace that are diagonal within the subspace with respect to the operator $-J\sum_{\langle j,l\rangle}\hat{b}^\dagger_j\hat{b}_l$. This requires that

$$-E^{(1)}_v C^v_{j,l} = J(n_0+1)\sum_{\langle s,l\rangle} C^v_{s,l} + Jn_0\sum_{\langle j,s\rangle} C^v_{j,s} \quad \text{and} \quad C^v_{j,j} = 0, \tag{3.36}$$

where $E^{(1)}_v$ is the first order correction to the energy of $|\Phi_v\rangle$. For a translationally invariant system the $C^v_{j,l}$'s must also fulfill periodic boundary conditions that make the equations difficult to solve analytically. We proceed by solving these equations numerically to find the band of excited particle-hole states.

In terms of these states the dynamic structure factor becomes

$$\begin{aligned} S(\Delta\mathbf{k},\Delta\omega_\mathbf{k}) = |f_{0,\mathbf{0},0,\mathbf{0}}(\Delta\mathbf{k})|^2 \left[n_0^2\mathcal{F}(\Delta\mathbf{k})\delta(\Delta\omega_\mathbf{k}) \right. \\ \left. + \sum_v \left| \frac{J}{U}\sum_{\langle j,l\rangle}\langle\Phi^{(0)}_v|\hat{b}^\dagger_j\hat{b}_l|\Psi^{(0)}_0\rangle(e^{i\mathbf{q}\cdot\mathbf{r}_j} - e^{i\mathbf{q}\cdot\mathbf{r}_l}) \right|^2 \delta((U+E^{(1)}_v)/\hbar - \Delta\omega_\mathbf{k}) \right], \end{aligned} \tag{3.37}$$

where

$$\mathcal{F}(\Delta\mathbf{k}) = \sum_{j,l} e^{i\Delta\mathbf{k}\cdot(\mathbf{r}_j-\mathbf{r}_l)} = \prod_{j\in\{x,y,z\}} \frac{\sin^2(M_j\Delta\mathbf{k}_j a/2)}{\sin^2(\Delta\mathbf{k}_j a/2)} \tag{3.38}$$

is the classical diffraction pattern from an $M_x \times M_y \times M_z$ array of apertures with inter-site separation a in each dimension.

We plot the dynamic structure factor in Figure 3.5 for energy change $\hbar\Delta\omega_\mathbf{k}$ near U using a numerical solution of Equation (3.36) for an 8×8 two dimensional lattice. The light scattering at frequencies near $U/\hbar$ is distributed over a band of energies that scales with the size of J. The intensity of this light depends on $(J/U)^2$ and is many orders of magnitude smaller than that due to classical diffraction.

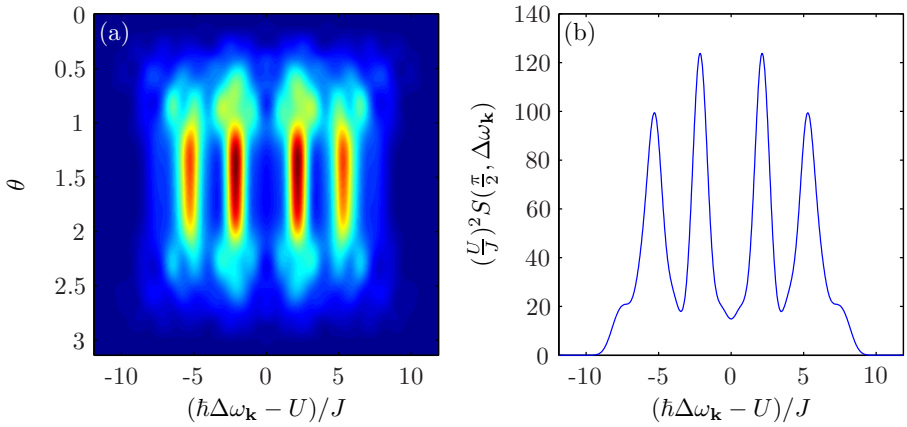

Figure 3.5: Dynamic structure factor in the Mott insulator regime for an 8×8 lattice with $V_0 = 20E_R$ and $n_0 = 1$. (a) Angular dependence for $\phi = 0$ of the components with $\hbar\Delta\omega_{\mathbf{k}} \sim U$. (b) A slice through the function in (a) at $\theta = \pi/2$. The frequency distribution is plotted assuming a measurement time scale of 70 ms.

3.7 Angular distribution of light scattering from the Mott insulator

We now look at the angular distribution of light scattering from the Mott insulator and adapt our approach to allow for scattering to higher bands and scattering at finite temperature. Again we will assume that the temperature is low enough that all the atoms initially reside within the lowest band of the lattice. Including all bands, the static structure factor is given by the expression

$$S(\Delta\mathbf{k}) = \sum_{j_1,j_2,j_3,j_4,\mathbf{m}} \langle \hat{b}^\dagger_{j_1,\mathbf{0}} \hat{b}_{j_2,\mathbf{m}} \hat{b}^\dagger_{j_3,\mathbf{m}} \hat{b}_{j_4,\mathbf{0}} \rangle f^*_{j_1,\mathbf{0},j_2,\mathbf{m}}(\Delta\mathbf{k}) f_{j_4,\mathbf{0},j_3,\mathbf{m}}(\Delta\mathbf{k}). \tag{3.39}$$

As in the superfluid case, we can simplify the part involving scattering to higher bands using the sum rule, this time for the Wannier functions, to get

$$S_b(\Delta\mathbf{k}) = N - \sum_{j_1,j_2,j_4} \langle \hat{b}^\dagger_{j_1,\mathbf{0}} \hat{b}_{j_4,\mathbf{0}} \rangle f^*_{j_1,\mathbf{0},j_2,\mathbf{0}}(\Delta\mathbf{k}) f_{j_4,\mathbf{0},j_2,\mathbf{0}}(\Delta\mathbf{k}). \tag{3.40}$$

The description now only involves contributions from the lowest band and we can drop the band index from our notation. Neglecting the overlap between Wannier functions at different lattice sites, the contribution to light scattering from the lowest band is

$$S_g(\Delta\mathbf{k}) = |f_{0,0}(\Delta\mathbf{k})|^2 \sum_{j,l} \langle \hat{n}_j \hat{n}_l \rangle e^{i\Delta\mathbf{k}\cdot(\mathbf{r}_j - \mathbf{r}_l)} \tag{3.41}$$

and the contribution from scattering involving the upper bands is

$$S_b(\Delta\mathbf{k}) = N(1 - |f_{0,0}(\Delta\mathbf{k})|^2). \tag{3.42}$$

Here we see that when the site overlap is negligible, the contribution from the upper bands is dependent only on the shape of the site Wannier function and provides no other information about the atoms in the lattice.

Deep in the Mott insulator regime the angular dependence of light scattering could be calculated using the perturbation theory of the previous section. However, as we have seen, perturbing J from zero leads to corrections to the unperturbed scattering pattern of order $M(J/U)^2$ and corrections to the unperturbed energies of order J [80]. When $J \ll U$ these perturbations have negligible effects on the scattering pattern and the scattering pattern is well approximated by that produced when $J = 0$. We therefore proceed to calculate the scattering at finite temperature by assuming $J = 0$.

To evaluate Equation (3.41) in the Mott regime at temperature T we need to calculate $\sum_u \langle \psi_u | \hat{n}_j \hat{n}_l | \psi_u \rangle e^{-E_u/k_B T}/Z$ where $|\psi_u\rangle$ are the eigenstates of the Bose-Hubbard Hamiltonian with energy E_u, and $Z = \sum_u e^{-E_u/k_B T}$ is the canonical partition function of the system. Making the approximation $J = 0$ [100], the eigenstates are simply number states $|\{n\}_u\rangle \equiv |\{n_j^{(u)}, j = 1, \ldots, M\}\rangle$ with energies $\sum_j U n_j^{(u)}(n_j^{(u)} - 1)/2$, where the total number of atoms, $\sum_j n_j^{(u)} = M n_0$, is fixed.

For a translationally invariant system, the energy of these number state remains

the same under any permutation of lattice sites. The eigenstates are then divided into degenerate groups labelled by v, where $|\{n\}_v\rangle$ is a representative eigenstate. The other members of the group are got by permutations P of the lattice sites, resulting in g_v different states $|P\{n\}_v\rangle$ each with energy E_v. We can use this symmetry to evaluate the required matrix elements of Equation (3.41). For each v we have

$$\sum_P \langle P\{n\}_v|\hat{n}_j\hat{n}_l|P\{n\}_v\rangle = \begin{cases} g_v\langle n^2\rangle_v & \text{for } j=l \\ \dfrac{g_v(N^2 - M\langle n^2\rangle_v)}{M(M-1)} & \text{for } j\neq l, \end{cases} \tag{3.43}$$

where $\langle n^2\rangle_v = \frac{1}{M}\sum_j \left(n_j^{(v)}\right)^2$ is the average over of the degenerate group v. This then gives

$$\sum_{j,l}\sum_P \langle P\{n\}_v|\hat{n}_j\hat{n}_l|P\{n\}_v\rangle e^{i\Delta\mathbf{k}\cdot(\mathbf{r}_j-\mathbf{r}_l)} = g_v\left[n_0^2\sum_{j,l} e^{i\Delta\mathbf{k}\cdot(\mathbf{r}_j-\mathbf{r}_l)} + \frac{\langle n^2\rangle_v - n_0^2}{(M-1)}\left(M^2 - \sum_{j,l} e^{i\Delta\mathbf{k}\cdot(\mathbf{r}_j-\mathbf{r}_l)}\right)\right]. \tag{3.44}$$

Finally we find that the lowest band contribution to the light scatter results in two terms. The first is the classical pattern due to the average density

$$S_{g0}(\Delta\mathbf{k}) = |f_{0,0}(\Delta\mathbf{k})|^2 n_0^2 \mathcal{F}(\Delta\mathbf{k}), \tag{3.45}$$

and the second term is due to the number fluctuations on each site at finite temperature

$$S_{g1}(\Delta\mathbf{k}) = |f_{0,0}(\Delta\mathbf{k})|^2 \sum_v \frac{g_v e^{-E_v/k_BT}(\langle n^2\rangle_v - n_0^2)}{(M-1)Z}\left(M^2 - \mathcal{F}(\Delta\mathbf{k})\right). \tag{3.46}$$

For a number of sites of around 50 this formalism allows us to calculate the

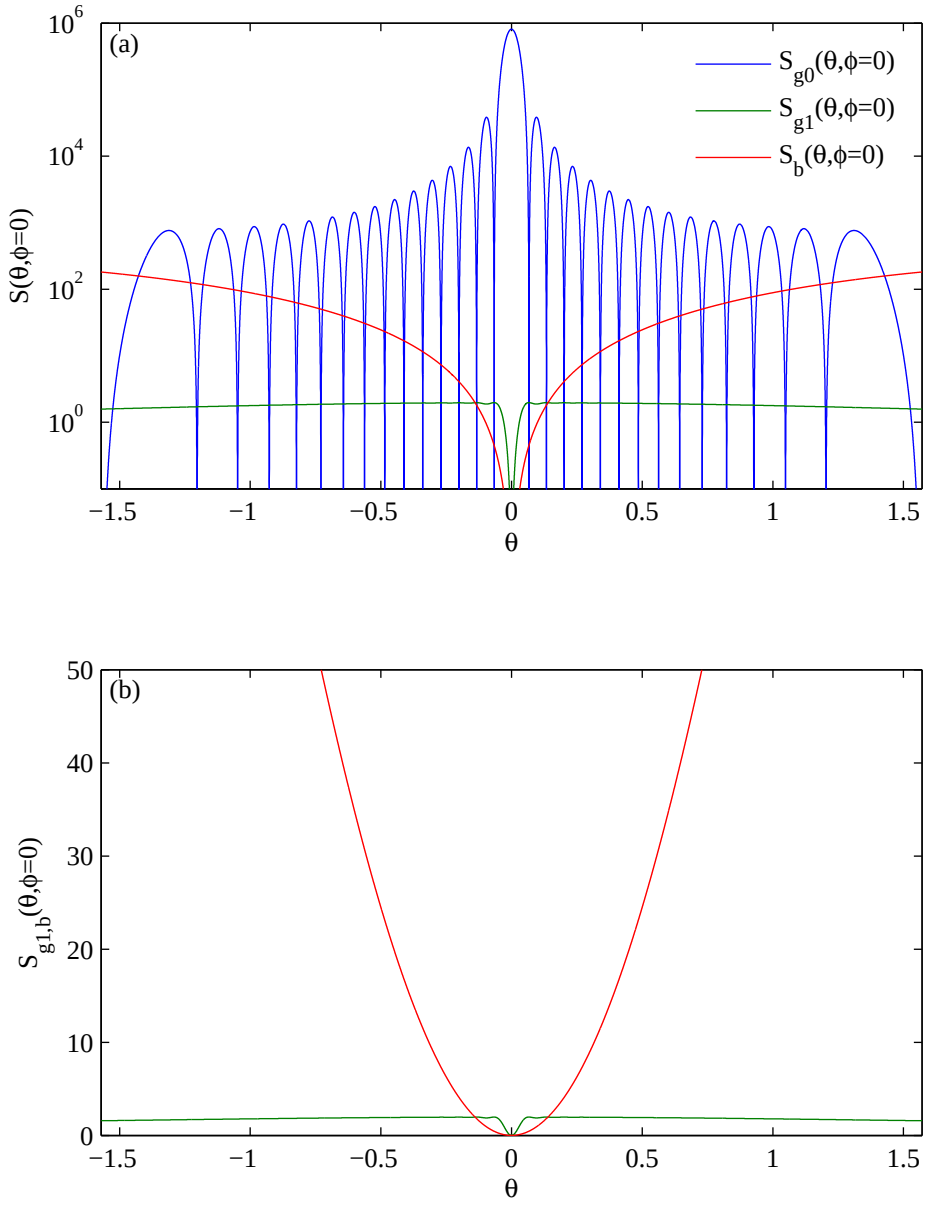

Figure 3.6: Angular dependence of components of the static structure factor in the Mott insulator regime for a 30×30 lattice with $n_0 = 1$ and $V_0 = 25E_R$ in all directions. The temperature is $0.05E_R/k_B$ ($U = 0.66E_R$) at which point the ground state proportion is 0.3. (a) Components of the structure factor on a log scale for $\phi = 0$. (b) Inelastic components only.

light scattering resulting from all possible excitations. We soon see however, that in the temperature range where the ground state, $|\{n_j = n_0, j = 1, \ldots, M\}\rangle$, is still significantly populated, the only states that play a significant role determining the scattering distribution are the states involving particle-hole excitations. These are the states that have $n_0 + 1$ atoms at the sites $p_1, p_2, \ldots, p_v$ and an equal number of sites $h_1, h_2, \ldots, h_v$ with $n_0 - 1$ atoms. There are $g_v = M!/(M-2v)!(v!)^2$ states with v particle-hole pairs and these have energy $E_v = vU$ and site number fluctuations of $(\langle n^2 \rangle_v - n_0^2) = 2v/M$. Restricting our calculations to just these states allows for calculations involving much larger lattices.

In the limit $T = 0$ the light scattering is purely due to the classical diffraction pattern and higher band scatter, no excitation of the lattice occurs within the lowest band, a major difference from the superfluid phase. We can see why this is by considering the simple two site case. Switching from the site basis to the lattice momentum basis using $\hat{b}_{\mathbf{q}} = \frac{1}{\sqrt{N_s}} \sum_j \hat{b}_j e^{i\mathbf{q}\cdot\mathbf{r}_j}$, we see that the Mott state with filling factor one is $\hat{b}_1^\dagger \hat{b}_2^\dagger |0\rangle = 1/2((\hat{b}_{\mathbf{0}}^\dagger)^2 - (\hat{b}_{\mathbf{q}}^\dagger)^2)|0\rangle$, where $\mathbf{q} = \frac{\pi}{a}(\mathbf{r}_2 - \mathbf{r}_1)$. Light scattering involving wave vector change $\Delta\mathbf{k} = \mathbf{q}$ occurs by two routes $\hat{b}_{\mathbf{q}}^\dagger \hat{b}_{\mathbf{0}}$ and $\hat{b}_{\mathbf{0}}^\dagger \hat{b}_{\mathbf{q}}$. Each of these routes takes the Mott state to the same state, but with opposite signs, and the amplitudes cancel. The lack of excitations is then explained as due to interference caused by correlations in the lattice momentum distribution.

In Figure 3.6 we plot the components of the static structure factor for a Mott insulator at finite temperature. The classical diffraction pattern remains the central feature and does not change with temperature, as in the superfluid case. However, the inelastic scattering is significantly different from the superfluid case with the scattering involving higher bands dominant over the other inelastic scattering processes, which disappear as $T \to 0$. In Figure 3.7(a) we plot the ratio of inelastic scattering in the lowest band to the temperature independent higher band scattering. In this case the ratio does not get above 0.05 while the zero temperature

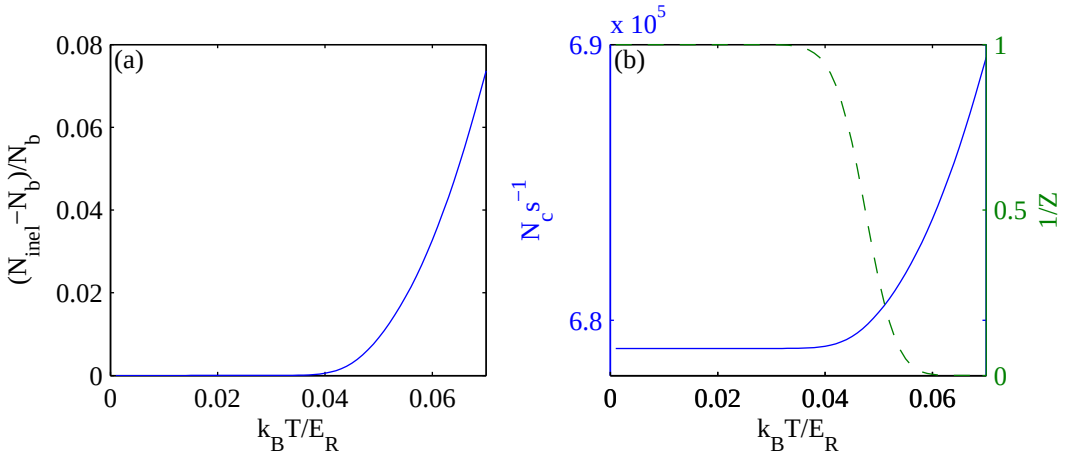

Figure 3.7: Temperature dependence of scattering from a Mott insulator state for a 30×30 lattice with $n_0 = 1$ and $V_0 = 25E_R$ in all directions. The scattering rates are determined for the D_2-line of Rb^{87}, with a detuning from resonance of 20γ and laser intensity $I_{in} = 10Wm^{-2}$. (a) Ratio of the number of photons scattered by lowest band inelastic scattering $N_{inel} - N_b$ to the number scattered by higher band inelastic scattering N_b. (b)(left axis – solid) The number of photons per second collected by a lens with numerical aperture 0.5 and a 0.06 radians circular stop. (b)(right axis – dashed) Proportion of state in zero temperature ground state.

ground state is still significantly populated.

In Figure 3.7(b) we plot the number of photons collected by the lens system suggested by Ruostekoski *et al.* and discussed in Section 3.5. The temperature independent band scattering greatly reduces the efficiency of temperature measurement, where a temperature measurement at $T = 0.05E_R/k_B$ would take over 6500 repetitions to achieve an accuracy of 10%. In contrast without the band contribution this would have only required 60 repetitions.

3.8 Conclusions

In this chapter we have shown how the correlations in the Mott and superfluid states are reflected in the way these states scatter light. We have extended previous treatments of light scattering, where the most significant extension has been the inclusion of the higher band structure in the scattering process. Using our

treatment of higher band scattering we have demonstrated that this reduces the efficiency of temperature measurements using light scattering, particularly in the Mott insulator case. In future work this treatment could also be applied to the case for fermions in optical lattices to test whether the temperature measurement suggested by Ruostekoski *et al.* also has reduced efficiency when the higher bands are included.

Chapter 4

Light scattering from small optical lattices

In the previous chapter we formed a description of the light scattered from the superfluid and Mott insulator regimes by using approximate methods that applied in the extremes $U \to 0$ and $J \to 0$. In this chapter we examine the regime of small lattices where the eigenstates of the Bose-Hubbard Hamiltonian can be found directly by numerical diagonalisation. We do this in the first place to provide a test of the methods we used in the previous chapter and to provide information about what happens in between the two extremes, which we will look at in the first part of this chapter.

Small lattices are also potentially important in their own right, particularly given that we are interested in creating entanglement between incoming light and the atoms in the optical lattice. Scattering individual photons off a lattice containing only a few atoms leads to a significant change of the atomic system, whereas for a system with a large number of atoms this only causes a small perturbation. With small lattices we are then able to see strong conditionality between consec-

utive scattering events, which we investigate in the second part of this chapter. We see this as a starting point for future work investigating light scattering and entanglement in arrays of small lattice systems.

In this chapter we numerically diagonalise the Bose-Hubbard Hamiltonian for an atomic system with fixed particle number N. The Hilbert space in this case is spanned by $(M+N-1)!/[(M-1)!N!]$ basis vectors, for a lattice with M sites. The size of the basis grows rapidly with N and M; in the limit $N = M \gg 1$, increasing both M and N by one increases the basis size by a factor of four. This means that numerical diagonalisation rapidly becomes intractable using current computer technology. Nevertheless, for lattice sizes such that $N, M \leq 12$ we can find numerical solutions for the ground state and a number of excited states of the Bose-Hubbard Hamiltonian.

4.1 Comparison with approximate methods

The numerical exact solution of the Bose-Hubbard model allows us to examine how well the perturbative treatments used in the previous chapter predict the distribution of light scattering. In Figure 4.1(a) we compare the scattering distributions calculated using the numerical diagonalisation and the Bogoliubov method for a one-dimensional lattice with $N = M = 9$ at finite temperature. We see good agreement between the scattering patterns produced. In Figure 4.1(b) we compare the distributions after subtracting the parts resulting from classical diffraction and the higher bands. We see that the Bogoliubov treatment has an erroneous contribution at $\Delta k_x = 0$. This is because the Bogoliubov treatment used is not number conserving and leads to fluctuations in the total number of atoms. We expect a number conserving treatment [87, 88, 89, 90, 9] would lead to better agreement here. The difference at $\Delta k_x = 0$ does not affect the predictions made about the

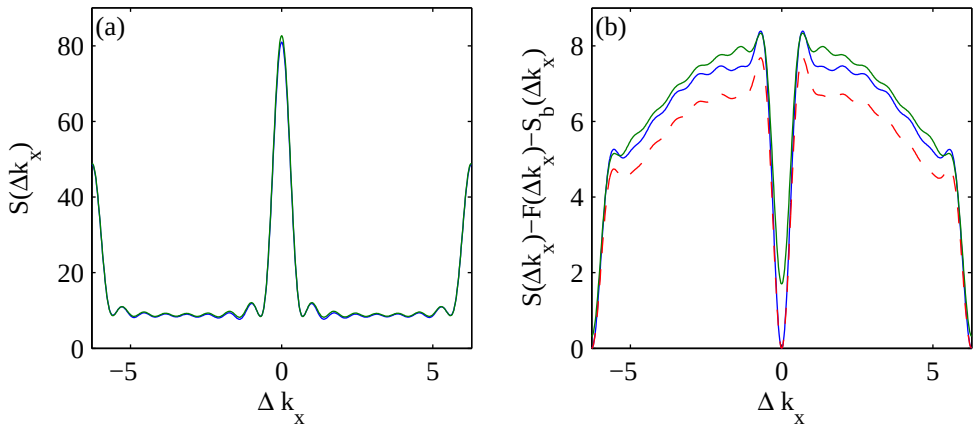

Figure 4.1: Comparison of structure factors calculated for a one-dimensional lattice with $N = M = 9$ using (blue) the numerical solution of the Bose-Hubbard model and (green) the Bogoliubov treatment. (a) Full structure factor. (b) Structure factor minus the classical diffraction pattern $\mathcal{F}(\Delta k_x)$ and the contribution from higher bands. For the Bogoliubov theory the remaining components are the first and second order contributions shown by the green line. The red dashed line shows just the first order term. Parameters used are $T = 0.0035 E_R/k_B$, $U/J = 0.48$, $V_0 = 15$ and the Bogoliubov treatment gives a condensate population of 8.1 atoms.

temperature measurement in Section 3.5, as this contribution is removed by the stop. Note that in Figure 4.1 V_0 is artificially high to remove differences in the comparison resulting from the use of the Bose-Hubbard Hamiltonian, which makes the tight binding approximation, for the exact diagonalisation and the use of the full Bloch description in the Bogoliubov treatment. The system is kept within the Bogoliubov regime by making the scattering length artificially low.

In Figure 4.2(a) we compare the structure factors in the Mott regime calculated using the numerical diagonalisation and the perturbative Mott treatment from Section 3.7. Figure 4.2(b) shows the contribution due only to the finite temperature excitations above the zero temperature ground state. We see good agreement, suggesting our method of calculating the temperature dependence of the light scattering in the previous chapter will produce results with good accuracy.

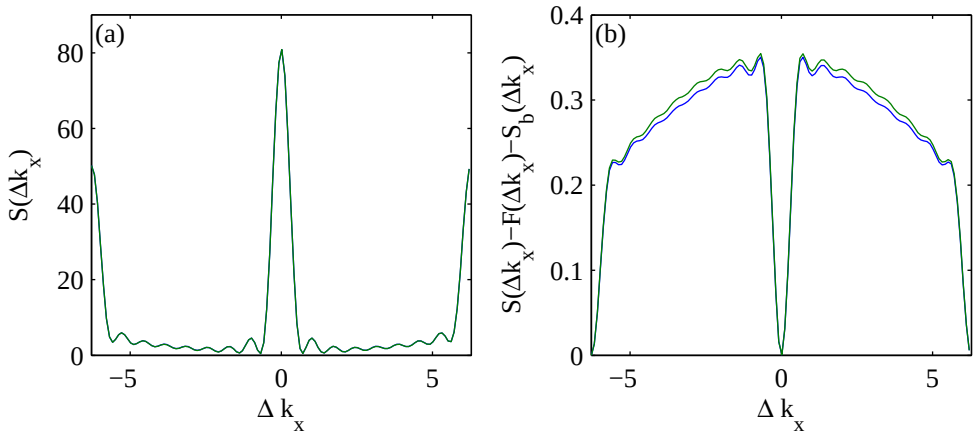

Figure 4.2: Comparison of the structure factors for a one-dimensional lattice with $N = M = 9$ in the Mott regime calculated using (blue) the numerical solution and (green) the perturbative Mott treatment. (a) Full structure factor. (b) Contribution due to finite temperature excitations only. Parameters used are $T = 0.037 E_R/k_B$, $U/J = 51$, $V_0 = 17$ and the proportion of the atoms in the zero temperature ground state is 0.84.

4.2 Angular distribution of light scattering

Using the numerical solution of the Bose-Hubbard model, we can now examine light scattering behaviour over a full range of U/J values, from the superfluid regime near $U/J = 0$, to the Mott regime where $U/J \gg 1$. In Figure 4.3 we plot the scattering distributions for two different experimental methods of changing the ratio of U/J. The first, in the top row of the figure, shows how the distribution changes as we vary the s-wave scattering length. This results in U/J changing while the site Wannier function of the lattice remains constant and can be achieved by Feshbach resonance [13]. The second method involves changing the lattice height V_0, which leads to a simultaneous change of U/J and the width of Wannier function. The change in the angular distribution for this scenario is shown in the second row of the figure, where, compared to the previous scenario, we see a narrowing of the distribution for low V_0 when the Wannier function is widest. In both cases we see a smooth transition between the patterns in the superfluid and Mott regimes, with

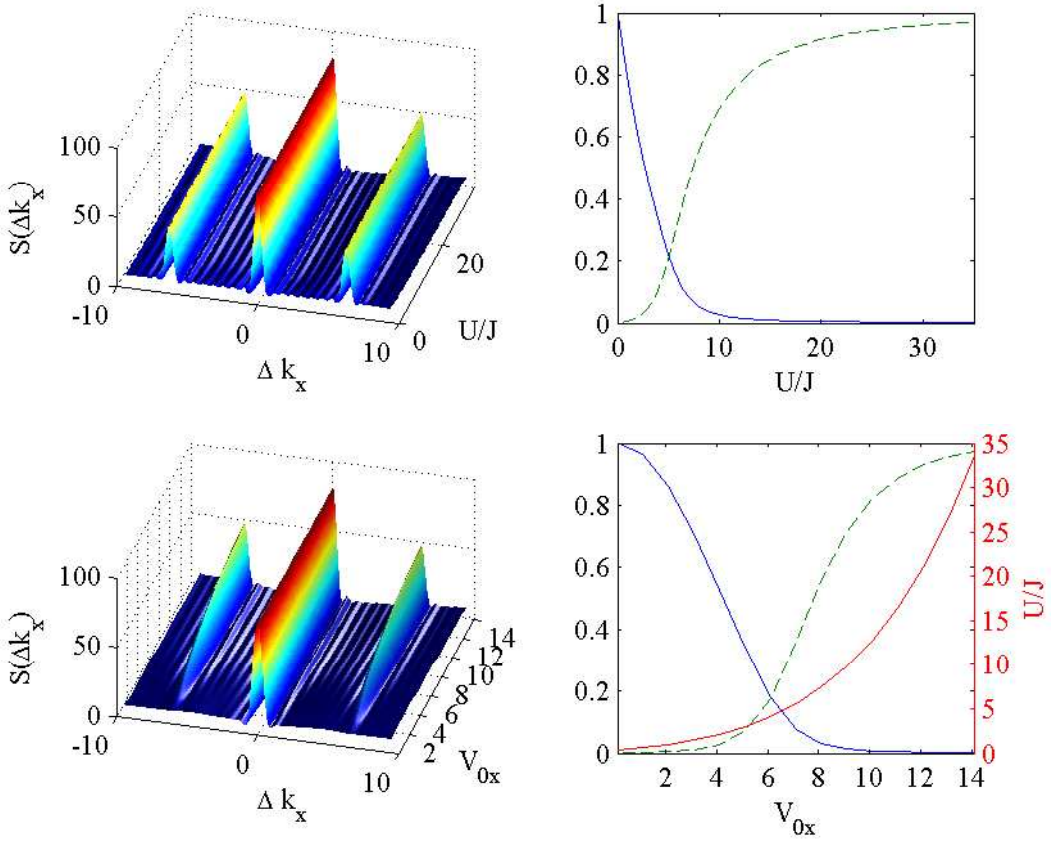

Figure 4.3: Angular dependence of scattering for a one-dimensional lattice with $N = M = 9$ at $T = 0$ as (top) U/J is varied while keeping $V_0 = 15$ constant and (bottom) while V_0 is adjusted. On the right we show the overlap of the ground state with (blue) the $U = 0$ superfluid state and (green) the $U \to \infty$ Mott state. In the bottom right plot we also show the value of U/J for comparison purposes.

no new features appearing in between.

4.3 Dynamic light scattering

Up until now, our theory has assumed that the light scattering pattern can be calculated using the static structure factor for a particular state. The underlying assumption has been that, following each light scattering event, the state of the atoms remains essentially unchanged and the next scattering event will occur with the same distribution. This approximation is valid if the number of atoms is so large that light scattering only perturbs the state slightly, or the scattering experiment is repeated a number of times for the same initial state and only a few photons are scattered in each realisation. For a small lattice, the change to the many-body state caused by each light scattering event will be significant, and we cannot expect the static structure factor to produce an accurate description if more than a few photons are scattered.

Here we investigate the effect of consecutive photon scattering events on the many-body state in a small lattice. To do so we extend the method used by Rau *et al.* to study the localisation of two particles in free space as a result of light scattering [101]. Rau *et al.* showed that, for a two particle system, scattering a photon followed by detection of the photon in the far field resulted in relative localisation of the two particles' coordinates. Consecutive scattering events then led to the particles becoming increasingly well localised over time. This can be understood as each scattering and detection event revealing information about the relative position of the two particles and the series of scatterings and detections pushing the state towards an eigenstate of the light scattering measurement. We will see that a similar process occurs for atoms in an optical lattice.

To make the treatment of dynamic scattering tractable for optical lattices we

neglect scattering out of the lowest band and also the overlap of neighbouring Wannier functions. The effect of the latter approximation on the scattering distributions is small for $V_0 > 5$ and decreases as V_0 increases. Neglecting the band structure becomes a more accurate approximation as either V_0 increases or as the wave vector of the light becomes small compared with the wave vector of the optical lattice. This becomes a very good approximation in the case of matter wave scattering [102], where energy conservation restricts the atoms from receiving enough energy to get out of the lowest band. We also restrict the system to a one dimensional lattice in the x-direction and only consider photon scattering within the xz-plane, where the initial light propagates along the z-axis.

4.3.1 Effect of scattering on the many-body state

We proceed by examining the effect on the many-body state of scattering events where the photons are detected in the far field. The scattering and detection events are assumed to have a definite time ordering, so that the mth event results in a new state of the atomic system $|\Psi_m\rangle$. Working again with the number state basis, $|\{n\}_u\rangle \equiv |\{n_j^{(u)}, j = 1, \ldots, M\}\rangle$, where $n_j^{(u)}$ is the number of atoms at site j and u uniquely identifies each basis state, the system state can be expanded as $|\Psi_m\rangle = \sum_u c_u^{(m)} |\{n\}_u\rangle$. First order scattering of a photon from this state leads to the new state

$$\sum_u c_u^{(m)} |\{n\}_u\rangle \frac{g}{N\sqrt{2\pi}} \int_{-\pi}^{\pi} d\theta I(\theta) \sum_j e^{-i\mathbf{r}_j \cdot \Delta\mathbf{k}(\theta)} n_j^{(u)} |\theta\rangle, \tag{4.1}$$

where $I(\theta) = \int d\mathbf{r} e^{i\Delta\mathbf{k}(\theta)\cdot\mathbf{r}} |w(r)|^2$, $\Delta\mathbf{k}(\theta) = k_0(-\sin\theta, 0, 1 - \cos\theta)$ and $|\theta\rangle$ is the plane wave state that would result in a photon being detected at an angle θ from the z-axis in the far field. Detection of a photon at angle θ then occurs according

to the probability density

$$P_m(\theta) = \frac{g^2}{2\pi N^2} \sum_u \left| I(\theta) c_u^{(m)} \sum_j e^{-i\mathbf{r}_j \cdot \Delta\mathbf{k}(\theta)} n_j^{(u)} \right|^2 . \tag{4.2}$$

Following a detection at θ the many-body state is projected into the new state

$$|\Psi_{m+1}\rangle = \frac{1}{\sqrt{\mathcal{N}}} \sum_u c_u^{(m)} \sum_j e^{-i\mathbf{r}_j \cdot \Delta\mathbf{k}(\theta)} n_j^{(u)} |\{n\}_u\rangle, \tag{4.3}$$

where $\mathcal{N}$ normalises the state.

This suggests an iterative process where we calculate the scattering distribution for a state, then choose a random detection event according to that distribution and find a new state using Equation (4.3). These steps are then repeated to simulate the effect of multiple scattering and detection events on the many-body state. The effect of this process can be seen by examining the projection in Equation (4.3). We note that the number basis states are eigenstates of the projection, and the scattering process will preserve any state that begins in a basis state. Moreover, some of the basis states produce the same scattering pattern, for example in the $N = M = 3$ case, $|201\rangle$ and $|102\rangle$ result in the same light scattering. Superposition of these states are partially preserved by the projection, in that the weight of each state in the superposition remains the same after scattering but the phase relationship is changed. For initial states that are the superposition of all the basis states, the projection gives higher weight to the basis states where $n_s = N$, for some lattice site s, and all other sites have zero occupancy. A sequence of scattering events with $\theta \neq 0$ then leads to a superposition of these states in the limit $m \to \infty$. This is because these states have the most uniform scattering distribution and scattering at any nonzero angle makes it more probable that the atomic system is in one of these states.

The story does not end here however, as noted by Rau *et al.* events where

photons are not scattered also reveal information about the many-body state and must be taken into account [101]. Following Rau *et al.* we introduce an unscattered term so that the state after the interaction becomes

$$\sum_u c_u^{(m)} |\{n\}_u\rangle \left(A_u|0\rangle + \frac{g}{N\sqrt{2\pi}} \int_{-\pi}^{\pi} d\theta I(\theta) \sum_j e^{-ir_j k_0 \sin(\theta)} n_j^{(u)} |\theta\rangle \right), \tag{4.4}$$

where we have introduced the unknown variable A_u as the coefficient of the unscattered state $|0\rangle$. To find A_u we note the total number of photons going into the system must equal the number coming out, that is, the probabilities of non-scattering and scattering must sum to one, or equivalently the state in Equation 4.4 must be normalised. This implies that

$$A_u = \sqrt{1 - \frac{g^2}{2\pi N^2} \int_{-\pi}^{\pi} d\theta \left| I(\theta) \sum_j e^{-ir_j k_0 \sin(\theta)} n_j^{(u)} \right|^2}, \tag{4.5}$$

where we have neglected the cross term between the non-scattered part and scattered part at $\theta = 0$. The cross term is proportional to the angular width of the unscattered state and can be made arbitrarily small by increasing the distance to the detector. The probability of a non-scattering event occurring for many-body state $|\Psi_m\rangle$ is then

$$P_m^{NS} = \sum_u |c_u^{(m)} A_u|^2. \tag{4.6}$$

Detecting a non-scattering event projects the state into the new state

$$|\Psi_{m+1}\rangle = \frac{1}{\sqrt{\mathcal{N}'}} \sum_u c_u^{(m)} A_u |\{n\}_u\rangle. \tag{4.7}$$

This projection favours basis states that produce less uniform scattering patterns and hence works in the opposite direction to the projection following a scattering event. As we will see this prevents the system from always ending in states with

all the atoms on one site.

The dynamic scattering process can now be simulated by the following procedure. Taking the initial state, we calculate the probability of non-scattering using Equation (4.6). A pseudo-random number is then generated to determine if non-scattering occurs. If it does then the projection in Equation (4.7) is applied. If instead scattering occurs then the random number is used to determine the angle of scattering according to the probability density in Equation (4.2). The state is then projected using Equation (4.3). In either case the many-body state is then normalised and becomes the input state and the process repeats.

4.3.2 Dynamic scattering from a 1d lattice

To examine the dynamic process we look at the simple case of a three site lattice containing three atoms. In this case there are only ten basis states making it straightforward to track the development of the many-body state. In Figure 4.4 we show one realisation of the dynamic scattering process for the three site lattice in the superfluid regime. For this example we have set the coupling constant $g = 0.1$ and as a result the vast majority of detection events result from non-scattering, however it only takes a few scattering events for the system to start favouring a particular final state. In this example the many-body state progresses toward a superposition of the states $|201\rangle$ and $|102\rangle$, two states which produce the same scattering pattern. As discussed above, continued scattering from this end superposition does not change the constituent basis vectors but does change the phase of the superposition. In Figure 4.4(c) we see that detection of a photon at non-zero angle quickly reduces the overlap of the many-body state with the original ground state. We see that the overlap makes quantum jumps when a scattering event occurs and gradually evolves due to non-scattering events.

By repeated simulation of the dynamic scattering process, we find that the

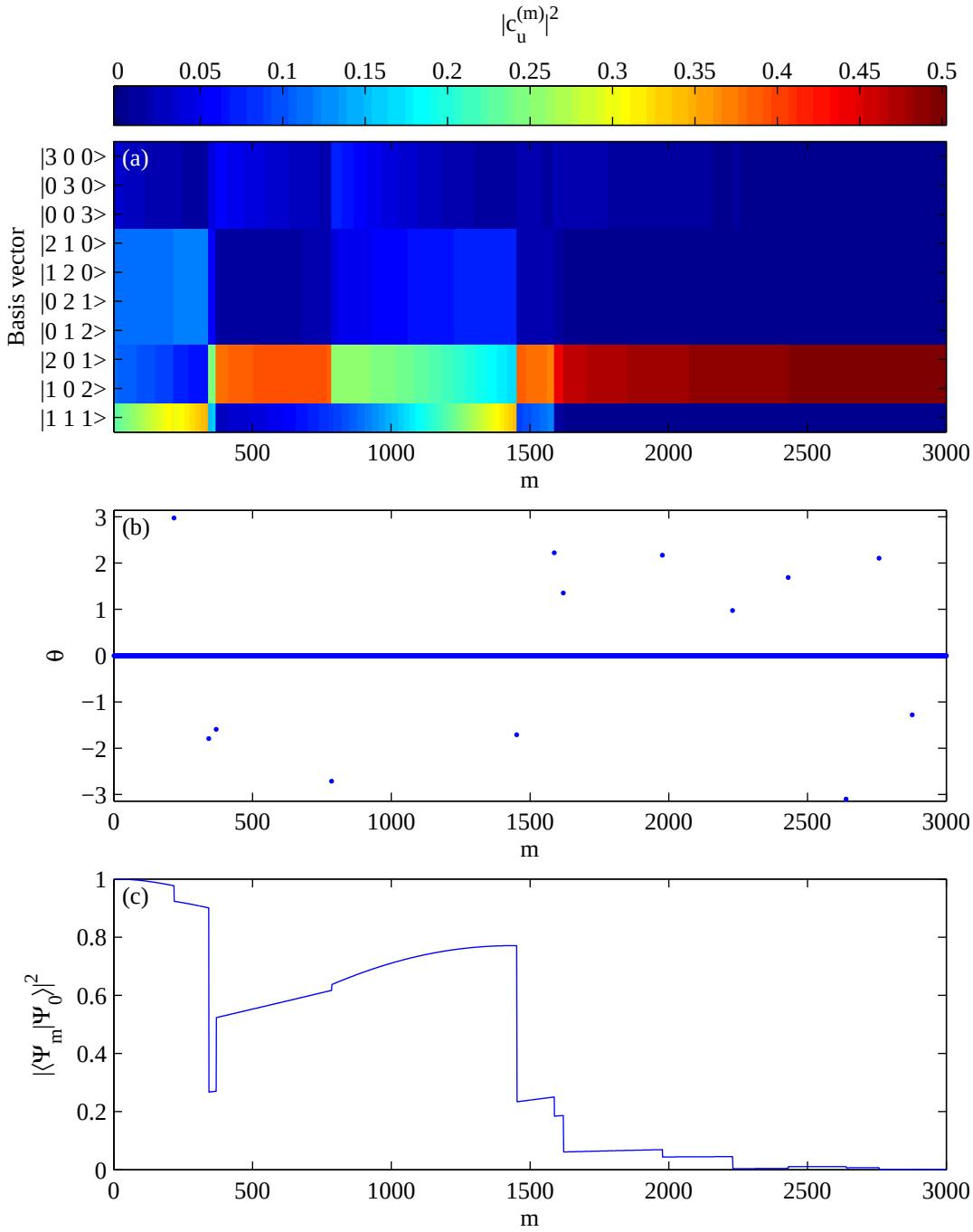

Figure 4.4: Development of an atomic state caused by 3000 scattering events for a lattice with $M = N = 3$. (a) Modulus squared of the basis coefficients of the state $|\Psi_m\rangle$. (b) Detected events. (c) Overlap of the many-body state with the initial ground state $|\Psi_0\rangle$. Parameters used are $U/J = 0.05$, $g = 0.1$ and $k_0 = \pi/a$.

simulations all settle into an end state after a number of scattering events. The end states are always superpositions of eigenstates of the scattering projection that produce the same scattering pattern. For the $N = M = 3$ cases there are four types of end state: (1) superpositions of $|300\rangle$, $|030\rangle$, and $|003\rangle$, (2) superpositions of $|210\rangle$, $|120\rangle$, $|012\rangle$ and $|021\rangle$, (3) superpositions of $|201\rangle$, and $|102\rangle$, and (4) $|111\rangle$.

In the Mott insulator regime the initial ground state is dominated by the $|111\rangle$ basis state and the most likely outcome of the dynamic process is to drive the state completely into the $|111\rangle$ state. In other words light scattering preserves the Mott state. In fact we find that the probability the end state of the dynamical scattering process is $|111\rangle$ is equal to $|\langle 111|\Psi_0\rangle|^2$, where $|\Psi_0\rangle$ is the initial state. This generalises for final states that are superpositions, for example the end state superposition of basis states $|201\rangle$ and $|102\rangle$ occurs with probability $|\langle 201|\Psi_0\rangle|^2 + |\langle 102|\Psi_0\rangle|^2$. In Figure 4.5(a) we plot the proportion with which each possible final state superposition is represented in an ensemble of 10000 simulations for various values of U/J. We see that the proportions match the initial probabilities of finding the relevant basis states in the initial ground state. The Mott state almost always ends in the $|111\rangle$ state, while for the superfluid, the end states are distributed across all possible outcomes. These results are independent of the coupling parameter g, which only affects the rate at which the state approaches an end state.

Because the final state proportions are the same as the initial basis state probabilities, we expect that the photon intensity distribution will equal that given by the initial ground state structure factor *if* we average over an ensemble of scattering experiments. This occurs even though the initial state can be completely changed in the scattering process. In Figure 4.5(b) we show the photon intensity distributions for two systems, one in the superfluid regime and the other in the Mott regime, for an ensemble of 10000 scattering simulations with 1000 detection events each. The photon intensity distributions for each ensemble match the struc-

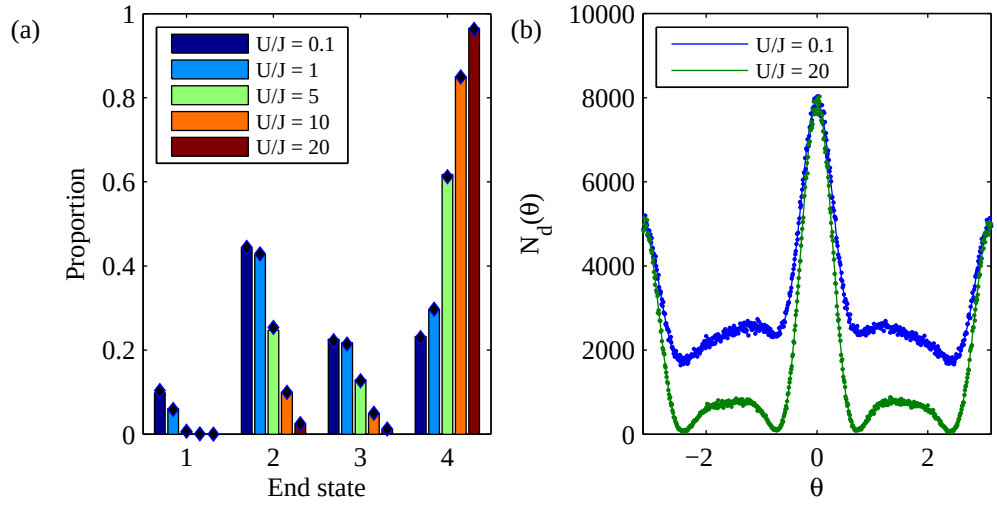

Figure 4.5: (a) Proportion of 10000 simulations that end in a final state superposition of (1) $|300\rangle$, $|030\rangle$, and $|003\rangle$, (2) $|210\rangle$, $|120\rangle$, $|012\rangle$ and $|021\rangle$, (3) $|201\rangle$, and $|102\rangle$, and (4) $|111\rangle$ at various values of U/J. The initial probabilities of finding these basis states in the initial ground state as shown by the diamonds. (b) (points) Number of photon detections $N_d(\theta)$ after 10000 simulations of 1000 detection events each, where the angular range is divided into 600 bins for photon counting. (lines) Scattering distributions predicted by the structure factors of the initial ground states. Parameters used are $g = 0.5$ and $k_0 = \pi/a$.

ture factors for the initial ground states, despite that in the superfluid case the individual realisations do not give the correct distribution.

4.4 Conclusions

Investigating light scattering from small lattices where the Bose-Hubbard model is exactly solvable has allowed us to test our earlier predictions about light scattering from the superfluid and Mott insulator regimes. We have seen that for small number of atoms the mean field and perturbative techniques compare well with the exact diagonalisation. Furthermore, this has allowed us to examine what happens across the transition from superfluid to Mott insulator, where we have found that the light scattering pattern smoothly changes between the two regimes without any new features occurring.

Working in the small lattice regime also raises the question of how the lattice changes after a photon is scattered and detected. We have created a model of the dynamic scattering and detection process, which shows how this pushes the atomic system towards eigenstates of the light scattering measurement process. In some cases this leads to superpositions of the atomic states. This treatment has shown that the light scattering distributions can be predicted by the static structure factor, even when the initial state is significantly perturbed, provided the experiment is repeated a number of times.

In our treatment of the dynamic scattering we have not included the effect of time development due to the atomic Hamiltonian, on the assumption that the light scattering process occurs on a time scale short compared to the tunnelling and interaction time scales. In future work this could be taken into account by evolving the system using the atomic Hamiltonian in between the light scattering events.

Chapter 5

Quantum imaging of spin states in optical lattices

As experiments with optical lattices have advanced, atomic spin has become an important variable [20], and new ways to probe spin distributions must be investigated. Analysis of noise correlations has been discussed as a method of characterising spin states [103], along with quantum polarisation spectroscopy, which provides a non-demolition measurement of the gas's bulk properties under certain conditions [34, 35, 36]. Light scattering observed in the far field has been considered as a method of measuring the Fourier transform of the spin distribution [104], and light scattering has been proposed as a probe of fractional statistics in a Fermi gas in a one dimensional optical lattice [105, 106].

Here we consider imaging the spatial atomic spin distribution while the atoms remain *in situ*, avoiding the destruction of the atomic sample that occurs in time-of-flight imaging. In particular we look at off-resonant light scattered from the atoms, which is then collected by a microscope to form an image on a detector. We consider incoming light from coherent beams and also from spatially correlated

beams. Where in the latter case we build on the ideas developed in the field of quantum imaging [107, 65, 44] to show how the resolution of images can be enhanced and how spatial correlation functions of the atomic spin distribution can be measured. These concepts become increasingly useful for optical lattices where the lattice spacing is often similar to the wavelength of the probe light and coherent imaging becomes less useful due to the diffraction limit.

5.1 Interaction between light and atomic spins

For our imaging proposal, we restrict our attention to off-resonant light scattering from alkali atoms, which we described in Section 2.1. As discussed in Hammerer *et al.* [42] and Appendix 2.B, the polarisability tensor can be decomposed into three irreducible components of rank zero, one and two. The rank zero term leads to a spin-independent interaction, which does not play a part in the imaging interactions we consider here. The rank one term is responsible for the Faraday effect and is the interaction we use for imaging. The rank two term also leads to a spin-dependent interaction but is typically at least an order of magnitude smaller than the second term and goes to zero as the detuning increases (as shown in Appendix 2.B), and we neglect it here.

Recalling the rank one component from Equation (2.15) the interaction is

$$\hat{H} = -a_1(\Delta_{3/2}) \int d\mathbf{r}\hat{\boldsymbol{\rho}}(\mathbf{r}) \cdot (\tilde{\mathbf{E}}^{-}(\mathbf{r}) \times \tilde{\mathbf{E}}^{+}(\mathbf{r})). \tag{5.1}$$

Here $\hat{\boldsymbol{\rho}}(\mathbf{r}) = \sum_{m_1,m_2} \hat{\Psi}^{\dagger}_{m_2}(\mathbf{r})\langle Fm_2|\hat{\mathbf{F}}/\hbar|Fm_1\rangle\hat{\Psi}_{m_1}(\mathbf{r})$ is a vector operating on the atomic spin and $a_1(\Delta_{3/2})$ is the detuning dependent coupling constant given by Equation (2.44).

This effective interaction Hamiltonian describes light scattering from the incoming beam, where photons scatter from the atoms in the lattice and take away

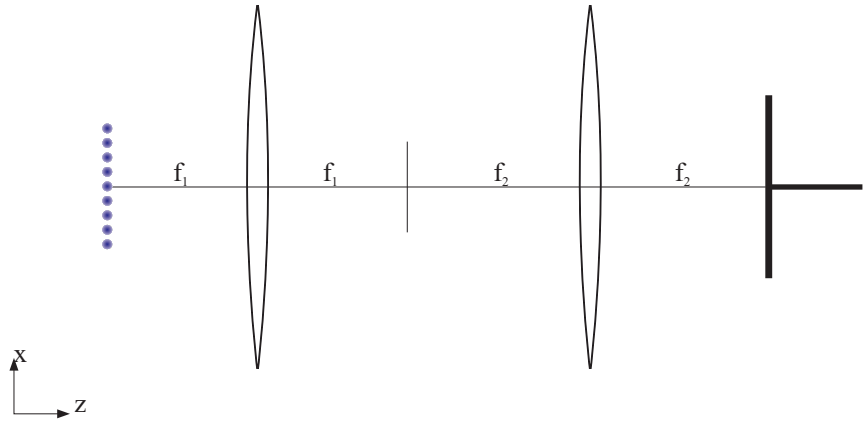

Figure 5.1: Imaging scheme. Light propagating in the z direction interacts with atoms in an optical lattice, then passes through a diffraction limited two lens system and is detected at the focal plane of the second lens.

information about the spin distribution. These photons can then be imaged onto a detector as shown in Figure 5.1. To make calculations for this system practical however, the full three dimensional, multimode interaction Hamiltonian must first be simplified. In considering this type of imaging our primary concern is the spatial description of the light as it interacts with the atoms in the optical lattice and propagates through the system. With this in mind, we assume the photons in the light field are approximately monochromatic with frequency ω. We also consider one-dimensional optical lattices in the x-direction, with the result that the useful variation in an image is also in the x-direction. The system can then be approximately described by a light field that only varies in two dimensions, x and z. Numerical calculations of images for three dimensional systems show that this simplified theory captures the nature of the imaging process well, and provides a good model for images integrated over the y-direction.

Tsang describes the quantization of a two dimensional electromagnetic field in the monochromatic approximation [73]. We generalize Tsang's formalism to include both possible polarizations, in which case the slowly varying electric field

operator becomes

$$\tilde{\mathbf{E}}^{+}(x,z) = i\sum_{\sigma}\sqrt{\frac{\eta}{2\pi}}\int_{-k}^{k} d\kappa\gamma(\kappa)\hat{a}_{\sigma}(\kappa)\boldsymbol{\epsilon}_{\sigma}(\kappa)e^{i\kappa x + i\sqrt{k^2-\kappa^2}z}, \tag{5.2}$$

where $\eta = \hbar k/(2\epsilon_0 L_y \mathcal{T})$, $\gamma(\kappa) = (1-\kappa^2/k^2)^{-1/4}$ and $k = \omega/c = 2\pi/\lambda$. The parameters $\mathcal{T}$ and L_y are the interaction time and extent of the light field in the y-dimension respectively, which enter the formalism as part of the two dimensional approximation [73, 108].

The operators $\hat{a}_1(\kappa)$ and $\hat{a}_2(\kappa)$ destroy photons with wave vector $\kappa\hat{\mathbf{x}} + k\hat{\mathbf{z}}/\gamma(\kappa)^2$ and polarization vectors $\boldsymbol{\epsilon}_1(\kappa) = \hat{\mathbf{x}}/\gamma(\kappa)^2 - \kappa\hat{\mathbf{z}}/k$ and $\boldsymbol{\epsilon}_2(\kappa) = \hat{\mathbf{y}}$ respectively. They obey the commutator relation $[\hat{a}_{\sigma}(\kappa), \hat{a}^{\dagger}_{\sigma'}(\kappa')] = \delta(\kappa-\kappa')\delta_{\sigma,\sigma'}$. Using these operators we can define the N-photon momentum eigenstate [73]

$$|\kappa_1,\ldots\kappa_n\rangle_1 \otimes |\kappa_{n+1},\ldots,\kappa_N\rangle_2 = \frac{1}{\sqrt{n!(N-n)!}}\hat{a}^{\dagger}_1(\kappa_1)\ldots\hat{a}^{\dagger}_1(\kappa_n)\hat{a}^{\dagger}_2(\kappa_{n+1})\ldots\hat{a}^{\dagger}_2(\kappa_N)|0\rangle, \tag{5.3}$$

which has n photons with $\boldsymbol{\epsilon}_1$-polarization and $N-n$ photons with $\boldsymbol{\epsilon}_2$-polarization. These states can then be used as a basis for the general states $|\phi, n, N-n\rangle$ that have n photons with $\boldsymbol{\epsilon}_1$-polarization and $N-n$ photons with $\boldsymbol{\epsilon}_2$-polarization. We have

$$|\phi, n, N-n\rangle = \int_{-k}^{k} d\kappa_1\ldots d\kappa_N \phi(\kappa_1,\ldots,\kappa_N)|\kappa_1,\ldots\kappa_n\rangle_1 \otimes |\kappa_{n+1},\ldots,\kappa_N\rangle_2, \tag{5.4}$$

where we refer to $\phi(\kappa_1,\ldots,\kappa_N)$ as the momentum amplitude of the N-photon state.

We suppose the atoms are in an optical lattice in the x-direction with uniform site separation a and expand the atomic field operators in terms of lowest band Wannier functions $\hat{\Psi}_m(\mathbf{r}) = \sum_j \hat{b}_{j,m} w(\mathbf{r}-\mathbf{r}_j)$, which we assume are not dependent

on the spin state of the atom[1]. The operator $\hat{b}_{j,m}$ destroys an atom with spin m at lattice site j, centred at $\mathbf{r}_j = (x_j, 0, 0)$. We assume the lattice is strong enough so that the Wannier functions have negligible overlap between neighbouring sites, in which case the spin operator becomes

$$\hat{\boldsymbol{\rho}}(\mathbf{r}) = \sum_{j,m_1,m_2} |w(\mathbf{r}-\mathbf{r}_j)|^2 \hat{b}^\dagger_{j,m_2} \hat{b}_{j,m_1} \langle F m_2 | \hat{\mathbf{F}}/\hbar | F m_1 \rangle. \tag{5.5}$$

Integrating over y and z then gives a vector operator dependent only on x

$$\hat{\boldsymbol{\rho}}(x) = \int dydz \hat{\boldsymbol{\rho}}(\mathbf{r}). \tag{5.6}$$

In terms of this spin operator and the two-dimensional electric field the effective interaction Hamiltonian becomes

$$\begin{aligned}\hat{H} = -\frac{a_1(\Delta)\eta}{2\pi} \int dx \int_{-k}^{k} d\kappa_1 d\kappa_2 \gamma(\kappa_1)\gamma(\kappa_2) e^{i(\kappa_2-\kappa_1)x} \\ \times \hat{\boldsymbol{\rho}}(x) \cdot \Big[\Big(\frac{\kappa_1}{k} \hat{a}_1^\dagger(\kappa_1)\hat{a}_2(\kappa_2) - \frac{\kappa_2}{k} \hat{a}_2^\dagger(\kappa_1)\hat{a}_1(\kappa_2) \Big) \hat{\mathbf{x}} \\ + \left(\frac{\kappa_2}{k\gamma(\kappa_1)^2} - \frac{\kappa_1}{k\gamma(\kappa_2)^2} \right) \hat{a}_1^\dagger(\kappa_1)\hat{a}_1(\kappa_2)\hat{\mathbf{y}} \\ + \left(\frac{1}{\gamma(\kappa_1)^2} \hat{a}_1^\dagger(\kappa_1)\hat{a}_2(\kappa_2) - \frac{1}{\gamma(\kappa_2)^2} \hat{a}_2^\dagger(\kappa_1)\hat{a}_1(\kappa_2) \right) \hat{\mathbf{z}} \Big]\end{aligned} \tag{5.7}$$

In deriving Equation (5.7) we used the approximation

$$\int dydz |w(\mathbf{r}-\mathbf{r}_j)|^2 e^{i(\sqrt{k^2-\kappa_2^2}-\sqrt{k^2-\kappa_1^2})z} \approx \int dydz |w(\mathbf{r}-\mathbf{r}_j)|^2 \equiv |w(x-x_j)|^2, \tag{5.8}$$

which is very good for the imaging scenarios we consider, where the Wannier functions are confined in the z-direction tightly compared to the variation of the electric

[1]Scattering involving higher bands can be neglected here because our images are formed from photons scattered in the forward direction, where the higher band scattering is minimised and dominated by elastic scattering.

field in the z-direction.

Furthermore, for the imaging parameters we consider, the term proportional to $\hat{\boldsymbol{\rho}}(x) \cdot \hat{\mathbf{z}} \equiv \hat{\rho}_z(x)$ in the effective Hamiltonian is much larger than the others and determines the dominant features of the images. In the following we neglect the other terms in our theoretical description. These terms lead to small changes that can be easily calculated and are included numerically in the calculations used to produce our figures.

5.2 Light scattering and N-photon imaging

Having derived a description of the interaction between the atomic spins and the light field, we now consider how this interaction leads to light scattering and how the scattered light can be used to image the spin distribution. Taking the atomic spin quantization axis to be $\hat{\mathbf{z}}$, the spin operator in the z-direction is diagonal in atomic spin, that is $\hat{\rho}_z(x) = \sum_j \hat{\rho}_{z,j} |w(x-x_j)|^2$, where $\hat{\rho}_{z,j} = \sum_m m\hat{n}_{j,m}$ and $\hat{n}_{j,m} = \hat{b}^\dagger_{j,m}\hat{b}_{j,m}$. The atomic evolution in the optical lattice due to intersite tunnelling and atom-atom interactions occurs on a time scale of order of the inverse recoil frequency [18]. We will assume that the duration of the light matter interaction is short compared to this time scale and neglect the atomic evolution during the interaction. First order perturbation then mixes the original state of the atom-photon system $|\psi\rangle$ with

$$\int dx \int_{-k}^{k} d\kappa_1 d\kappa_2 e^{i(\kappa_2-\kappa_1)x} \hat{\rho}_z(x) \left(\frac{\gamma(\kappa_2)}{\gamma(\kappa_1)} \hat{a}^\dagger_1(\kappa_1)\hat{a}_2(\kappa_2) - \frac{\gamma(\kappa_1)}{\gamma(\kappa_2)} \hat{a}^\dagger_2(\kappa_1)\hat{a}_1(\kappa_2) \right) |\psi\rangle \tag{5.9}$$

This first order scattering process transforms the initial momentum amplitude of the photons $\phi_i(\kappa_1, \ldots, \kappa_N)$ into the scattered distribution $\phi_s(\kappa_1, \ldots, \kappa_N)$. The imaging system in Figure 5.1 then maps the scattered momentum amplitude to a new momentum amplitude at the detector $\phi_d(\kappa_1, \ldots, \kappa_N)$. Due to the finite extent

of the lenses in the imaging system, the transverse momentum of the photons reaching the detector is restricted to a finite bandwidth, such that $|\kappa| < \kappa_l \equiv k \sin\theta$ where $\sin\theta$ is the numerical aperture of the optical system [75, 109]. This limit, which corresponds to the Rayleigh-Abbe diffraction limit, requires

$$\phi_d(\kappa_1, \ldots, \kappa_N) = \begin{cases} 0 & \text{if any } |\kappa_n| > \kappa_l \\ \phi_s(\kappa_1, \ldots, \kappa_N) & \text{otherwise,} \end{cases} \tag{5.10}$$

where for simplicity we have let $f_1 = f_2$.

We now have a description of the N-photon state at the detector and we are left with the problem of extracting useful information from this state. A measurement of the intensity of the light at the detector provides the simplest form of image, but does not make full use of the multiphoton state. Using an N-photon absorbing material that creates a signal when all N photons arrive at the same point allows us to make better use of the N-photon nature, but may be subject to low efficiency [73]. Recently, as discussed in Section 2.3, it was demonstrated by Tsang that intensity measurements at the detector followed by post-processing can reveal similar information to N-photon absorption [75]. As this method does not rely on the photons all being coincident at a single point it has much higher efficiency.

The variable required in these measurements is the N-photon intensity distribution, $I(x_1, \ldots, x_N) = \sum_{\sigma_1,\ldots,\sigma_N} \langle \tilde{E}^-_{\sigma_N}(x_N) \ldots \tilde{E}^-_{\sigma_1}(x_1) \tilde{E}^+_{\sigma_1}(x_1) \ldots \tilde{E}^+_{\sigma_N}(x_N) \rangle$. At the detector for the state $|\phi, n, N-n\rangle$ this is given by

$$I(x_1, \ldots, x_N) = \sum_P \eta^N \left| \psi_d(P(x_1, \ldots, x_N)) \right|^2 \tag{5.11}$$

where the sum is over all coordinate permutations P and

$$\psi_d(x_1,\ldots,x_N) \equiv \frac{1}{(2\pi)^{N/2}} \int_{-k}^{k} d\kappa_1 \ldots d\kappa_N \exp\left(i\sum_{n=1}^{N}\kappa_n x_n\right) \times \gamma(\kappa_1)\ldots\gamma(\kappa_N)\phi_d(\kappa_1,\ldots,\kappa_N) \quad (5.12)$$

is an N-dimensional transform of the momentum amplitude. The transform of the input light $\psi_i(x_1,\ldots,x_N)$ is defined in the same way. Note that if all photons are in the same polarization state, the momentum amplitude must obey bosonic symmetry so that $\phi(\ldots,\kappa_n,\ldots,\kappa_m,\ldots) = \phi(\ldots,\kappa_m,\ldots,\kappa_n,\ldots)$ for all n and m. In which case $\psi(x_1,\ldots,x_N)$ must obey the same symmetry and is invariant under coordinate permutations.

5.3 Coherent spin imaging

Before studying multiphoton imaging, we first look at the image created by coherent laser photons scattering off the atoms in the optical lattice. We suppose the photons enter the system with $\boldsymbol{\epsilon_2}$ polarisation and momentum amplitude $\phi_i(\kappa)$. First order scattering according to Equation (5.9) will then result in $\boldsymbol{\epsilon_1}$-polarised photons with a momentum amplitude that depends on the atomic field operators,

$$\phi_s(\kappa) = \frac{1}{\gamma(\kappa)} \int_{-k}^{k} d\kappa' \int dx \gamma(\kappa') e^{i(\kappa'-\kappa)x} \phi_i(\kappa') \hat{\rho}_z(x). \quad (5.13)$$

Here, because light scattering off the atoms results in an orthogonal polarisation, the unscattered light can be filtered out and we can detect an image due only to the scattered light [104]. The intensity distribution at the detector will then be

$$I(x) = \eta \langle \psi_d^\dagger(x)\psi_d(x)\rangle \quad (5.14)$$

where

$$\psi_d(x) = \frac{1}{\sqrt{2\pi}} \int_{-\kappa_l}^{\kappa_l} d\kappa \gamma(\kappa) \phi_s(\kappa) e^{i\kappa x} = 2\kappa_l \int dx' \mathrm{sinc}(\kappa_l(x - x'))\psi_i(x')\hat{\rho}_z(x'). \quad (5.15)$$

The result is a diffraction limited image of the spin density weighted by the photons original spatial distribution. The integration over the sinc function in the image amplitude $\psi_d(x)$ blurs the image, but has the useful side effect that the image depends on the spin correlation function $\langle \hat{\rho}_z(x')\hat{\rho}_z(x'')\rangle$.

5.4 Two-photon spin image

We next consider the scattering of a two-photon state from the atoms in the optical lattice and the resulting two-photon intensity distribution. We take the initial state to have one $\boldsymbol{\epsilon_1}$-polarised photon and one $\boldsymbol{\epsilon_2}$-polarised photon, then first order scattering from this state will result in a state with two photons with the same polarisation. The photons in the final state will then be indistinguishable and knowledge of which photon was scattered is lost. Using polarisation filters or beam splitters, we can then detect only two-photon states with two photons in the same polarisation state. The resulting image is then due to pairs of photons containing one scattered photon and one unscattered photon. If we filter out $\boldsymbol{\epsilon_2}$-polarised photons, the two-photon intensity distribution is

$$I(x_1, x_2) = \langle \tilde{E}_1^-(x_1)\tilde{E}_1^-(x_2)\tilde{E}_1^+(x_2)\tilde{E}_1^+(x_1)\rangle = 2\eta^2 \langle \psi_d^\dagger(x_1, x_2)\psi_d(x_1, x_2)\rangle \quad (5.16)$$

where

$$\psi_d(x_1, x_2) = \sqrt{2}\kappa_l \int dx \hat{\rho}_z(x) \left(\mathrm{sinc}(\kappa_l(x_1 - x))\psi_i(x_2, x) + \mathrm{sinc}(\kappa_l(x_2 - x))\psi_i(x_1, x)\right). \quad (5.17)$$

The amplitude $\psi_d(x_1, x_2)$ consists of two terms resulting from the two indistinguishable paths the photons could have taken to reach x_1 and x_2, that is, the scattered photon reaching x_1 and the unscattered photon reaching x_2 and *vice versa*. For simplicity, here we have assumed that the photon source is also limited in transverse momentum by κ_l.

The use of two-photon absorption imaging can now lead to higher resolution than that of the coherent spin image discussed in the previous section. If the initial two-photon state is generated by parametric down conversion, then the transverse momenta of the photons is typically anti-correlated [110]. If we take the initial momentum amplitude to be approximately $\phi_i(\kappa_1, \kappa_2) = \delta(\kappa_1 + \kappa_2)$ for $|\kappa_1|, |\kappa_2| < \kappa_l$ and zero elsewhere, then the spatial distribution is $\psi_i(x, x') = \kappa_l \text{sinc}[\kappa_l(x - x')]/\pi$. In this case the two-photon absorption image depends on the amplitude

$$\psi_d(x_1, x_1) = \frac{\sqrt{8}\kappa_l^2}{\pi} \int dx \hat{\rho}_z(x) \text{sinc}^2(\kappa_l(x_1 - x)). \tag{5.18}$$

Comparing this with the coherent imaging amplitude in Equation (5.15), we see that using two photons here results in the sinc function being raised to the power of two, allowing an image with higher resolution. In general for an N-photon state this type of imaging results in an improvement in resolution that scales like $\sqrt{N}$ [107].

A two-photon absorption image requires two photon detectors. A more efficient way to acquire the resolution improvement is to calculate the centroid distribution of the two-photon intensity distribution [75]. In place of the Cartesian coordinates we can express the system in terms of the centroid and relative positions of the two photons

$$X \equiv \frac{x_1 + x_2}{2}, \qquad \xi \equiv \frac{x_1 - x_2}{2}. \tag{5.19}$$

For the parametric down converted source described above the centroid probability

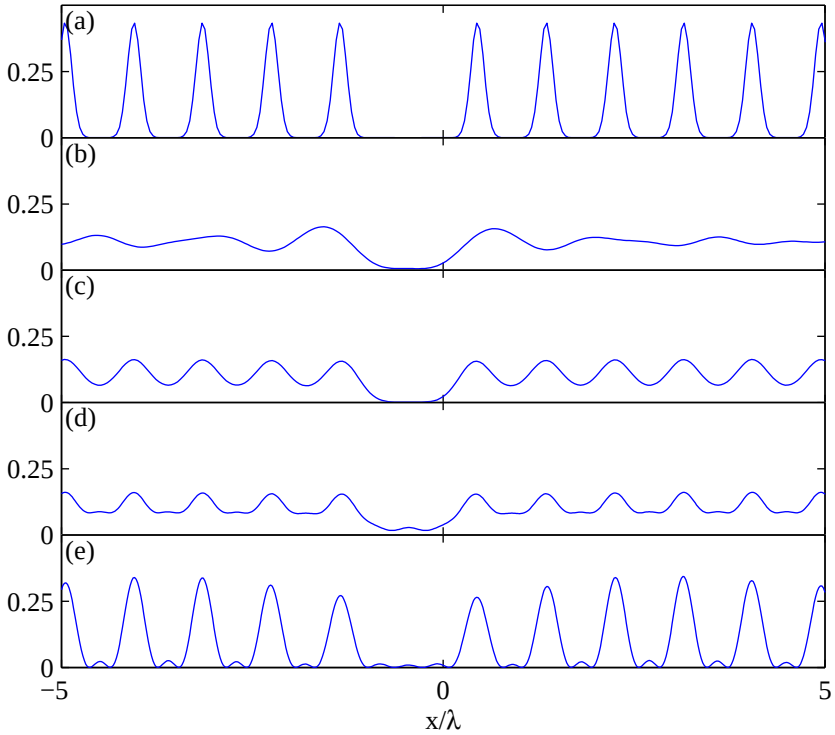

Figure 5.2: Normalised images of a lattice containing atoms all in the $m = 1$ state with a defect. a) The lattice spin density to be imaged. b) The coherent image. c) The two-photon absorption image. d) The centroid distribution for the two-photon intensity distribution (Equation (5.20)). e) The centroid of the two-photon amplitude (Equation (5.23)). Here the lattice site separation is $a = 0.9\lambda$, the lattice strength is $V_0 = 30E_R$ and the imaging system has numerical aperture $\sin\theta = 2/3$.

distribution (unnormalised) is

$$\int d\xi \langle \psi_d^\dagger(X+\xi, X-\xi)\psi_d(X+\xi, X-\xi)\rangle = \frac{8(\kappa_l)^4}{\pi^2}\int dx dx' \langle \hat{\rho}_z(x)\hat{\rho}_z(x')\rangle K(X,x,x'), \quad (5.20)$$

where

$$K(X,x,x') = \int d\xi \mathrm{sinc}(\kappa_l(X+\xi-x))\mathrm{sinc}(\kappa_l(X-\xi-x)) \times \mathrm{sinc}(\kappa_l(X+\xi-x'))\mathrm{sinc}(\kappa_l(X-\xi-x')). \quad (5.21)$$

The resulting image has a similar resolution improvement to the two-photon absorption image, but is expected to be simpler to obtain in an experiment.

If we could measure the amplitude $\langle \psi(x_1, x_2)\rangle$ directly, for example by spatial quantum state tomography [111], then the centroid measurement applied to the amplitude would result in an image with higher resolution still. Using the identity

$$\int_{-\infty}^{\infty} dx \mathrm{sinc}(b(x+y))\mathrm{sinc}(b(z-x)) = \frac{\pi}{b}\mathrm{sinc}(b(y+z)) \quad (5.22)$$

the probability distribution (unnormalised) of the centroid becomes

$$\left|\int d\xi \langle \psi(X+\xi, X-\xi)\rangle\right|^2 = 8\kappa_l^2 \left|\int dx \langle \hat{\rho}_z(x)\rangle \mathrm{sinc}(2\kappa_l(X-x))\right|^2. \quad (5.23)$$

The factor of two is now inside the sinc function, leading to a factor of two resolution improvement over the coherent case. However, the requirement for quantum state tomography means that this would be significantly more difficult to achieve in an experiment.

In Figure 5.2 we compare the various possible images described above. The images are of an optical lattice with a single $m = 1$ atom at each site except for a

missing or $m = 0$ atom at $x = -a/2$. The lattice site separation is 0.9 times the wavelength of the imaging light and the optical system has a numerical aperture of 2/3. For these parameters the coherent image allows the identification of the defect in the optical lattice filling, but does not resolve the individual sites. The two-photon absorption image and the centroid of the two-photon intensity distribution both resolve the individual sites. The centroid of the two-photon amplitude resolves the sites with an improved visibility.

The precise resolving power of each image type depends on the lattice properties, but a rough guide is that in the coherent image it becomes difficult to resolve individual sites for site spacings below $a \sim \lambda/\sin\theta$, while for the two-photon amplitude centroid this limit is halved. For the two-photon absorption and two-photon intensity centroid images individual peaks associated with each lattice also develop around $a \sim \lambda/(2\sin\theta)$, as in the amplitude centroid image, but the visibility of these peaks is lower than for the amplitude centroid image.

5.5 Images of example spin states

We now apply our imaging proposal to example spin states of atoms in an optical lattice. For an optical lattice with a single spin-1 atom at each site, the ground state potentially consists of dimers [112]. This occurs when neighbouring sites form a spin singlet (total spin equal to zero). Denoting site j's spin states $m = +1, 0, -1$ by $|+\rangle_j$,$|0\rangle_j$ and $|-\rangle_j$ respectively, a dimerised state of an M-site lattice (M even) is represented by

$$\bigotimes_{j=1}^{M/2} \frac{1}{\sqrt{3}} \left(|+\rangle_{2j}|-\rangle_{2j-1} + |-\rangle_{2j}|+\rangle_{2j-1} - |0\rangle_{2j}|0\rangle_{2j-1}\right). \tag{5.24}$$

The coherent imaging intensity can be rewritten in terms of the site correlation

functions as

$$I(x) = 4\eta\kappa_l^2 \sum_{j,r} \langle \hat{\rho}_{z,j}\hat{\rho}_{z,r}\rangle f(x - x_j) f(x - x_r) \tag{5.25}$$

where

$$f(x) = \int dx' |w(x')|^2 \mathrm{sinc}(\kappa_l(x - x')) \tag{5.26}$$

is the image amplitude resulting from the lattice site Wannier function. For the dimer case $\langle \hat{\rho}_{z,j}^2\rangle = 2/3$, $\langle \hat{\rho}_{z,2j-1}\hat{\rho}_{z,2j}\rangle = -2/3$ for integer j and $\langle \hat{\rho}_{z,j}\hat{\rho}_{z,r}\rangle = 0$ otherwise. The intensity then becomes

$$I(x) = \frac{8\eta\kappa_l^2}{3} \sum_{j=1}^{M/2} \left(f(x - x_{2j-1}) - f(x - x_{2j})\right)^2 . \tag{5.27}$$

From this form we see that the atomic correlations lead to interference in the resulting image. In particular, at the centre of each dimer pair, $x = (x_{2j-1} + x_{2j})/2$, the contribution to the image from the atoms in the dimer at x_{2j-1} and x_{2j} cancel, and we are left with a background intensity due to the other atoms. This cancellation leads to local minima in the image at the centre of each dimer pair. The cancellation does not occur at $x = (x_{2j} + x_{2j+1})/2$ between atoms from separate dimers. For a lattice spacing $a \leq 1/(2\sin\theta)$ the images of sites $2j$ and $2j + 1$ are no longer resolved and merge at $x = (x_{2j} + x_{2j+1})/2$ to form local maxima. Thus, below the diffraction limit, the image is an oscillation with double the spatial period of the lattice due to the paring of atoms. This pattern persists until oscillations with double the lattice period can no longer be resolved.

Another potential state of the spin-1 chain is a trimerised state, where three neighbouring sites form a singlet [113]. A trimerised state of an M-site lattice (M multiple of three) is

$$\bigotimes_{j=1}^{M/3} \frac{1}{\sqrt{6}} \left(|+0-\rangle_j + |-+0\rangle_j + |0-+\rangle_j - |+-0\rangle_j - |0+-\rangle_j - |-0+\rangle_j\right) \tag{5.28}$$

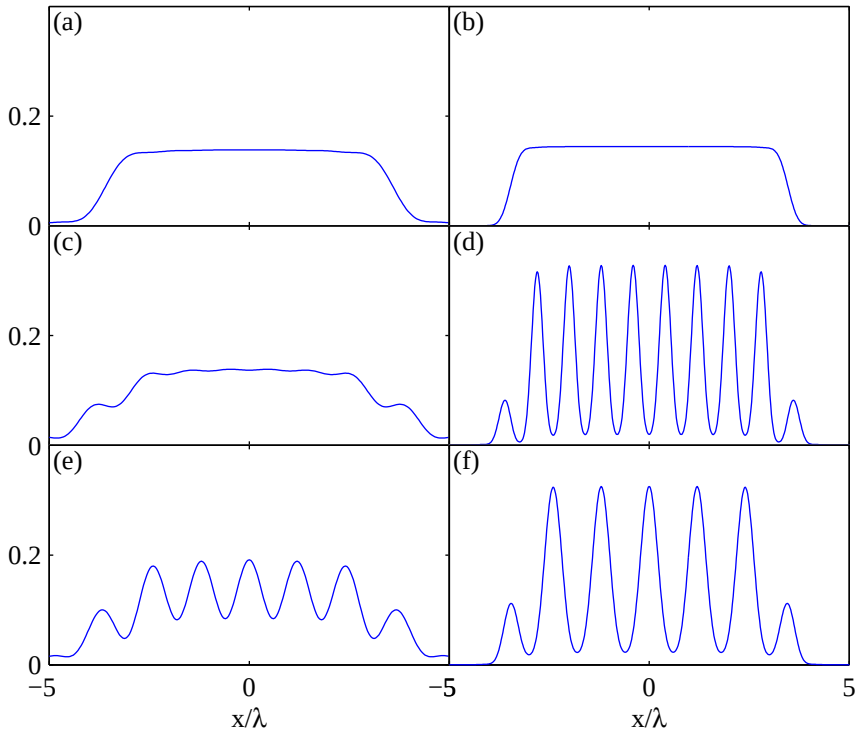

Figure 5.3: Normalised coherent (left column) and two-photon intensity centroid (right column) images of an 18 atom spin chain in the (a-b) unpolarised state, (c-d) dimer state and (e-f) trimer state. The images are for a lattice spacing $a = 0.4\lambda$ and the optical system has numerical aperture $\sin\theta = 1/2$.

where $|m_1 m_2 m_2\rangle_j = |m_1\rangle_{3j-2}|m_2\rangle_{3j-1}|m_3\rangle_{3j}$. In this case $\langle\hat{\rho}^2_{z,j}\rangle = 2/3$, $\langle\hat{\rho}_{z,3j-2}\hat{\rho}_{z,3j-1}\rangle = \langle\hat{\rho}_{z,3j-2}\hat{\rho}_{z,3j}\rangle = \langle\hat{\rho}_{z,3j-1}\hat{\rho}_{z,3j}\rangle = -2/6$ for integer j and $\langle\hat{\rho}_{z,j}\hat{\rho}_{z,r}\rangle = 0$ otherwise. The coherent image intensity then becomes

$$I(x) = \frac{4\eta\kappa_l^2}{3}\sum_{j=1}^{M/3}\big((f(x-x_{3j-2}) - f(x-x_{3j-1}))^2 + (f(x-x_{3j-2}) - f(x-x_{3j}))^2 + (f(x-x_{3j-1}) - f(x-x_{3j}))^2\big)\,. \quad (5.29)$$

As in the case of the dimer, the atomic correlations lead to interference in the image. In this case the interference results in an oscillation with three times the spatial period of the lattice, with local minima at the centre of each trimer and maxima at the points between separate trimers.

The same effects occur in the two-photon images of both the dimer and trimer, but due to the greater resolving power they are visible for smaller lattice site spacings. In Figure 5.3 the coherent and two-photon intensity centroid images of the the dimer and trimer states are compared with the unpolarised state that has $\langle\hat{\rho}_{z,j}\rangle = 0$, $\langle\hat{\rho}^2_{z,j}\rangle = 2/3$ and $\langle\hat{\rho}_{z,j}\hat{\rho}_{z,r}\rangle = 0$ for $j \neq r$. The images are generated for parameters where the dimer oscillations become difficult to resolve in the coherent image. The dimer oscillations in the coherent image become unresolvable for lattice spacings below $a \sim 0.2\lambda/\sin\theta$, whereas the oscillations in the two photon image become unresolvable at $a \sim 0.14\lambda/\sin\theta$. The oscillations in the trimer state become unresolved in the coherent image below $a \sim 0.16\lambda/\sin\theta$, and in the two-photon image below $a \sim 0.1\lambda/\sin\theta$.

5.6 Spatial correlation measurements

Another potential use of two-photon imaging is to examine local spatial correlations in the atomic lattice that cannot be accessed using methods that probe the entire sample [35, 36, 34]. If we have light that is spatial correlated as $\psi_i(x, x') = \kappa_l\{\mathrm{sinc}[\kappa_l(x - x' - a)] + \mathrm{sinc}[\kappa_l(x - x' + a)]\}/(\sqrt{2}\pi)$, so that the two photons are separated by a, then the two-photon image amplitude (Equation (5.17)) becomes

$$\psi_d(x_1, x_2) = \frac{\kappa_l^2}{\pi}\int dx[\hat{\rho}_z(x) + \hat{\rho}_z(x + a)] \times \{\mathrm{sinc}[\kappa_l(x_1 - x)]\mathrm{sinc}[\kappa_l(x_2 - x - a)] + \mathrm{sinc}[\kappa_l(x_1 - x - a)]\mathrm{sinc}[\kappa_l(x_2 - x)]\}. \quad (5.30)$$

A measurement of the two-photon intensity distribution at $x_1 = x$ and $x_2 = x + a$ then depends on $\langle(\hat{\rho}_z(x) + \hat{\rho}_z(x + a))^2\rangle$. For an optical lattice, if the two photon resolution is such that $\int dx|w(x)|^2\mathrm{sinc}^2(\kappa_l x) \gg \int dx|w(x)|^2\mathrm{sinc}^2(\kappa_l(x - a))$ then

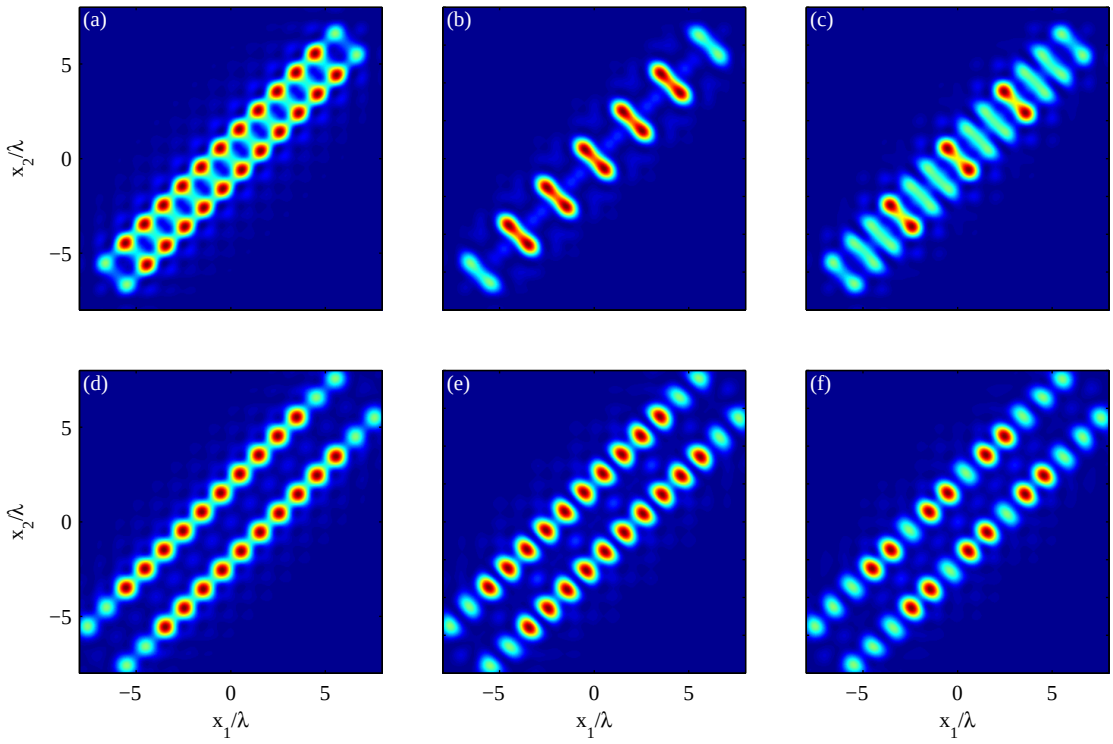

Figure 5.4: (Color online) Two-photon intensity distributions resulting from a 12 atom spin chain in various states. In (a-c) the imaging photons are initially correlated to be separated by a, and in (e-f) by $2a$. The images are of (a) and (e) the unpolarised state, (b) and (d) the dimer state, (c) and (f) the trimer state. The imaging system has $\sin\theta = 1/2$ and the imaging light has $\lambda = a$.

the main contribution to the two-photon distribution at $(x_1, x_2) = (x_j, x_{j+1})$ is

$$\langle \psi_d^\dagger(x_j, x_{j+1})\psi_d(x_j, x_{j+1})\rangle \approx \frac{\kappa_l^4}{\pi^2}\langle(\hat{\rho}_{z,j} + \hat{\rho}_{z,j+1})^2\rangle \left(\int dx |w(x)|^2 \mathrm{sinc}^2(\kappa_l x)\right)^2 . \tag{5.31}$$

This allows us to access the neighbour correlation using $\langle(\hat{\rho}_{z,j} + \hat{\rho}_{z,j+1})^2\rangle = \langle\hat{\rho}_{z,j}^2 + \hat{\rho}_{z,j+1}^2\rangle + 2\langle\hat{\rho}_{z,j}\hat{\rho}_{z,j+1}\rangle$. For the dimer state the atoms of a dimer pair have a neighbour correlation leading to $I(x_{2j-1}, x_{2j}) \approx \langle\rho_{2j-1}^2 + \rho_{2j}^2\rangle + 2\langle\rho_{2j-1}\rho_{2j}\rangle = 0$. There is no neighbour correlation between atoms of separate dimers leading to $I(x_{2j}, x_{2j+1}) \approx \langle\hat{\rho}_{z,2j}^2 + \hat{\rho}_{z,2j+1}^2\rangle = 4/3$. For the trimer state the correlation between neighbours in a trimer leads to $I(x_{3j-2}, x_{3j-1}) = I(x_{3j-1}, x_{3j}) \approx 2/3$, while atoms of separate trimers have no correlation leading to $I(x_{3j}, x_{3j+1}) \approx 4/3$.

In Figure 5.4(a-c) we compare the resulting two-photon intensity distributions for the trimer and dimer states with the unpolarised state. In the dimer image, Figure 5.4(b), the correlations between atoms in the dimer state lead to the removal of every second peak when compared to the unpolarised state image, while in the trimer image, Figure 5.4(c), correlations lead to partial cancellation of two out of three peaks.

Similarly, if we consider light correlated so that photons in the initial pair are separated by $2a$, the two-photon intensity distribution then probes the correlation $\langle\hat{\rho}_{z,j}\hat{\rho}_{z,j+2}\rangle$. For the dimer no such correlations exist and cancellation does not occur as it did in the previous example. The trimer does have correlations over this range and partial cancellation of peaks occurs at photon coordinates $(x_1, x_2) = (x_{3j-2}, x_{3j})$ and (x_{3j}, x_{3j-2}). This behaviour is shown in Figure 5.4(d-e).

5.7 Conclusions

In this chapter we have demonstrated how coherent *in situ* imaging can distinguish between spin states in an optical lattice. Furthermore, we have shown how the use of spatially correlated light can improve the resolution of these images and allow us to distinguish spin states beyond the limits imposed by Rayleigh diffraction. We have also demonstrated a method that uses spatially correlated light to directly probe the local spatial correlation function of the atoms. While we have restricted most of our attention here to two-photon imaging due to the relative ease of generating two-photon states in experiments, future work could generalise these results to higher photon number states, where further improvements in resolution should be possible.

Chapter 6

Imaging of fractional spin Hall states

Electrons that are confined to two dimensions and cooled to within a few degrees of absolute zero behave in ways that have fascinated condensed matter physicists for decades. This began in 1980 when von Klitzing *et al.* performed an experiment with a cold electron system and observed plateaus in the Hall resistance as magnetic field was varied [114]. The Hall resistance was exactly quantised at these plateaus to a value of $h/(ne^2)$, where n is a positive integer, and this phenomena is hence referred to as the integer quantum Hall effect. This effect can be understood in terms on non-interacting electrons and is due to complete filling of Landau levels, which are the sets of degenerate single-particle electron orbitals.

This discovery was soon followed by the observation of a similar effect, where the Hall resistance was exactly quantised as $h/(\nu e^2)$, with ν a fraction, 1/3 in this case [115]. This fractional quantum Hall effect occurs when the Landau levels are partially filled, with filling factor ν, and the interactions between the electrons drive the gas into a strongly correlated state. This effect cannot be understood using

perturbation theory and much of the current understanding is due to proposal of trial wave functions, such as the celebrated Laughlin wavefunction [116].

Recently in addition to the standard quantum Hall effect, which exists in spin-polarised electron gases, a quantum spin Hall effect was predicted to occur in solid state materials [117, 118, 119, 120] and was demonstrated experimentally [121]. This effect exists in samples where there is a spin-orbit coupling and does not require a magnetic field. The quantum spin Hall effect does not break time-reversal symmetry and a quantum phase transition from a normal insulator to a topological insulator can occur [120, 121]. Non-trivial topological states such as those that occur in the quantum spin Hall effect are currently generating a lot of interest in part due to the goal of creating a topological quantum computer.

The above effects have all been detected in semi-conductor materials that have their properties defined and limited by their composition. A more flexible realisation of these effects may be possible in ultracold atoms. A promising direction towards achieving these states is via optical means, where a synthetic magnetic field can be induced for neutral atoms [37] providing a way to achieve the quantum Hall effect. Furthermore, the spin Hall effect may also be produced by optical means [122, 123] and interactions between particles can then lead to the fractional quantum spin Hall effect [124].

Effective means of probing these states in ultracold gases must be developed. Destructive methods involving Bragg scattering [38, 125] and density measurement [126] have been suggested to probe the global properties of topological insulating states. Here, we apply the spin imaging methods discussed in Chapter 5, as well as some additional methods, to examine how well we can probe local properties of an ultracold Bose gas in the quantum Hall regime while the atoms remain *in situ*.

6.1 Spin Hall states in Bose gases

Liu *et al.* propose that the fractional spin Hall effect can be realised in a two dimensional gas of ultracold bosons by applying optical beams with orbital angular momentum [124]. The spatial dependence of the light-atom coupling then leads to the opposite spin states (in this case dressed hyperfine states) experiencing effective magnetic fields in opposite directions. Two potential ground states may then be produced, which are of the form originally proposed by Halperin [127], these are

$$\Phi_n = \left(\prod_{j<l}^{N/2} (z_j - z_l)^2 (\zeta_j - \zeta_l)^2 \right) \left(\prod_{u,v}^{N/2} (z_u - \zeta_v)^n e^{-|z_u|^2/2 - |\zeta_v|^2/2} \right), \tag{6.1}$$

with $n = 1$ or 2. These wavefunctions states are expressed in terms of the variables $z_j = (x_j + iy_j)/\ell$ and $\zeta_j = (x_{N/2+j} + iy_{N/2+j})/\ell$, where $\mathbf{x}_j = (x_j, y_j)$ are the coordinates of the atoms. The indices $j = 1$ through $N/2$ refer to the spin up atoms and $N/2+1$ through N to spin down. The characteristic length scale $\ell = \sqrt{\hbar/(eB)}$ is determined by the effective magnetic field B generated by the optical field, and is of the order of a few microns for the parameters discussed in Liu *et al.* [124]. The two states have associated fractional filling factors $\nu_1 = 1/3$ and $\nu_2 = 1/4$.

6.2 Imaging the spin distribution

We now apply the theory developed in the previous chapter to calculate spin images of these fractional spin Hall states. Because the states are two-dimensional, we must generalize the theory to include both transverse directions of the electric field in the image formation. We use the same spin-light interaction as before, recalling

Equation (5.1),

$$\hat{H} = -a_1(\Delta_{3/2}) \int d\mathbf{r} \hat{\boldsymbol{\rho}}(\mathbf{r}) \cdot (\tilde{\mathbf{E}}^{-}(\mathbf{r}) \times \tilde{\mathbf{E}}^{+}(\mathbf{r})). \tag{6.2}$$

However the monochromatic electric field is now three dimensional

$$\tilde{\mathbf{E}}^{+}(\mathbf{x}, z) = i \sum_{\sigma} \frac{\sqrt{\eta}}{2\pi} \int_{\mathcal{K}} d\boldsymbol{\kappa} \gamma(\boldsymbol{\kappa}) \hat{a}_{\sigma}(\boldsymbol{\kappa}) \boldsymbol{\epsilon}_{\sigma}(\boldsymbol{\kappa}) e^{i\boldsymbol{\kappa}\cdot\mathbf{x} + ikz/\gamma(\boldsymbol{\kappa})^2}, \tag{6.3}$$

where $\eta = \hbar k/(2\epsilon_0 \mathcal{T})$, $\gamma(\boldsymbol{\kappa}) = (1 - |\boldsymbol{\kappa}|^2/k^2)^{-1/4}$, $k = \omega/c = 2\pi/\lambda$, $\mathcal{T}$ is the interaction time scale [73] and the integration region is $\mathcal{K} = \{\boldsymbol{\kappa} = (\kappa_x, \kappa_y) : |\boldsymbol{\kappa}| < k\}$ [128]. The operators $\hat{a}_1(\boldsymbol{\kappa})$ and $\hat{a}_2(\boldsymbol{\kappa})$ destroy photons with wavevector $\kappa_x \hat{\mathbf{x}} + \kappa_y \hat{\mathbf{y}} + k\hat{\mathbf{z}}/\gamma(\boldsymbol{\kappa})^2$ and polarisation vectors $\boldsymbol{\epsilon}_1(\boldsymbol{\kappa}) = (\hat{\mathbf{x}}/\gamma(\boldsymbol{\kappa})^2 - \kappa_x \hat{\mathbf{z}}/k)/\sqrt{1 - \kappa_y^2/k^2}$ and $\boldsymbol{\epsilon}_2(\boldsymbol{\kappa}) = (-\kappa_x \kappa_y \hat{\mathbf{x}}/k^2 + (1 - \kappa_y^2/k^2)\hat{\mathbf{y}} - \kappa_y \hat{\mathbf{z}}/(k\gamma(\boldsymbol{\kappa})^2))/\sqrt{1 - \kappa_y^2/k^2}$ respectively. They obey the commutator relation $[\hat{a}_{\sigma}(\boldsymbol{\kappa}), \hat{a}_{\sigma'}(\boldsymbol{\kappa}')] = \delta(\kappa_x - \kappa_x')\delta(\kappa_y - \kappa_y')\delta_{\sigma,\sigma'}$.

We can now follow a similar procedure as in the previous chapter to simplify the light-matter interaction. As before, the dominant features of the image are due to the z component of the spin operator $\hat{\boldsymbol{\rho}}(\mathbf{x})$, and in this chapter we will neglect the corrections due to the other terms. To first order the light-matter interaction then mixes the original state of the system $|\psi\rangle$ with

$$\int d\mathbf{x} \int_{\mathcal{K}} d\boldsymbol{\kappa} d\boldsymbol{\kappa}' \frac{\gamma(\boldsymbol{\kappa}')\sqrt{1 - \kappa_y'^2/k^2}}{\gamma(\boldsymbol{\kappa})\sqrt{1 - \kappa_y^2/k^2}} \left(e^{i(\boldsymbol{\kappa}' - \boldsymbol{\kappa})\cdot\mathbf{x}} \hat{a}_1^{\dagger}(\boldsymbol{\kappa}) \hat{a}_2(\boldsymbol{\kappa}') - \text{H.c.} \right) \hat{\rho}_z(\mathbf{x}) |\psi\rangle \tag{6.4}$$

where $\rho_z(\mathbf{x}) = \sum_m m \hat{\Psi}_m^{\dagger}(\mathbf{x}) \hat{\Psi}_m(\mathbf{x})$. The factors of $\sqrt{1 - \kappa_y^2/k^2}$ here result in corrections to the images of the same order of the terms we neglected above due to the x and y components of the spin operator, and we neglect these in all the imaging scenarios below except the far field case.

For the wavefunctions described by Equation (6.1) the many-body state to be

imaged is

$$|\Phi_n\rangle = \frac{1}{\sqrt{\mathcal{N}}} \int d\mathbf{x}_1 \cdots d\mathbf{x}_N \Phi_n(\mathbf{x}_1, \cdots, \mathbf{x}_N) \times \hat{\Psi}_+^\dagger(\mathbf{x}_1) \cdots \hat{\Psi}_+^\dagger(\mathbf{x}_{N/2}) \hat{\Psi}_-^\dagger(\mathbf{x}_{N/2+1}) \cdots \hat{\Psi}_-^\dagger(\mathbf{x}_N)|0\rangle, \quad (6.5)$$

with normalisation factor $\mathcal{N} = [(N/2)!]^2 \int d\mathbf{x}_1 \cdots d\mathbf{x}_N |\Phi_n(\mathbf{x}_1, \cdots, \mathbf{x}_N)|^2$. In which case the light scattering described by Equation (6.4) results in an image

$$I(\boldsymbol{\chi}) = \sum_{m,m'} mm' \int d\mathbf{x} d\mathbf{x}' \langle \Phi_n | \hat{\Psi}_m^\dagger(\mathbf{x}) \hat{\Psi}_m(\mathbf{x}) \hat{\Psi}_{m'}^\dagger(\mathbf{x}') \hat{\Psi}_{m'}(\mathbf{x}') | \Phi_n \rangle f^*(\mathbf{x}, \boldsymbol{\chi}) f(\mathbf{x}', \boldsymbol{\chi}), \quad (6.6)$$

where the function $f(\mathbf{x}, \boldsymbol{\chi})$ is determined by the properties of the imaging process and $\boldsymbol{\chi}$ denotes the imaging coordinates. Evaluating the expectation value gives

$$I(\boldsymbol{\chi}) = \frac{\int d\mathbf{x}_1 \cdots d\mathbf{x}_N |\Phi_n(\mathbf{x}_1, \cdots, \mathbf{x}_N)|^2 \mathcal{O}(\boldsymbol{\chi}, \mathbf{x}_1, \cdots, \mathbf{x}_N)}{\int d\mathbf{x}_1 \cdots d\mathbf{x}_N |\Phi_n(\mathbf{x}_1, \cdots, \mathbf{x}_N)|^2}, \quad (6.7)$$

where

$$\mathcal{O}(\boldsymbol{\chi}, \mathbf{x}_1, \cdots, \mathbf{x}_N) = \left| \sum_{j=1}^{N/2} f(\mathbf{x}_j, \boldsymbol{\chi}) - \sum_{j=N/2+1}^{N} f(\mathbf{x}_j, \boldsymbol{\chi}) \right|^2. \quad (6.8)$$

For any reasonable number of atoms the integration over the many-body wavefunctions in Equation (6.7) is not suitable for exact computation, and we resort to using the Metropolis Monte Carlo method [129]. This method approximates the image by calculating the sum $I(\boldsymbol{\chi}) \approx \frac{1}{M} \sum_{n=1}^{M} \mathcal{O}(\boldsymbol{\chi}, \mathbf{R}^{(n)})$ for M coordinate configurations $\mathbf{R}^{(n)} = \{\mathbf{x}_1^{(n)}, \cdots, \mathbf{x}_N^{(n)}\}$ distributed according to the probability distribution $|\Phi_n(\mathbf{R}^{(n)})|^2$. The coordinate configurations are generated by the Metropolis algorithm, which involves a random walk through N-particle coordinate space that favours steps towards points of higher probability according to the wavefunction.

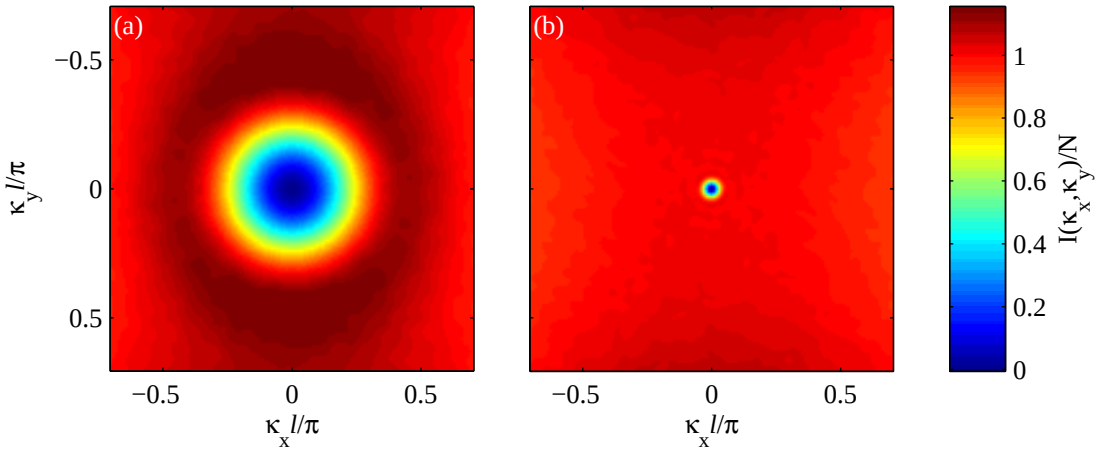

Figure 6.1: Far field images of the spin quantum Hall ground states, with (a) $n = 1$ and (b) $n = 2$.

6.2.1 Coherent far field imaging

One of the simplest methods of imaging the system is to illuminate the sample with coherent light and then let the scattered light propagate into the far field, where the distance from the sample is much greater than the wavelength of the imaging light. In this region the spatial dependence of the light is simply determined by the Fourier components of the scattered light. For photons from a coherent beam entering the system with $\boldsymbol{\epsilon_2}$ polarisation and momentum distribution $\phi_i(\boldsymbol{\kappa})$, the first order scattering results in $\boldsymbol{\epsilon_1}$-polarised photons with a momentum distribution that depends on the atomic field operators according to

$$\phi_s(\boldsymbol{\kappa}) = \frac{1}{\gamma(\boldsymbol{\kappa})\sqrt{1-\kappa_y^2/k^2}} \int_{\mathcal{K}} d\boldsymbol{\kappa}' \int d\mathbf{x}\gamma(\boldsymbol{\kappa}')\sqrt{1-\kappa_y'^2/k^2}\, e^{i(\boldsymbol{\kappa}'-\boldsymbol{\kappa})\cdot\mathbf{x}}\phi_i(\boldsymbol{\kappa}')\hat{\rho}_z(\mathbf{x}). \tag{6.9}$$

If we then filter out the $\boldsymbol{\epsilon_2}$ polarised light, we get an image in the far field that is determined by $I(\zeta\mathbf{x}) = I(\boldsymbol{\kappa}) = \langle\phi_s^\dagger(\boldsymbol{\kappa})\phi_s(\boldsymbol{\kappa})\rangle$. Here the scaling constant ζ depends on the distance from the sample to the detector, and determines the spatial size of the image.

In Figure 6.1 we show the far field images of the states from Equation (6.1).

These images are generated by averaging over 100000 Monte Carlo configurations of 100 particles. The input beam is assumed to be a plain wave with $\phi_i(\boldsymbol{\kappa}') = \delta(\boldsymbol{\kappa}')$ and the imaging light has wavelength $\lambda = \ell$. The far field image allows us to distinguish the two grounds states, both images go to zero at $\boldsymbol{\kappa} = \mathbf{0}$ but the image for $n = 1$ goes toward zero over a much larger range. This is because for the $n = 1$ state the atoms of opposite spin are allowed to exist closer to each other than particles of the same spin, leading to long wavelength oscillations in the far field that create the large dip in the $n = 1$ image. For $n = 2$ the particles of opposite spin interact in the same way as particles of same spin and these long wavelength oscillations do not occur.

6.2.2 Coherent imaging with a microscope

We now look at the images created by the microscope imaging system we used in the previous chapter and is shown in Figure 5.1. Once again we illuminate the sample with coherent $\boldsymbol{\epsilon_2}$-polarised light that is filtered out before detection. For the two-dimensional system the intensity of the scattered light at the detector after passing through the imaging system is

$$I(\mathbf{x}) = \eta \langle \psi_d^\dagger(\mathbf{x}) \psi_d(\mathbf{x}) \rangle \tag{6.10}$$

where

$$\psi_d(\mathbf{x}) = 2\pi\kappa_l \int d\mathbf{x}' \frac{J_1(\kappa_l |\mathbf{x} - \mathbf{x}'|)}{|\mathbf{x} - \mathbf{x}'|} \psi_i(\mathbf{x}') \hat{\rho}_z(\mathbf{x}'). \tag{6.11}$$

The point spread function is now $J_1(x)/x$, where $J_1(x)$ is a Bessel function of the first kind, compared with the sinc function of our two-dimensional theory in Chapter 5.

The spin quantum Hall wavefunction from Equation (6.1) leads to particle configurations that are strongly correlated where atoms avoid the positions of other

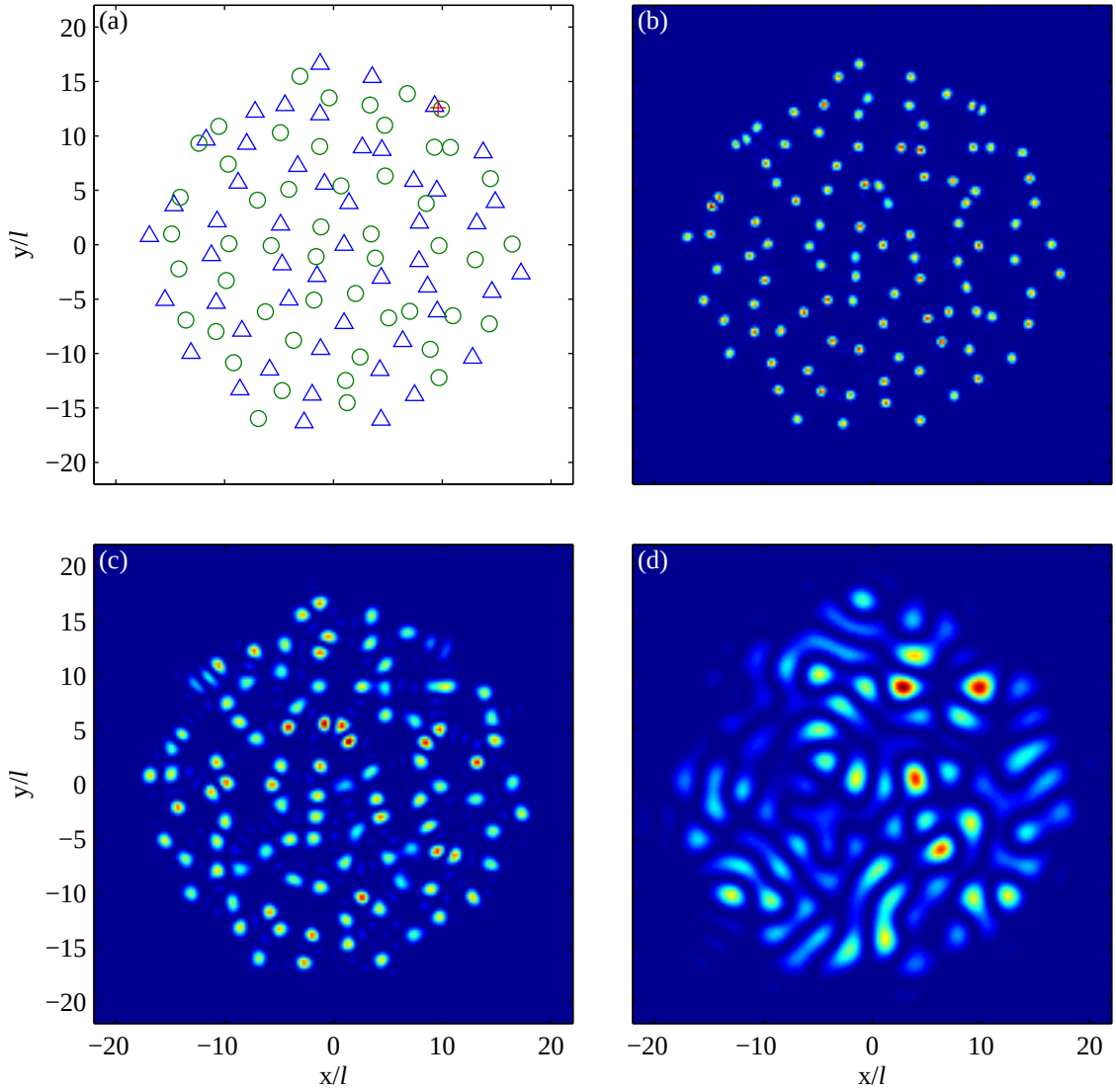

Figure 6.2: Imaging an individual particle configuration for the $n = 1$ state. (a) Particle configuration to be imaged, particles with spin $m = 1$ denoted by triangles and spin $m = -1$ by circles. A closely separated pair of particles with opposite spin is indicated by the red '+'. Images have numerical apertures (b) $\sin\theta = 0.75\lambda/\ell$, (c) $\sin\theta = 0.5\lambda/\ell$ and (d) $\sin\theta = 0.25\lambda/\ell$.

atoms. However over the entire distribution the position of each individual atom is distributed uniformly over a disk. The ensemble average in Equation (6.10) then leads to an image of a disk with uniform intensity, where the uniform intensity is related to the spin correlations over the spatial area of the point spread function, which is in turn determined by the numerical aperture of the optical system.

As discussed in [23], it is important to remember that the ensemble average is not what is observed in an individual experiment and that here the individual images could be modelled more closely by the individual particle configurations generated by the Monte Carlo algorithm. In Figure 6.2 we show images of an individual particle configuration from the $n = 1$ state. The first image for $\sin\theta = 0.75\lambda/\ell$ resolves the individual particles. As the numerical aperture decreases, the image probes the sum of the spins within the point spread function. For $\sin\theta = 0.5\lambda/\ell$ we can see cancellation in the image due to closely situated particles with opposite spin, such as the pair indicated by the red '+'. The image for $\sin\theta = 0.25\lambda/\ell$ probes the relative spin over a greater area.

Figure 6.3 shows images of an individual Monte Carlo particle configuration from the $n = 2$ state. In this state, the distance $(z_u - \zeta_v)$ between particles of opposite spin is raised to the power of two and, as a result, particles of opposite spin in this state do not come as close to each other as in the $n = 1$ state. The particles then spread out over a slightly larger disk. Cancellation in the image due to particles of opposite spin also then happens at lower numerical aperture.

6.2.3 Noise correlation imaging

If we look at an ensemble of particle configurations and their images, we can then do noise correlation analysis of the images [23]. This involves calculating correlations within each individual image in the ensemble and then comparing this with averages from the entire ensemble. For example, we can look at spatial correlations in the

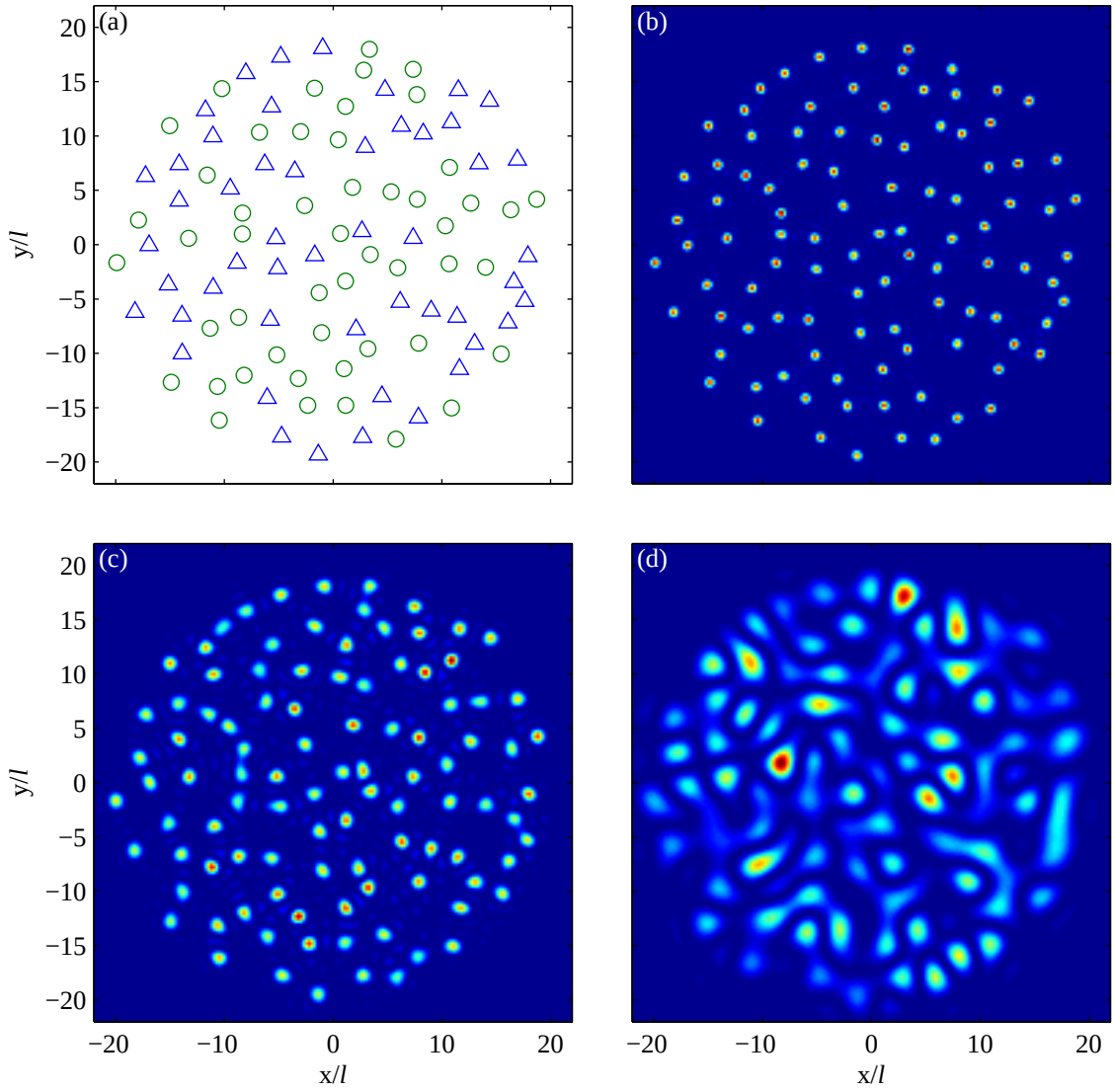

Figure 6.3: Imaging an individual particle configuration for the $n = 2$ state. (a) Particle configuration to be imaged, particles with spin $m = 1$ denoted by triangles and spin $m = -1$ by circles. Images have numerical apertures (b) $\sin\theta = 0.75\lambda/\ell$, (c) $\sin\theta = 0.5\lambda/\ell$ and (d) $\sin\theta = 0.25\lambda/\ell$.

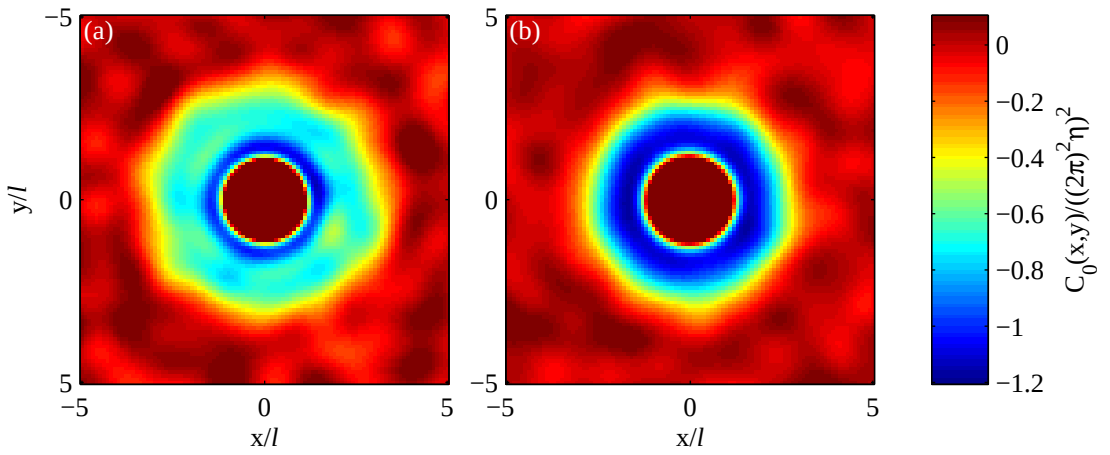

Figure 6.4: Noise correlation image $C_{\mathbf{0}}(\mathbf{x})$ of (a) the $n = 1$ state and (b) the $n = 2$ state. The imaging system has numerical aperture $\sin\theta = 0.45\lambda/\ell$. The central peaks are off the scale of the plot, with maximums of $18.8/((2\pi)^2\eta^2)$ and $13.8/((2\pi)^2\eta)^2$ for $n = 1$ and $n = 2$ respectively.

images by calculating

$$C_{\mathbf{r}}(\mathbf{x}) = \langle I(\mathbf{r})I(\mathbf{r}+\mathbf{x})\rangle - \langle I(\mathbf{r})\rangle\langle I(\mathbf{r}+\mathbf{x})\rangle. \tag{6.12}$$

In Figure 6.4 we compare plots of this function for the two grounds states, taking $\mathbf{r} = \mathbf{0}$ and averaging over an ensemble of 100000 images. The numerical aperture of the imaging system in this case is $\sin\theta = 0.45\lambda/\ell$.

Examining the noise correlation image of the $n = 2$ state in Figure 6.4(b) first, we see a large positive correlation in the centre out to a radius of about 1.2ℓ due to the finite width of the point spread function. The correlation image then becomes negative and reaches a minimum, which results from the low probability of a particle being in that region if another particle is at the origin. The noise correlation image then increases and approaching an average value of zero for our finite ensemble. In Figure 6.4(a) the $n = 1$ state has a far smaller region of low correlation due to lack of particles. Instead it has a region (from $\sim 1.7\ell$ to $\sim 3\ell$) of partial correlation due to particles with opposite spin, which are allowed to exist closer together in the $n = 1$ than in the $n = 2$ state.

6.3 Two photon spatial correlation imaging

To further probe the spatial spin correlations in the system we can again look to two-photon imaging. However, the situation is a little different than in the optical lattice case, where each atom occurs at a lattice site separated by a fixed distance. Here pairs of atoms can occur with a continuous range of separations so probing the system with two-photon states with a fixed separation is less useful.

Instead we can use a simpler state of two photons that are correlated in polarisation but not in position. Taking the initial state to be $\int d\boldsymbol{\kappa}_1 d\boldsymbol{\kappa}_2 \phi(\boldsymbol{\kappa}_1)\phi(\boldsymbol{\kappa}_2)|\boldsymbol{\kappa}_1\rangle_1 \otimes |\boldsymbol{\kappa}_2\rangle_2$, the two-photon image intensity is then

$$I(\mathbf{x}_1, \mathbf{x}_2) = \eta^2 \langle \psi_d^\dagger(\mathbf{x}_1, \mathbf{x}_2)\psi_d(\mathbf{x}_1, \mathbf{x}_2)\rangle \tag{6.13}$$

where

$$\psi_d(\mathbf{x}_1, \mathbf{x}_2) = \sqrt{8}\pi\kappa_l \int d\mathbf{x} \left(\frac{J_1(\kappa_l|\mathbf{x}_1 - \mathbf{x}|)}{|\mathbf{x}_1 - \mathbf{x}|}\psi_i(\mathbf{x}_2) + \frac{J_1(\kappa_l|\mathbf{x}_2 - \mathbf{x}|)}{|\mathbf{x}_2 - \mathbf{x}|}\psi_i(\mathbf{x}_1) \right) \psi_i(\mathbf{x})\hat{\rho}_z(\mathbf{x}'). \tag{6.14}$$

If the initial distribution of each photon $\psi_i(\mathbf{x})$ is uniform and $\mathbf{x}_1$ and $\mathbf{x}_2$ are separated by a distance greater than the width of the point spread function, the two photon intensity is then approximately proportional to the spatial spin correlation function

$$I(\mathbf{x}_1, \mathbf{x}_2) \widetilde{\propto} \langle (\hat{\rho}_z(\mathbf{x}_1) + \hat{\rho}_z(\mathbf{x}_2))^2 \rangle. \tag{6.15}$$

In Figure 6.5 we plot a slice through the two-photon distribution for a particle configuration from the $n = 1$ state. The slice was taken so that $\mathbf{x}_1$ is equal to the position of a spin-up particle and we have plotted the two-photon distribution as a function of $\mathbf{x}_2$. The distribution shows peaks at the positions of the other spin-up particles and troughs at the positions of the spin-down particles.

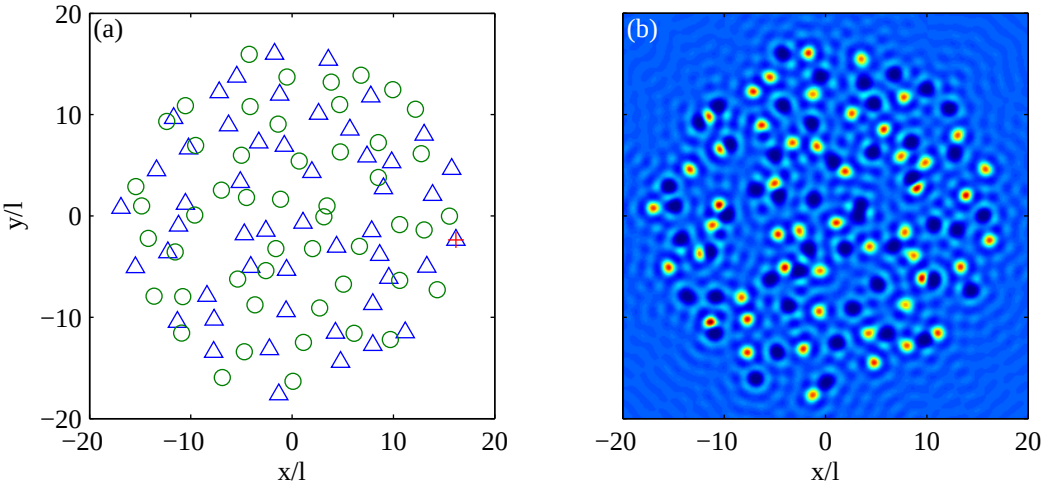

Figure 6.5: (a) Particle configuration from the $n = 1$ state wavefunction. (b) Slice from the two photon image of the particle configuration in (a). The slice is a plot over $\mathbf{x}_2$ for $\mathbf{x}_1 = (16.2, -2.4)$, which is the coordinate of the particle marked with a red '+' on the left. Here the numerical aperture of the imaging system is $\sin\theta = 2\lambda/(3\ell)$.

6.4 Phase contrast Imaging

The two photon imaging scheme described above relies on two-photon coincidence measurements which may limit its efficiency. Here we consider phase contrast imaging, which has been used successfully to image Bose gases *in situ* [130]. This method is similar to the coherent imaging proposal we considered where light is scattered and collected by a microscope to create an image. However, in this case instead of filtering out the unscattered light, the unscattered light and scattered light interfere to create an image with intensity proportional to the laser amplitude.

For our case, if the incoming light is $\boldsymbol{\epsilon}_2$-polarised, the light scattered according to the spin interaction has $\boldsymbol{\epsilon}_1$ polarisation and is phase-shifted by $-i$. For interference to occur between the unscattered and scattered light, the unscattered light's polarisation must be rotated and the phase of the resulting $\boldsymbol{\epsilon}_\mathbf{1}$ component must be shifted by $-i$ as well. This is achieved by placing a dot of material at the focal point of the first lens that will act as a quarter wave plate with optical

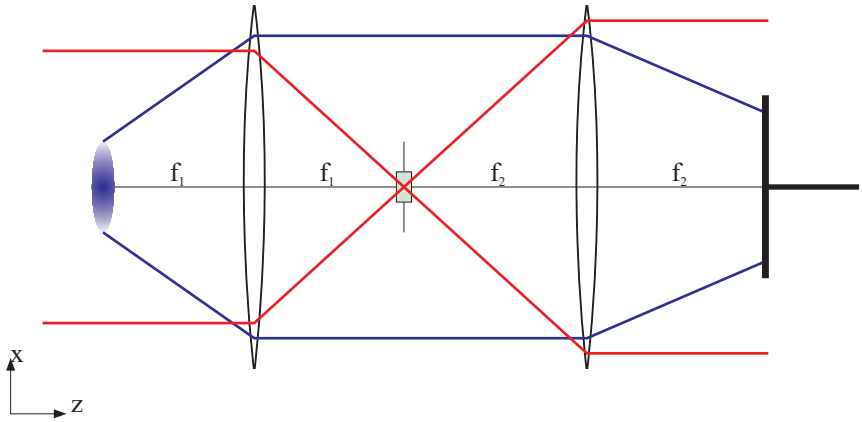

Figure 6.6: Schematic of phase contrast imaging arrangement. Coherent imaging light (red rays) illuminates the atomic sample resulting in scattered light (blue rays). The unscattered imaging light is focused by the first lens onto a quarter wave plate, rotating its polarisation and shifting its phase, while the scattered light is unaffected. The second lens then focuses the scattered light onto the detector, where it interferes with the phase-shifted unscattered light creating an image of the atoms.

axis at 45 degrees to the x-axis. This arrangement is shown in Figure 6.6. The unscattered light then passes through the wave plate, while the unscattered light, for the most part, is unaffected. We can then filter out $\boldsymbol{\epsilon}_2$-polarised light, leaving a phase contrast image of the spin distribution.

The intensity of the light at the detector is then a baseline intensity due to the unscattered light plus a modulation caused by the interference. We have

$$I(\mathbf{x}) = \frac{|\alpha|^2\eta}{2}\psi_i(\mathbf{x})^2 + \frac{|\alpha|^2\eta^2 a_1(\Delta)\kappa_l}{\sqrt{2}\pi\hbar}\psi_i(\mathbf{x})\int d\mathbf{x}'\frac{J_1(\kappa_l|\mathbf{x}-\mathbf{x}'|)}{|\mathbf{x}-\mathbf{x}'|}\psi_i(\mathbf{x}')\hat{\rho}_z(\mathbf{x}'), \quad (6.16)$$

where we have neglected the term proportional to $a_1(\Delta)^2$ and assumed the input light is in the coherent state $|\alpha\rangle_2$ with spatial profile $\psi_i(\mathbf{x})$. The interference term is proportional to the spin of the atoms, where troughs are produced by spin down atoms and peaks produced by spin up atoms. In fact for a single coordinate configuration, this reproduces the same image as we got by slicing through the two-photon distribution above in Figure 6.5. This allows us to probe the relationship between

the atomic spins without the need for photon coincidence measurement.

6.5 Conclusions

In this chapter we have investigated how ultracold atoms in the spin quantum Hall regime might be imaged. We have shown that the two ground states predicted by Liu *et al.* can be distinguished by coherent far field imaging. The difference in the far field images is a direct result of the different spatial correlations between the opposite spin atoms in the two ground states. These correlations can be revealed by noise correlation imaging, where we saw that analysis of an ensemble of images shows for the $n = 1$ state the relative closeness of atoms of opposite spin compared with the $n = 2$ case. We have tested a method of using pairs of photons to measure the spatial correlations in the many-body states, however this method was shown to provide no additional information over what is available through the technique of phase contrast imaging with coherent light.

This work has shown what might be learnt about these states using light scattering, and in the future this could be extended to examine what the images of excited states of the system would look like. In this chapter we have neglected the possibility of each consecutive light scattering event affecting the next, as we considered in Chapter 4. Applying the techniques of that chapter here may lead to interesting effects where the measurement process leads to new states of the atomic system.

Chapter 7

Conclusion

In this thesis we have presented a theoretical investigation of light scattering from ultracold bosons in optical potentials. Our work has been motivated by the fast development of ultracold atoms as tools for investigating many-body physics, which is accompanied by a need for better methods of probing the many-body states produced in experiments. We have shown how light scattering can be used in a number of different scenarios to reveal information about these states and also how it changes these states.

Specifically, we have seen that for the superfluid and Mott insulator states the angular distribution of light scattered distinguishes these states and reveals information about the correlations within them. In both cases the light scattered has a temperature dependence which may be used to measure the temperature of the state, however this has limited efficiency particularly in the Mott state due to scattering of atoms into higher bands of the optical lattice.

We have created a model of dynamic light scattering from small optical lattices in the regime where the Bose-Hubbard model can be exactly solved. In this model, scattering events followed by the detection of the photon change the many-body

state of the atoms, pushing the state, after a number of events, towards eigenstates of this measurement process. In some cases this leads to superposition of many-body states, where the final state is signalled by the angular distribution of the photons. This model demonstrates that light scattering distributions can be predicted by the static structure factor, even when the scattering significantly perturbs the initial state.

When the light scattering is spin dependent, we have shown that it is possible to distinguish different spin ground states of an optical lattice in images of the atoms. Furthermore, we have seen that in this case, it is also possible by using correlated input light to obtain enhanced resolution in images of the spin state. Correlated input light also allows us to directly probe the spatial spin correlations in the lattice.

Spin dependent scattering can also be employed to study atoms in synthetic magnetic fields, where we have shown that ground states in the quantum Hall regime can be distinguished by the angular dependence of scattering. We have also shown how correlations in these states can be revealed using noise correlation imaging and a variant of phase-contrast imaging.

7.1 Future work

Our work in this thesis has led us from studying strongly correlated systems in optical lattices to strongly correlated spin systems in synthetic magnetic fields. This provides an excellent platform for more research in the area of spin systems approaching the quantum Hall regime, which is particularly pertinent as new methods are making this an experimental possibility. As we saw in Chapter 6 there is potential for this regime to be achieved in a trapped Bose gas with optically induced magnetic fields. Furthermore these synthetic fields can also be applied to

atoms in optical lattices [38, 39] and this is an area where we would like to do future research.

In particular we see theoretical treatments of small numbers of atoms in traps or optical lattices as a potentially fruitful line of theoretical research. In this case the Hamiltonians could be solved exactly, as we did here in Chapter 4. For systems with two spin components, different interaction strengths between atoms in different spin states would lead to coupling between the spatial states and the internal states of the atoms, potentially leading to spatial-internal state entanglement. Coupling light to these systems may then lead to a way of probing the entanglement that is created. Moreover, for small lattice systems we can apply the dynamic light scattering formalism developed in Chapter 4 to examine how performing light scattering measurements would affect the evolution of the system, with the aim of generating further novel states of matter.

Bibliography

[1] William D. Phillips, *Laser cooling and trapping of neutral atoms*, Rev. Mod. Phys. **70**, 721 (1998).

[2] M. H. Anderson, J. R. Ensher, M. R. Matthews, C. E. Wieman, and E. A. Cornell, *Observation of Bose-Einstein condensation in a dilute atomic vapor*, Science **269**, 198 (1995).

[3] C. C. Bradley, C. A. Sackett, J. J. Tollett, and R. G. Hulet, *Evidence of Bose-Einstein condensation in an atomic gas with attractive interactions*, Phys. Rev. Lett. **75**, 1687 (1995). *ibid.* **79**, 1170 (1997).

[4] K. B. Davis, M.-O. Mewes, M. R. Andrews, N. J. van Druten, D. S. Durfee, D. M. Kurn, and W. Ketterle, *Bose-Einstein condensation in a gas of sodium atoms*, Phys. Rev. Lett. **75**, 3969 (1995).

[5] C. J. Pethick and H. Smith, **Bose-Einstein Condensation in Dilute Gases** (Cambridge University Press, 2002).

[6] Lev Pitaevskii and Sandro Stringari, **Bose-Einstein Condensation** (Oxford University Press, 2003).

[7] B. DeMarco and D. S. Jin, *Onset of Fermi degeneracy in a trapped atomic gas*, Science **285**, 1703 (1999).

[8] Andrew G. Truscott, Kevin E. Strecker, William I. McAlexander, Guthrie B. Partridge, and Randall G. Hulet, *Observation of Fermi pressure in a gas of trapped atoms*, Science **291**, 2570 (2001).

[9] A. J. Leggett, *Bose-Einstein condensation in alkali gases: Some fundamental concepts*, Rev. Mod. Phys. **73**, 307 (2001).

[10] R. Ozeri, N. Katz, J. Steinhauer, and N. Davidson, *Colloquium: Bulk Bogoliubov excitations in a Bose-Einstein condensate*, Rev. Mod. Phys. **77**, 187–205 (2005).

[11] M. Saba, T. A. Pasquini, C. Sanner, Y. Shin, W. Ketterle, and D. E. Pritchard, *Light scattering to determine the relative phase of two Bose-Einstein condensates*, Science **307**, 1945–1948 (2005).

[12] S. Inouye, A. P. Chikkatur, D. M. Stamper-Kurn, J. Stenger, D. E. Pritchard, and W. Ketterle, *Superradiant Rayleigh scattering from a Bose-Einstein condensate*, Science **285**, 571 (1999).

[13] Cheng Chin, Rudolf Grimm, Paul Julienne, and Eite Tiesinga, *Feshbach resonances in ultracold gases*, Rev. Mod. Phys. **82**, 1225–1286 (2010).

[14] Markus Greiner, Cindy A. Regal, and Deborah S. Jin, *Emergence of a molecular Bose-Einstein condensate from a Fermi gas*, Nature **426**, 537–540 (2003).

[15] T. Bourdel, L. Khaykovich, J. Cubizolles, J. Zhang, F. Chevy, M. Teichmann, L. Tarruell, S. J. J. M. F. Kokkelmans, and C. Salomon, *Experimental study of the BEC-BCS crossover region in lithium 6*, Phys. Rev. Lett. **93**, 050401 (2004).

[16] M. W. Zwierlein, J. R. Abo-Shaeer, A. Schirotzek, C. H. Schunck, and W. Ketterle, *Vortices and superfluidity in a strongly interacting Fermi gas*, Nature **435**, 1047–1051 (2005).

[17] P.S. Jessen and I.H. Deutsch. *Optical lattices.* volume 37 of *Advances In Atomic, Molecular, and Optical Physics*, pages 95 – 138. Academic Press, 1996.

[18] D. Jaksch, C. Bruder, J. I. Cirac, C. W. Gardiner, and P. Zoller, *Cold bosonic atoms in optical lattices*, Phys. Rev. Lett. **81**, 3108 (1998).

[19] Markus Greiner, Olaf Mandel, Tilman Esslinger, Theodor W. Hänsch, and Immanuel Bloch, *Quantum phase transition from a superfluid to a Mott insulator in a gas of ultracold atoms*, Nature **415**, 39 (2002).

[20] Maciej Lewenstein, Anna Sanpera, Veronica Ahufinger, Bogdan Damski, Aditi Sen De, and Ujjwal Sen, *Ultracold atomic gases in optical lattices: mimicking condensed matter physics and beyond*, Adv. Phys. **56**, 243–379(137) (March 2007).

[21] Thilo Stöferle, Henning Moritz, Christian Schori, Michael Köhl, and Tilman Esslinger, *Transition from a strongly interacting 1d superfluid to a Mott insulator*, Phys. Rev. Lett. **92**, 130403 (2004).

[22] D. Clément, N. Fabbri, L. Fallani, C. Fort, and M. Inguscio, *Exploring correlated 1d Bose gases from the superfluid to the Mott-insulator state by inelastic light scattering*, Phys. Rev. Lett. **102**, 155301 (2009).

[23] Ehud Altman, Eugene Demler, and Mikhail D. Lukin, *Probing many-body states of ultracold atoms via noise correlations*, Phys. Rev. A **70**, 013603 (2004).

[24] Simon Folling, Fabrice Gerbier, Artur Widera, Olaf Mandel, Tatjana Gericke, and Immanuel Bloch, *Spatial quantum noise interferometry in expanding ultracold atom clouds*, Nature **434**, 481–484 (2005).

[25] T. Rom, Th. Best, D. van Oosten, U. Schneider, S. Folling, B. Paredes, and I. Bloch, *Free fermion antibunching in a degenerate atomic Fermi gas released from an optical lattice*, Nature **444**, 733–736 (2006).

[26] Ferdinand Brennecke, Tobias Donner, Stephan Ritter, Thomas Bourdel, Michael Kohl, and Tilman Esslinger, *Cavity QED with a Bose-Einstein condensate*, Nature **450**, 268–271 (2007).

[27] Yves Colombe, Tilo Steinmetz, Guilhem Dubois, Felix Linke, David Hunger, and Jakob Reichel, *Strong atom-field coupling for Bose-Einstein condensates in an optical cavity on a chip*, Nature **450**, 272–276 (2007).

[28] Ferdinand Brennecke, Stephan Ritter, Tobias Donner, and Tilman Esslinger, *Cavity optomechanics with a Bose-Einstein condensate*, Science **322**, 235–238 (2008).

[29] W. Chen, D. Meiser, and P. Meystre, *Cavity QED determination of atomic number statistics in optical lattices*, Phys. Rev. A **75**, 023812 (2007).

[30] Igor B. Mekhov, Christoph Maschler, and Helmut Ritsch, *Cavity-enhanced light scattering in optical lattices to probe atomic quantum statistics*, Phys. Rev. Lett. **98**, 100402 (2007).

[31] Igor B. Mekhov, Christoph Maschler, and Helmut Ritsch, *Probing quantum phases of ultracold atoms in optical lattices by transmission spectra in cavity quantum electrodynamics*, Nat. Phys. **3**, 319 – 323 (2007).

[32] Jonas Larson, Bogdan Damski, Giovanna Morigi, and Maciej Lewenstein, *Mott-insulator states of ultracold atoms in optical resonators*, Phys. Rev. Lett. **100**, 050401 (2008).

[33] Igor B. Mekhov and Helmut Ritsch, *Quantum nondemolition measurements and state preparation in quantum gases by light detection*, Phys. Rev. Lett. **102**, 020403 (2009).

[34] K. Eckert, Ł. Zawitkowski, A. Sanpera, M. Lewenstein, and E. S. Polzik, *Quantum polarization spectroscopy of ultracold spinor gases*, Phys. Rev. Lett. **98**, 100404 (2007).

[35] Kai Eckert, Oriol Romero-Isart, Mirta Rodríguez, Maciej Lewenstein, Eugene S. Polzik, and Anna Sanpera, *Quantum non-demolition detection of strongly correlated systems*, Nat. Phys. **4**, 50–54 (2008).

[36] T Roscilde, M Rodríguez, K Eckert, O Romero-Isart, M Lewenstein, E Polzik, and A Sanpera, *Quantum polarization spectroscopy of correlations in attractive fermionic gases*, New J. Phys. **11**, 055041 (2009).

[37] Y.-J. Lin, R. L. Compton, K. Jimenez-Garcia, J. V. Porto, and I. B. Spielman, *Synthetic magnetic fields for ultracold neutral atoms*, Nature **462**, 628–632 (2009).

[38] Tudor D. Stanescu, Victor Galitski, and S. Das Sarma, *Topological states in two-dimensional optical lattices*, Phys. Rev. A **82**, 013608 (2010).

[39] N. Goldman, I. Satija, P. Nikolic, A. Bermudez, M. A. Martin-Delgado, M. Lewenstein, and I. B. Spielman, *Realistic time-reversal invariant topological insulators with neutral atoms*, Phys. Rev. Lett. **105**, 255302 (2010).

[40] J. Ruostekoski, C. J. Foot, and A. B. Deb, *Light scattering for thermometry of fermionic atoms in an optical lattice*, Phys. Rev. Lett. **103**, 170404 (2009).

[41] Kazimierz Łakomy, Zbigniew Idziaszek, and Marek Trippenbach, *Thermal effects in light scattering from ultracold bosons in an optical lattice*, Phys. Rev. A **80**, 043404 (2009).

[42] Klemens Hammerer, Anders S. Sørensen, and Eugene S. Polzik, *Quantum interface between light and atomic ensembles*, Rev. Mod. Phys. **82**, 1041–1093 (2010).

[43] Immanuel Bloch, Jean Dalibard, and Wilhelm Zwerger, *Many-body physics with ultracold gases*, Rev. Mod. Phys. **80**, 885–964 (2008).

[44] Mikhail Kolobov, editor, **Quantum Imaging** (Springer, 2007).

[45] Maciej Lewenstein, Li You, J. Cooper, and K. Burnett, *Quantum field theory of atoms interacting with photons: Foundations*, Phys. Rev. A **50**, 2207–2231 (1994).

[46] A. L. Fetter and J. D. Walecka, **Quantum Theory of Many-Particle Systems** (McGraw-Hill, 1971).

[47] Ivan H. Deutsch and Poul S. Jessen, *Quantum-state control in optical lattices*, Phys. Rev. A **57**, 1972–1986 (1998).

[48] J. M. Zhang, S. Cui, H. Jing, D. L. Zhou, and W. M. Liu, *Probing the quantum ground state of a spin-1 Bose-Einstein condensate with cavity transmission spectra*, Phys. Rev. A **80**, 043623 (2009).

[49] Dominik Schneble, Gretchen K. Campbell, Erik W. Streed, Micah Boyd, David E. Pritchard, and Wolfgang Ketterle, *Raman amplification of matter waves*, Phys. Rev. A **69**, 041601(R) (2003).

[50] Olaf Mandel, Markus Greiner, Artur Widera, Tim Rom, Theodor W Hnsch, and Immanuel Bloch, *Coherent transport of neutral atoms in spin-dependent optical lattice potentials.*, Phys. Rev. Lett. **91**, 010407 (2003).

[51] Gavin K. Brennen, Carlton M. Caves, Poul S. Jessen, and Ivan H. Deutsch, *Quantum logic gates in optical lattices*, Phys. Rev. Lett. **82**, 1060–1063 (1999).

[52] D. Jaksch, H.-J. Briegel, J. I. Cirac, C. W. Gardiner, and P. Zoller, *Entanglement of atoms via cold controlled collisions*, Phys. Rev. Lett. **82**, 1975–1978 (1999).

[53] W. Vincent Liu, Frank Wilczek, and Peter Zoller, *Spin-dependent Hubbard model and a quantum phase transition in cold atoms*, Phys. Rev. A **70**, 033603 (2004).

[54] L.-M. Duan, E. Demler, and M. D. Lukin, *Controlling spin exchange interactions of ultracold atoms in optical lattices*, Phys. Rev. Lett. **91**, 090402 (2003).

[55] P Blair Blakie and Charles W Clark, *Wannier states and Bose-Hubbard parameters for 2d optical lattices*, Journal of Physics B: Atomic, Molecular and Optical Physics **37**, 1391 (2004).

[56] D. Jaksch and P. Zoller, *The cold atom Hubbard toolbox*, Annals of Physics **315**, 52 – 79 (2005). Special Issue.

[57] Charles Kittel, **Introduction to Solid State Physics** (John Wiley and Sons, 7th edition, 1995).

[58] Neil W. Ashcroft and David N. Mermin, **Solid State Physics** (Thomson Learning, Toronto, 1st edition, January 1976).

[59] Andrew John Daley, **Manipulation and Simulation of Cold Atoms in Optical Lattices**, D.Phil thesis, Leopold-Franzens-Universität Innsbruck, 2005.

[60] Stephen Richard James Franz Clark, **Strongly correlated one-dimensional systems of cold atoms in optical lattices**, DPhil thesis, University of Oxford, 2007.

[61] W. Kohn, *Analytic properties of Bloch waves and Wannier functions*, Phys. Rev. **115**, 809–821 (1959).

[62] Kerson Huang, **Statistical Mechanics** (John Wiley and Sons, 1963).

[63] Matthew P. A. Fisher, Peter B. Weichman, G. Grinstein, and Daniel S. Fisher, *Boson localization and the superfluid-insulator transition*, Phys. Rev. B **40**, 546–570 (1989).

[64] H. P. Büchler, G. Blatter, and W. Zwerger, *Commensurate-incommensurate transition of cold atoms in an optical lattice*, Phys. Rev. Lett. **90**, 130401 (2003).

[65] L A Lugiato, A Gatti, and E Brambilla, *Quantum imaging*, J. Opt. B **4**, S176 (2002).

[66] Agedi N. Boto, Pieter Kok, Daniel S. Abrams, Samuel L. Braunstein, Colin P. Williams, and Jonathan P. Dowling, *Quantum interferometric optical lithography: Exploiting entanglement to beat the diffraction limit*, Phys. Rev. Lett. **85**, 2733–2736 (2000).

[67] Sean Bentley and Robert Boyd, *Nonlinear optical lithography with ultra-high sub-Rayleigh resolution*, Opt. Express **12**, 5735–5740 (2004).

[68] Hiroshi Ooki, Masaya Komatsu, and Masato Shibuya, *A novel super-resolution technique for optical lithography — nonlinear multiple exposure method*, Japanese Journal of Applied Physics **33**, L177–L179 (1994).

[69] Eli Yablonovitch and Rutger B. Vrijen, *Optical projection lithography at half the Rayleigh resolution limit by two-photon exposure*, Optical Engineering **38**, 334–338 (1999).

[70] P. R. Hemmer, A. Muthukrishnan, M. O. Scully, and M. S. Zubairy, *Quantum lithography with classical light*, Phys. Rev. Lett. **96**, 163603 (2006).

[71] M. Kiffner, J. Evers, and M. S. Zubairy, *Resonant interferometric lithography beyond the diffraction limit*, Phys. Rev. Lett. **100**, 073602 (2008).

[72] Zeyang Liao, M. Al-Amri, and M. Suhail Zubairy, *Quantum lithography beyond the diffraction limit via Rabi oscillations*, Phys. Rev. Lett. **105**, 183601 (2010).

[73] Mankei Tsang, *Relationship between resolution enhancement and multiphoton absorption rate in quantum lithography*, Phys. Rev. A **75**, 043813 (2007).

[74] William N. Plick, Christoph F. Wildfeuer, Petr M. Anisimov, and Jonathan P. Dowling, *Optimizing the multiphoton absorption properties of maximally path-entangled number states*, Phys. Rev. A **80**, 063825 (2009).

[75] Mankei Tsang, *Quantum imaging beyond the diffraction limit by optical centroid measurements*, Phys. Rev. Lett. **102**, 253601 (2009).

[76] D. M. Brink and G. R. Satchler, **Angular Momentum** (Oxford University Press, March 1994).

[77] J. J. Sakurai, **Modern Quantum Mechanics (2nd Edition)** (Addison Wesley, January 1994).

[78] C. Menotti, M. Krämer, L. Pitaevskii, and S. Stringari, *Dynamic structure factor of a Bose-Einstein condensate in a one-dimensional optical lattice*, Phys. Rev. A **67**, 053609 (2003).

[79] D. van Oosten, D. B. M. Dickerscheid, B. Farid, P. van der Straten, and H. T. C. Stoof, *Inelastic light scattering from a Mott insulator*, Phys. Rev. A **71**, 021601 (2005).

[80] Ana Maria Rey, P. Blair Blakie, Guido Pupillo, Carl J. Williams, and Charles W. Clark, *Bragg spectroscopy of ultracold atoms loaded in an optical lattice*, Phys. Rev. A **72**, 023407 (2005).

[81] Stefan Rist, Chiara Menotti, and Giovanna Morigi, *Light scattering by ultracold atoms in an optical lattice*, Phys. Rev. A **81**, 013404 (2010).

[82] Igor B. Mekhov, Christoph Maschler, and Helmut Ritsch, *Light scattering from ultracold atoms in optical lattices as an optical probe of quantum statistics*, Phys. Rev. A **76**, 053618 (2007).

[83] W. Chen and P. Meystre, *Cavity QED characterization of many-body atomic states in double-well potentials: Role of dissipation*, Phys. Rev. A **79**, 043801 (2009).

[84] Léon Van Hove, *Correlations in space and time and Born approximation scattering in systems of interacting particles*, Phys. Rev. **95**, 249–262 (1954).

[85] Robert Graham and Dan Walls, *Spectrum of light scattered from a weakly interacting Bose-Einstein condensed gas*, Phys. Rev. Lett. **76**, 1774 (1996).

[86] Allan Griffin, **Excitations in a Bose-Condensed Liquid** (Cambridge University Press, 1993).

[87] M. Girardeau and R. Arnowitt, *Theory of many-boson systems: Pair theory*, Phys. Rev. **113**, 755–761 (1959).

[88] C. W. Gardiner, *Particle-number-conserving Bogoliubov method which demonstrates the validity of the time-dependent Gross-Pitaevskii equation for a highly condensed Bose gas*, Phys. Rev. A **56**, 1414 (1997).

[89] Y. Castin and R. Dum, *Low-temperature Bose-Einstein condensates in time-dependent traps: Beyond the U(1) symmetry-breaking approach*, Phys. Rev. A **57**, 3008 (1998).

[90] M. D. Girardeau, *Comment on "Particle-number-conserving Bogoliubov method which demonstrates the validity of the time-dependent Gross-Pitaevskii equation for a highly condensed Bose gas"*, Phys. Rev. A **58**, 775–778 (1998).

[91] N. Bogolubov, *On the theory of superfluidity*, J. Phys. **11**, 23 (1947).

[92] D. van Oosten, P. van der Straten, and H. T. C. Stoof, *Quantum phases in an optical lattice*, Phys. Rev. A **63**, 053601 (2001).

[93] Keith Burnett, Mark Edwards, Charles W Clark, and Martin Shotter, *The Bogoliubov approach to number squeezing of atoms in an optical lattice*, J. Phys. B: At., Mol. Opt. Phys. **35**, 1671–1678 (2002).

[94] L. D. Landau, E. M. Lifshitz, and L. P. Pitaevskii, **Statistical Physics Part 2** (Pergamon Press, 1980).

[95] E. C. Svensson, V. F. Sears, A. D. B. Woods, and P. Martel, *Neutron-diffraction study of the static structure factor and pair correlations in liquid* ^4He, Phys. Rev. B **21**, 3638–3651 (1980).

[96] D. M. Stamper-Kurn, A. P. Chikkatur, A. Görlitz, S. Inouye, S. Gupta, D. E. Pritchard, and W. Ketterle, *Excitation of phonons in a Bose-Einstein condensate by light scattering*, Phys. Rev. Lett. **83**, 2876 (1999).

[97] E. E. Rowen, N. Bar-Gill, and N. Davidson, *Quantum enhancement of higher-order phononlike excitations of a Bose-Einstein condensate*, Phys. Rev. Lett. **101**, 010404 (2008).

[98] D. McKay, M. White, and B. DeMarco, *Lattice thermodynamics for ultracold atoms*, Phys. Rev. A **79**, 063605 (2009).

[99] J. K. Freericks and H. Monien, *Strong-coupling expansions for the pure and disordered Bose-Hubbard model*, Phys. Rev. B **53**, 2691–2700 (1996).

[100] P. Blakie, A.-M. Rey, and A. Bezett, *Thermodynamics of quantum degenerate gases in optical lattices*, Laser Physics **17**, 198–204 (2007).

[101] A. V. Rau, J. A. Dunningham, and K. Burnett, *Measurement-induced relative-position localization through entanglement*, Science **301**, 1081–1084 (2003).

[102] Scott N. Sanders, Florian Mintert, and Eric J. Heller, *Matter-wave scattering from ultracold atoms in an optical lattice*, Phys. Rev. Lett. **105**, 035301 (2010).

[103] Robert W Cherng and Eugene Demler, *Quantum noise analysis of spin systems realized with cold atoms*, New J. Phys. **9**, 7 (2007).

[104] Inés de Vega, J. Ignacio Cirac, and D. Porras, *Detection of spin correlations in optical lattices by light scattering*, Phys. Rev. A **77**, 051804 (2008).

[105] Juha Javanainen and Janne Ruostekoski, *Optical detection of fractional particle number in an atomic Fermi-Dirac gas*, Phys. Rev. Lett. **91**, 150404 (2003).

[106] J. Ruostekoski, J. Javanainen, and G. V. Dunne, *Manipulating atoms in an optical lattice: Fractional fermion number and its optical quantum measurement*, Phys. Rev. A **77**, 013603 (2008).

[107] Vittorio Giovannetti, Seth Lloyd, Lorenzo Maccone, and Jeffrey H. Shapiro, *Sub-Rayleigh-diffraction-bound quantum imaging*, Phys. Rev. A **79**, 013827 (2009).

[108] K. J. Blow, Rodney Loudon, Simon J. D. Phoenix, and T. J. Shepherd, *Continuum fields in quantum optics*, Phys. Rev. A **42**, 4102–4114 (1990).

[109] Mikhail I. Kolobov and Claude Fabre, *Quantum limits on optical resolution*, Phys. Rev. Lett. **85**, 3789–3792 (2000).

[110] David Nikolaevich Klyshko, **Photons and Nonlinear Optics** (Gordon and Breach Science, New York, 1988).

[111] A. I. Lvovsky and M. G. Raymer, *Continuous-variable optical quantum-state tomography*, Rev. Mod. Phys. **81**, 299–332 (2009).

[112] S. K. Yip, *Dimer state of spin-1 bosons in an optical lattice*, Phys. Rev. Lett. **90**, 250402 (2003).

[113] Kiyohide Nomura and Satoshi Takada, *A new phase of the $s = 1$ bilinear-biquadratic chain: -a trimerized state-*, J. Phys. Soc. Jpn. **60**, 389–392 (1991).

[114] K. v. Klitzing, G. Dorda, and M. Pepper, *New method for high-accuracy determination of the fine-structure constant based on quantized Hall resistance*, Phys. Rev. Lett. **45**, 494–497 (1980).

[115] D. C. Tsui, H. L. Stormer, and A. C. Gossard, *Two-dimensional magnetotransport in the extreme quantum limit*, Phys. Rev. Lett. **48**, 1559–1562 (1982).

[116] R. B. Laughlin, *Anomalous quantum Hall effect: An incompressible quantum fluid with fractionally charged excitations*, Phys. Rev. Lett. **50**, 1395–1398 (1983).

[117] C. L. Kane and E. J. Mele, *Quantum spin Hall effect in graphene*, Phys. Rev. Lett. **95**, 226801 (2005).

[118] B. Andrei Bernevig and Shou-Cheng Zhang, *Quantum spin Hall effect*, Phys. Rev. Lett. **96**, 106802 (2006).

[119] Xiao-Liang Qi, Yong-Shi Wu, and Shou-Cheng Zhang, *Topological quantization of the spin Hall effect in two-dimensional paramagnetic semiconductors*, Phys. Rev. B **74**, 085308 (2006).

[120] B. Andrei Bernevig, Taylor L. Hughes, and Shou-Cheng Zhang, *Quantum spin Hall effect and topological phase transition in HgTe quantum wells*, Science **314**, 1757–1761 (2006).

[121] Markus König, Steffen Wiedmann, Christoph Brne, Andreas Roth, Hartmut Buhmann, Laurens W. Molenkamp, Xiao-Liang Qi, and Shou-Cheng Zhang, *Quantum spin Hall insulator state in HgTe quantum wells*, Science **318**, 766–770 (2007).

[122] Xiong-Jun Liu, Xin Liu, L. C. Kwek, and C. H. Oh, *Optically induced spin-Hall effect in atoms*, Phys. Rev. Lett. **98**, 026602 (2007).

[123] Shi-Liang Zhu, Hao Fu, C.-J. Wu, S.-C. Zhang, and L.-M. Duan, *Spin Hall*

effects for cold atoms in a light-induced gauge potential, Phys. Rev. Lett. **97**, 240401 (2006).

[124] Xiong-Jun Liu, Xin Liu, L. C. Kwek, and C. H. Oh, *Fractional spin Hall effect in atomic Bose gases*, Phys. Rev. B **79**, 165301 (2009).

[125] Xiong-Jun Liu, Xin Liu, Congjun Wu, and Jairo Sinova, *Quantum anomalous Hall effect with cold atoms trapped in a square lattice*, Phys. Rev. A **81**, 033622 (2010).

[126] Guocai Liu, Shi-Liang Zhu, Shaojian Jiang, Fadi Sun, and W. M. Liu, *Simulating and detecting the quantum spin Hall effect in the kagome optical lattice*, Phys. Rev. A **82**, 053605 (2010).

[127] B. I. Halperin, *Theory of the quantized Hall conductance*, Helv. Phys. Acta **56**, 75–102 (1983).

[128] H. Yuen and J. Shapiro, *Optical communication with two-photon coherent states – Part I: Quantum-state propagation and quantum-noise*, Information Theory, IEEE Transactions on **24**, 657 – 668 (1978).

[129] Mark E. J. Newman and G. T. Barkema, **Monte Carlo methods in statistical physics** (Oxford University Press, 1999).

[130] M. R. Andrews, M.-O. Mewes, N. J. van Druten, D. S. Durfee, D. M. Kurn, and W. Ketterle, *Direct, nondestructive observation of a Bose condensate*, Science **273**, 84 (1996).